JUMPING EXERCISE AND SCLEROSTIN ANTIBODY AS COUNTERMEASURES FOR SIMULATED MICROGRAVITY IN THE ADULT RAT SKELETON

A Dissertation

by

JON PAUL ELIZONDO

Submitted to the Office of Graduate and Professional Studies of
Texas A&M University
in partial fulfillment of the requirements for the degree of

DOCTOR OF PHILOSOPHY

Chair of Committee,	Harry Hogan
Committee Members,	Susan Bloomfield
	Pilwon Hur
	Bruce Tai
Head of Department,	Andreas Polycarpou

May 2021

Major Subject: Mechanical Engineering

ABSTRACT

Astronauts undergo significant bone loss during spaceflight. The lack of gravitational loading increases bone resorption and decreases bone formation in weight-bearing bones, resulting in a net loss of bone.

NASA traditionally counteracts bone loss by returning loading to astronauts' bones with daily resistance exercise. However, recent data suggest that exercise alone does not completely protect astronauts.

To supplement resistance exercise, NASA has previously investigated pharmaceutical countermeasures. A promising osteoporosis medication, anti-sclerostin antibody (Scl-Ab), could provide a viable treatment for spaceflight-induced bone loss.

This study investigated exercise and Scl-Ab as preventive countermeasures to microgravity-induced bone loss. To do this, we used the well-established hindlimb unloading rat model, and we administered Scl-Ab or a voluntary jumping protocol before hindlimb unloading.

First, we characterized loading from our jumping protocol. We found that ground reaction forces were on average 2.8 times body weight in our rats. These greatly elevated loads were osteogenic in forelimbs and hindlimbs. We found elevated bone formation rate, decreased osteoclast surface, and elevated cortical bone mineral density in jumping animals compared to untreated controls. Thus, we believe our jumping model is a physiologically relevant bone model for anabolic resistance exercise in humans.

Next, we assessed the impact of jumping, Scl-Ab, and unloading on bone integrity, and we directly compared the effectiveness of Scl-Ab and jumping exercise. Both preventive countermeasures were effective through four weeks of disuse. Bone architecture and mechanical properties in both treatment groups were improved after four weeks of unloading compared to untreated unloading controls. However, Scl-Ab was much more effective in the especially vulnerable cancellous compartment. Scl-Ab doubled bone volume fraction and tripled yield stress and elastic modulus of cancellous bone compared to unloading controls. Scl-Ab is an especially strong candidate for a pharmaceutical countermeasure to spaceflight bone loss.

Finally, we conducted finite element modeling of compression of cancellous rat bone. These simulations did not reflect findings from μCT and physical compression of the same bone volume. Despite these seemingly erroneous results, we have identified a number of procedural improvements, and we believe that these simulations will become a valuable and routine outcome for our lab.

DEDICATION

For Marc

I always tried to blaze a path for you.

I will do for others what I wish I could for you.

ACKNOWLEDGEMENTS

I first want to thank my family for supporting me through my years of study and through the dissertation process. My graduate studies did not go exactly as planned, and I would not have finished without my family's constant love and support.

In a similar vein, I would like to thank my lab for their support. Halfway through my program, my younger brother passed away. As I was at home with my family, my lab group sent me a care package that included the best pear I have ever tasted. It sounds silly, but I can still taste that pear, and it reminds me how lucky I am to have worked with such a caring group of people.

Dr. Hogan guided me throughout the five years of my graduate studies, and for a few years before that when I worked in the lab as an undergraduate. I am very grateful for his generous mentorship and for his willingness to provide feedback and advice at all hours of the night. I would also like to thank the other members of the Hogan lab who worked on this study with me. Dr. Scott Lenfest, Dr. Jess Brezicha, Zachary Kohn, Jennifer Kosniewski, and Jeremy Black were all instrumental to the project presented in this dissertation. They made the long hours worthwhile, and always patiently gave me directions when got lost in the maze-like animal care facility on a weekly basis.

I also had the pleasure of working closely with Dr. Bloomfield and her Bone Biology Lab. Her vast knowledge of biology allows our side of the lab to focus on doing what we love—breaking things. I always appreciate Dr. Bloomfield's insightful writing comments, which have greatly improved this dissertation and many a conference

presentation. I'd also like to extend a special thank you to former Bone Biology Lab member Dr. Corinne Metzger for helping with the analyses presented in this dissertation.

I would like to thank Dr. Tai for serving on my committee and sharing his expertise in finite element methods, as FEM was a new adventure for me in this dissertation. Dr. Hur served on my committee and provided guidance in analyzing the force plate data. Developing and implementing the force plate system was another effort that was outside of our lab's usual business, so Dr. Hur's guidance was much appreciated. Dr. Hur's students, Christian DeBuys, Kenny Chour, and Namita Anil Kumar were also invaluable to the force plate system's development. They gave me much instruction in circuit-building basics that I sorely needed.

Dr. Larry Suva was generous enough to conduct microCT scanning on our femurs, and Alyssa Falk coordinated the scanning and provided us with the resulting image files for our finite element analysis. I am very grateful for their help, without which this study would be much less compelling.

I would also like to thank Dr. Merriweather, John Avila, and all of my LSAMP Bridge to the Doctorate Fellows. My LSAMP BTD fellowship was a wonderful experience that showed me I could succeed in my doctoral journey. They gave me the confidence to return to A&M after my leave of absence.

Finally, I need to thank the University Writing Center. Working at the Writing Center off and on over the last seven years prepared me well to write this document, and my Writing Center accountability officer, Yuli Galarza Soto, kept me (mostly) on schedule as I wrote it up.

This project is the result of a massive effort by so many people. I am forever grateful to all people, named and not, who helped me reach the end of this project.

CONTRIBUTORS AND FUNDING SOURCES

Contributors

This work was supervised by a dissertation committee consisting of committee head Dr. Harry Hogan of the Department of Mechanical Engineering and committee members Dr. Bruce Tai of the Department of Mechanical Engineering, Dr. Susan Bloomfield of the Department of Kinesiology, and Dr. Pilwon Hur of the Gwangju Institute of Science and Technology.

Histomorphometry and pQCT were conducted by Dr. Corinne Metzger, formerly of the Department of Kinesiology. MicroCT was performed by Dr. Larry Suva of the Department of Veterinary Physiology and Pharmacology. Dr. Scott Lenfest formerly of the Department of Mechanical Engineering conducted portions of the three-point bending presented in this dissertation.

Funding Sources

The author was supported by NSF Award No. HRD 1612776 (LSAMP Bridge to the Doctorate Fellowship). This study was made possible by NASA Space Biology under grant NNX13AM43G. This dissertation's content is solely the responsibility of the author and does not represent official views of NASA or of NASA Space Biology.

TABLE OF CONTENTS

Page

Page

Page

LIST OF FIGURES

Page

Page

Page

LIST OF TABLES

Page

1. INTRODUCTION

One of the many health challenges posed by spaceflight is bone loss. Unprotected by modern countermeasures, astronauts can lose up to 1.5% of hip bone mineral density per month during spaceflight[1–3]. The main driver of this bone loss is the lack of gravitational loading on weight-bearing bones. Bone adheres to Wolff's Law, which states that the mass and strength of bone adapt to the mechanical environment[4]. Thus, weight-bearing bones respond to microgravity by increasing bone resorption and decreasing bone formation. This leads to the net loss of bone seen in astronauts.

However, it is also possible to take advantage of Wolff's Law to prevent bone loss by returning loading to the skeleton during spaceflight. NASA accomplishes this primarily through daily resistance exercise aboard the ISS. Studies that have relied on 2-D DEXA measurements have found exercise to be largely effective at preventing bone density loss during standard, 6-month International Space Station (ISS) missions[5,6]. However, recent data from high resolution peripheral computed tomography[7] and finite element modeling[8] suggests that exercise alone does not completely protect astronauts.

Due to concerns over the effectiveness of exercise alone as a countermeasure, NASA has previously investigated a common osteoporosis medication, the bisphosphonate alendronate. The treatment improved bone density in the astronauts, but it caused undesirable upper gastrointestinal side effects in a minority of subjects receiving the treatment[6]. In addition, bisphosphonates bind directly to mineral in bone and remain in the skeleton for years after treatment is administered[9], causing concerns

for NASA about long-term residual effects. Consequently, other pharmacological countermeasures warrant study. Specifically, anti-sclerostin antibody (Scl-Ab), a promising, anabolic osteoporosis medication approved by the FDA in 2019[10], could provide a viable countermeasure for spaceflight-induced bone loss.

Investigation of Scl-Ab and further characterization of resistance exercise as countermeasures to microgravity-induced bone loss would benefit NASA. It would be especially useful to directly compare the effectiveness of the two countermeasures in a spaceflight setting. However, instead of conducting human studies in astronauts, it is much more feasible to use animal models to gain insight into the human skeleton. A common ground-based animal model used for investigating spaceflight-induced bone loss is the hindlimb unloading (HU) rat model[11–13]. In this model, the rat is suspended by a tail harness so that its hindlimbs do not touch the ground, thereby removing weight bearing from the hindlimbs. Thus, the hindlimbs of the animal are an analog for the unloaded skeleton of astronauts. This model has been shown to produce similar bone mineral density loss to spaceflight, as well as significant deterioration of the material and structural properties of bone[11–14]. Our laboratory has significant experience with the HU rat model, which made it an ideal choice for this study.

Previous studies have implemented a number of rat models of resistance exercise that are compatible with HU. Some investigators have used rat jumping models for resistance exercise. These models involve conditioning rats to perform repeated vertical jumps of up to 15 inches. The jumping protocols were shown to increase bone formation and reduce bone loss due to HU or ovariectomy-induced estrogen deficiency[15–19].

Our voluntary jumping protocol suffers from the shortcoming that the loads it produces in the bones of our animals are unknown. To address this, we measured ground reaction forces (GRFs) produced during voluntary jumping. Researchers have previously constructed and implemented rodent-sized force platforms to measure GRFs produced by rats. These approaches have been used in some cases for gait analysis[20–22] and, more analogously, to measure GRFs in an impact-loading paradigm that involved dropping rats from various heights[23].

Administering Scl-Ab to rodents by injection was substantially easier than training them to follow an exercise protocol. The Scl-Ab treatment interferes with pro-resorptive and anti-formation signaling between bone cells. In this way, Scl-ab increases bone formation and decreases bone resorption[24]. The net effect of the treatment is an anabolic (growth-promoting) response in bone. In various animal studies, including a mouse study conducted on a space shuttle mission[25], Scl-Ab significantly mitigated bone loss caused by disuse[24,26,27].

The overall objective of this study was to use the HU rat model to investigate Scl-Ab treatment and exercise as countermeasures to disuse-induced bone loss. First, the loading created by our voluntary jumping exercise regimen was characterized by ground reaction force measurements. We expected that jumping would create substantial increases in the daily loading imposed on the rats' limbs compared to loads imposed by normal cage activity (measured by body weight). Next, changes in the mechanical and architectural properties of our rats' femurs were characterized through micro-computed tomography (μCT) and mechanical testing. Results from these techniques allow for

comparing the effects of Scl-Ab and voluntary jumping exercise. We hypothesized that both countermeasures would improve bone outcomes and protect from the harmful effects of HU. However, we expected Scl-Ab to be more effective in the cancellous bone of the distal femur, and jumping to be more effective in the cortical bone of the femur midshaft. Finally, we conducted a finite element simulation of compression testing of metaphyseal cancellous bone from our rats' distal femurs. We hoped that modeling would give us new insight into the physical cancellous compression test that is also presented in this study, and we expected the results of the physical and simulated compression to be highly correlated.

The rest of this dissertation will describe our process and findings on these topics in detail. It will start with an in-depth discussion of the study's background in Chapter 2. Chapter 3 will detail the experimental methods hinted at above. Chapter 4 will give the results of this study, and Chapter 5 will wrap up with a discussion of our findings and their implications.

2. BACKGROUND

2.1. Bone Adaptation and Remodeling

Bone is a living, dynamic tissue. It is constantly replaced throughout a lifetime by a process known as remodeling. In healthy bone, the remodeling process preserves bone integrity by removing microdamage that could lower bone strength if allowed to accumulate[28]. To accomplish remodeling, three bone cell types act in tandem: osteoclasts, osteoblasts, and osteocytes.

The remodeling process begins with osteocytes, which are responsible for monitoring the bone environment and signaling to other cells to coordinate their activities. Osteocytes comprise 90%-95% of all bone cells and are distributed throughout the entire bone matrix. They have numerous dendritic processes extending from their cell bodies that create a far-reaching osteocyte network[29]. Osteocytes use their extensive network in part to sense mechanical loading on bone, but their exact sensory mechanism is a matter of some debate. It is likely that osteocytes sense bone's loading state by sensing some combination of fluid shear stress[29] or direct deformation[30] acting on any number of their structures. Regardless of the exact mechanism, osteocytes respond to mechanical stimulus by secreting signaling proteins to direct the bone remodeling response[29].

Osteocytes trigger the remodeling process by activating the bone resorbing cells, osteoclasts. Osteoclasts are multi-nucleated cells responsible for the removal of bone. These cells eat up old and damaged bone to pave the way for the formation of new bone. After resorption, teams of osteoblasts migrate to the remodeling site and produce organic

bone matrix, known as osteoid. The osteoid is made mostly of collagen and serves as a template for hydroxyapatite crystals. After osteoid is formed, osteoblast activity ceases, and the organic osteoid gradually mineralizes over time. About 70% of the final hydroxyapatite content forms over the first two to three weeks after osteoid formation, and then hydroxyapatite crystals slowly grow to a physiological limit, which can take anywhere from several months to a year[30].

In cortical bone of humans and most large mammals, this remodeling process results in well-organized, cylindrical columns of bone called osteons. Osteons are formed as teams of osteoclasts and osteoblasts burrow through the cortical bone matrix and then lay down organic matrix to close the hole[31].

Bone remodeling is not so organized in cancellous bone. Instead, osteoclasts form Howship's lacunae, small and somewhat irregular resorption regions. Osteoblasts then lay down new bone in these lacunae. Unfortunately, if a certain trabecula has too many Howship's lacunae, the osteoclasts can actually penetrate through the trabecula. Osteoblasts then have no ability to replace the lost trabecula in the same location[32]. Instead, the bone cells will have to thicken surrounding, intact trabeculae to compensate for the lost trabecular integrity. This compensation is not fully effective and results in a permanent loss of bone strength[33].

One important function of the bone remodeling process is to allow bone to adapt its mechanical environment. Julius Wolff was the first to describe these adaptations in his self-named Wolff's Law[4]. Wolff's Law states that bone adapts to the loads that are

placed on it. This was taken further by Harold Frost, who proposed a thermostat analogy for bone remodeling[34,35].

Just like a thermostat that activates when temperatures fall above or below a set level, bone remodeling activates when bone strains fall above or below a critical threshold. When strain is increased above normal, osteocytes sense the increased strain and signal to osteoclasts and osteoblasts. The osteoclasts and osteoblasts respond by decreasing bone resorption and increasing bone formation. Together, the cells strengthen the bone in the directions that will be most advantageous for the increased or unusual mechanical loading. Conversely, when bone strains are reduced, osteoclasts increase their resorptive activity, and osteoblasts decrease their formation of new bone. This leads to net bone resorption and a decrease in bone density and strength[35].

2.2. Spaceflight and Bone

Since the beginning of manned spaceflight in the 1960's, NASA has known that exposure to microgravity causes bone loss. Analysis from the early Skylab program (1973-1974) found that collagen breakdown products doubled post flight compared to preflight values[36]. In the 1990's, NASA began using dual-energy X-ray absorptiometry (DXA) to measure bone loss due to spaceflight. With this new imaging technology, LeBlanc et al. found bone mineral density (BMD) losses of 1.06-1.56% per month at the spine and hip[37].

On October 31, 2000, NASA launched its first crew to the International Space Station (ISS)[38], signaling a new era for spaceflight. The early 2000s also saw the first uses of quantitative computed tomography (QCT) to measure bone mineral parameters

in astronauts. QCT was a significant advance over DXA in part because it gave researchers the ability to measure cancellous and cortical bone separately. Using QCT, Lang et al. found that astronauts lost over 5 times more cancellous BMD than cortical BMD at the hip. The loss of cancellous bone drove the astronauts' overall rate of BMD loss at the hip to ~1.5% per month[2]. This rate is about 3 times greater than *yearly* hip BMD loss rates in postmenopausal Caucasian women (the population most at-risk for osteoporosis)[39]. Further early NASA ISS studies[1,40] and findings in Russian cosmonauts[41] corroborated that spaceflight produces significant cancellous bone loss in weight-bearing bones.

To combat bone loss in microgravity, NASA developed a number of countermeasures. One of the most important of these countermeasures is exercise. Exercise attempts to protect bone from microgravity by restoring loading to the skeleton. A standard ISS mission lasts somewhere from 4 to 6 months[42], and during this time, astronauts spend about two hours per day exercising. Resistance exercise is especially important to NASA's plan to combat bone loss, since resistance exercise produces large loads on the skeleton. The Advanced Resistive Exercise Device (ARED) is the current resistance exercise device aboard the ISS. It was launched to the ISS in 2008[43], and has been in use ever since. Exercise with ARED does mitigate bone loss, but ARED alone is not fully protective of bone properties. LeBlanc et al. compared astronauts' pre- and post-flight DXA scans and found significant reductions in hip BMD, despite ARED exercise[6]. However, they also found that exercise on ARED was a substantial improvement compared to previous exercise protocols, which failed to protect astronauts

from bone loss at any load bearing site of interest[6]. NASA studies by Smith et al. reinforced these findings. They found that ARED exercise protected from bone loss at a variety of weightbearing sites[5], and that exercise was effective for both men and women[44].

Thanks in large part to ARED exercise, NASA currently considers bone loss to be a low priority issue. In fact, in their published Human Research Program roadmap, NASA states that they do not plan to fund bone-related studies beyond those that are currently underway[45]. However, recent studies using advanced diagnostics have found that ARED exercise might not be as protective as once thought. Vico et al.[7] and Sibonga et al.[46] used high resolution peripheral QCT to evaluate ARED-era astronauts' bone. They both found significant bone loss at weightbearing sites, and Vico et al. found that reductions in density and simulated strength did not recover during the 12 months following return to Earth and normal gravity[7]. In addition, finite element simulation of vertebral compression revealed significant decreases in post-flight strength[8]. The astronauts' lost vertebral strength did not return even up to 4 years after spaceflight[8].

In addition to newly discovered concerns with exercise alone as a primary countermeasure to bone loss, exercise faces a few other obstacles in long-term viability. The most pressing issue currently is that the ARED is not suited for long-duration missions beyond low earth orbit. The ARED is too large to travel in the Orion capsule that NASA plans to use on their proposed 2030s manned mission to Mars[47]. NASA is developing more compact exercise equipment to be used on Orion[47], but if the equipment is less reliable or not as effective as the ARED, astronaut health could suffer.

Additionally, any exercise countermeasure could fail if an astronaut becomes injured during a mission. As early as 2009, NASA had recorded 219 in-flight musculoskeletal injuries. These injuries arose from a variety of daily activities, but the most common cause was exercise[48]. If any such injury were to become serious enough to prevent an astronaut from exercising for a substantial period of time, the astronauts' bone health could suffer and the success of the mission could be imperiled. This is especially true if the injury were to occur on an exploration mission, where astronauts could be months away from return to Earth.

To supplement exercise, NASA has previously investigated osteoporosis drug treatments for astronauts. This effort culminated in a study where NASA administered the bisphosphonate alendronate (Fosamax ®) to a cohort of astronauts in the early 2010s[6]. Bisphosphonates are the most common class of osteoporosis drug. They bind to bone mineral and inhibit osteoclast resorption. The anti-resorptive alendronate was administered to nine ISS astronauts. While aboard the ISS, the astronauts took alendronate and continued to exercise on the ARED. The combination of ARED exercise and alendronate completely eliminated pre- to post-flight BMD loss as measured by DXA. In addition, alendronate-treated astronauts returned to Earth with higher total hip and lumbar spine BMD compared to astronauts that used ARED but received no drug treatment[6].

Although alendronate was overall highly effective, there were some minor setbacks to the study. Nine astronauts accepted participation in the study. One of the nine dropped out before the mission, after experiencing indigestion after a test dose of

alendronate. One more astronaut experienced indigestion while taking the drug aboard the ISS and ceased participation in the study[6]. Gastrointestinal side effects of alendronate are well known, so these results are not wholly unexpected. However, it is an unfortunate drawback of the treatment. Indigestion in space is surely something that most people are not keen to experience.

Another drawback of alendronate is actually its longevity. Since alendronate binds to bone mineral, it can stay in bone for many years. It has been detected in bone up to 10 years after administration in humans[30]. Thus, alendronate, or any bisphosphonate, could have effects on bone turnover of astronauts long after they have returned from space and no longer need the drug's protection.

Finally, any drug treatment is riskier to use in space than on Earth. One of the unsolved concerns in NASA's Human Research Roadmap is the "Risk of Ineffective or Toxic Medications During Long-Duration Exploration Spaceflight[49]." It is possible that higher levels of radiation experienced in transit to Mars could cause medications to rapidly degrade[49]. NASA is currently developing strategies to mitigate this risk. However, as of now, the unknown shelf life of drug treatments in space is a concern for any substance used on a long-duration mission.

NASA currently does not administer osteoporosis treatments to its astronauts. It is possible that NASA is concerned about the side effects, but more likely is that NASA is simply confident in ARED exercise as a primary countermeasure to bone loss. However, the ARED will not travel on long-duration missions in the Orion capsule, and astronauts have never been in microgravity for the 2-3 years necessary for a Mars

mission. It is feasible that no reasonable amount of exercise would be able to protect astronauts for such a long duration. Despite NASA's fairly successful run at mitigating bone loss aboard the ISS, there is reason to further study both exercise and drug treatments with a focus on lengthy stays microgravity.

2.3. Animal Models

Animal models are invaluable tools for researchers, especially when the variables of interest are difficult or impossible to replicate in humans. Spaceflight is one such variable. So, space researchers rely heavily on ground-based animal models to simulate the effects of microgravity and of countermeasures to its negative effects. This study leverages two animal models: the hindlimb unloading rat model for simulated microgravity, and a voluntary jumping exercise protocol that simulates resistance exercise.

2.3.1. Hindlimb Unloading/Disuse

The rodent hindlimb unloading (HU) model is a well-established animal model for microgravity. It was conceived in the 1970s by NASA researcher Morey-Holton (who was then just "Morey")[50]. The model was refined by Morey-Holton and Globus throughout the following years[11–13,51]. In the hindlimb unloading model, rodents are suspended by the tail so that their hindlimbs do not touch the ground. They use their front legs only for locomotion (sometimes with the help of an overhead pulley apparatus). The unloaded hindlimbs of these rodents are an analog for the load-bearing bones of astronauts. Both the rodents and the astronauts have previously load-bearing bones that then become unloaded. Indeed, rodents used in the hindlimb unloading model

see similar bone mineral density loss to astronauts in spaceflight and experience significant deterioration of their bone strength and quality[14,52]. Our lab has extensive experience with the hindlimb unloading rodent model[53–62], especially the unloaded rat model, so using hindlimb unloading in rats was a natural choice for this study.

2.3.2. Exercise

Previous studies have incorporated various animal models analogous to resistance exercise. One of the first animal models that studied the effects of loading on bone was external loading models. External loading models anesthetize an animal and then apply a cyclical axial or bending strain to a bone with an external device. These models first saw use in bird species[63–65], where the models provided some of the first detailed understanding of bone's adaptation to mechanical load. Eventually, external loading protocols were refined for use in rodents. As expected, these protocols are anabolic to bone[66], and can even achieve anabolism under disuse conditions[67]. In addition to their effectiveness, a main advantage of external loading models is that the loads applied are very well controlled. The loading parameters (magnitude, frequency, duration) are direct inputs of the system. However, using external loading as a model for resistance exercise lacks some physiological relevance, since external loading does not account for the forces that muscles themselves apply to bone.

Muscle forces are the largest physiological forces applied to bone[68], so it is desirable for any animal model for resistance exercise to include muscle forces. Our laboratory has previously investigated electrical muscle stimulation in a rodent model for resistance exercise. The muscle stimulation protocols eliminated disuse-related bone loss

and increased cortical bone formation[53,58,59,69]. However, there is still some physiological relevance missing from these models, as the muscle forces exerted during electrical muscle stimulation are likely not reflective of physiological muscle activity. To progress even further in physiological relevance, some researchers have turned to jumping exercise models.

A jumping exercise protocol has been used extensively by a group of collaborators from Japan. In their model, rats repeatedly jump up to a 15-inch ledge, catch the ledge with their front paws, and are then placed back on the floor by hand to resume jumping. This group's protocol has consistently produced increased bone mass[15,18,19,70] and reduced bone loss due to hindlimb unloading[17,71]. This exercise protocol uses negative reinforcement with a shock grid to train the rats to jump. Another effective jumping exercise protocol that uses negative reinforcement has been developed by Fluckey et al.[72–74] and has even been used successfully in a rat hindlimb unloading model[74]. While negative reinforcement seemed to be effective for those previous studies, animal behavioral studies have actually found that positive reinforcement can produce better training results.

Positive reinforcement is a type of operant conditioning that uses a positive reward stimulus to reinforce a desired behavior. Perhaps the most classic example of this comes from B.F. Skinner's work[75]. Through positive reinforcement, his rats learned to pull a lever after receiving food rewards for the action. Skinner was able to train the same behavior with negative reinforcement by shock grid. However, later research that compared positive and negative reinforcement in rats found that enthusiasm (number of

attempted lever pulls) and number of correct lever pulls were significantly higher in rats trained with food rewards compared to those trained with shock avoidance[76]. Additionally, a study in dogs compared electric shock collar reinforcement and reinforcement by food or praise and concluded that both methods were equally effective. However, dogs trained with the electric collars exhibited greater numbers of stress behaviors than those trained with positive reinforcement[77].

This study uses positive reinforcement by food reward to train a voluntary jumping behavior in rats. The method was developed by former lab member Dr. Scott Lenfest[78] and veterinary specialist Dr. Amelia Looper. Our jumping regimen is very comparable to those used by Fluckey et al.[72–74] and the group of Japanese collaborators[15,18,19,70], and results thus far have shown that our jumping protocol produces anabolic effects[78]. However, our training scheme has the practical advantage of eliminating costly electrical equipment that can be difficult to use and maintain. And, positive reinforcement by sugar treat likely reduces stress in our animals compared to negative reinforcement by shock avoidance. Thus, we believe we have created a physiologically relevant resistance exercise model that has distinct advantages compared to existing rodent models.

2.4. Anti-Sclerostin Antibody Treatment

In addition to simulated resistance exercise, this study investigated an anabolic drug treatment countermeasure, anti-sclerostin antibody (Scl-Ab). Scl-Ab works by inhibiting sclerostin signaling in bone. Sclerostin is a protein excreted by osteocytes that

prompts increased osteoclast activity and decreased osteoblast activity, tipping the balance of bone turnover in favor of resorption[79].

Sclerostin's significance was first discovered in patients with rare genetic disorders that prevented them from producing the protein. These patients had abnormally high bone mass, but their bone quality was normal[79]. Seeing this, researchers began to investigate sclerostin signaling as a therapeutic target. The eventual results of these efforts was the creation of an anabolic osteoporosis treatment, romosozumab, which was approved by the FDA in 2019[10].

Romosozumab works by binding to sclerostin excreted by osteocytes. Since the sclerostin protein is already bound to the drug, it cannot bind to osteoclasts or osteoblasts. Thus, the anti-sclerostin antibody prevents sclerostin from delivering its pro-resorptive signals to bone cells[80]. Since sclerostin binds to both osteoclasts and osteoblasts, inhibiting sclerostin has the dual effect of increasing bone formation and decreasing bone resorption[81]. This prompts a strongly anabolic response in bone[81], and makes Scl-Ab a promising countermeasure to bone loss.

2.4.1. Scl-Ab in Microgravity Animal Models

Animal models have been used to investigate Scl-Ab as a countermeasure for spaceflight-induced bone loss in a number of studies. Zhang et al. administered Scl-Ab to rats during hindlimb unloading. Scl-Ab treatment doubled cancellous BV/TV compared to untreated animals. They also found that Scl-Ab improved midshaft mechanical properties and increased bone formation rate[82]. Another study used a hindlimb immobilization model for disuse, but found similar results to Zhang et al. Scl-

Ab treatment improved trabecular architecture and increased bone formation rate compared to untreated controls[83].

Spatz et al. administered Scl-Ab to mice during hindlimb unloading and found gains in trabecular bone mass and cortical bone strength compared to mice that were untreated during unloading[24]. This same group also investigated the effects of Scl-Ab in a partial weightbearing mouse model, which is analogous to loading astronauts would experience on the Moon or Mars. They found that Scl-Ab treatment during partial weight bearing completely prevented bone deterioration in their mice, and even enhanced bone outcomes above fully weight-bearing control levels. This trend held true for whole-body BMD, mechanical strength at the femur midshaft, and cancellous BV/TV. The effect on cancellous bone was especially pronounced, with Scl-Ab-treated animals having 2-3 times the BV/TV of all other groups[84].

Members of this same research group also contributed to a spaceflight study that further reinforced Scl-Ab's potential as a countermeasure to microgravity-induced bone loss. They injected a cohort of mice with a single large dose of Scl-Ab, and then sent the mice to space aboard space shuttle mission STS-135. The group presented their findings from this study in a series of conference presentations[25,85–87]. Scl-Ab treatment eliminated losses in whole-body BMD, losses in cancellous volume and architecture at the tibia, and losses in bone strength at the femur midshaft. In fact, outcomes from Scl-Ab treated animals that flew on STS-135 were not different from ground-based controls in any reported measure[25]. Additionally, finite-element modeling found improved

strength at the proximal tibia[87], femoral neck[85], and in a non-weight-bearing vertebrae of the STS-135 animals[86].

Similar to the STS-135 study, our study used a pretreatment approach in our administration of Scl-Ab before a period of unloading, which makes it unique among ground-based analog studies. This study design will help NASA evaluate the efficacy of preventive, preflight bone countermeasures. In addition to being easier to administer and monitor, preflight drug countermeasures could reduce or eliminate the risk of accelerated pharmaceutical degradation during spaceflight[49].

While using the same pretreatment format, our study makes a number of improvements over the STS-135 study to improve translatability to astronauts. First, we administered smaller, weekly doses of Scl-Ab over four weeks before unloading, instead of one large dose immediately before spaceflight. Our weekly doses resulted in the same total dose as the STS-135 study, but our dosing scheme is more analogous to clinical Scl-Ab dosing[81]. Second, the STS-135 study used young growing mice, while our study used skeletally mature rats. The skeletally mature rats of our study should be more accurate models of skeletally mature, adult astronauts. Finally, our study includes a recovery period of normal weightbearing after unloading, while the STS-135 study euthanized its mice immediately upon return from spaceflight. Our study's recovery period will allow us to assess any lasting effects of Scl-Ab treatment, which could be especially important given recent findings in human clinical studies.

2.4.2. Scl-Ab Treatment in Humans

Scl-Ab treatment in humans has thus far been quite successful. A number of phase two and three clinical trials found that treatment with Scl-Ab (romosozumab) robustly increased markers of bone formation, decreased bone resorption markers, increased BMD, and reduced vertebral fracture incidence in osteoporotic patients. However, most of the gains produced by the treatment occurred in the first year. After 12 months of treatment, the patients' bone formation markers returned to or below baseline levels[81]. In addition, a follow up to one of the clinical trials found that osteoporotic women who ceased all forms of treatment lost 80-90% of the BMD that they had gained from a year of Scl-Ab followed by two years of the antiresorptive denosumab. These losses occurred within 12 months of ceasing treatment[88].

Thus, it seems there are issues with the long-term effectiveness of Scl-Ab treatment. Unfortunately, the exploration missions that NASA is planning will extend beyond the single year in which Scl-Ab seems most effective in humans. Although the unloading period in our study only simulates a standard 4–6-month ISS mission, our study's pretreatment design and lengthy recovery period after unloading should help to capture any negative long-term impacts of Scl-Ab treatment.

2.5. Compression Testing of Cancellous Bone

Bone mineral density, which is possibly the most common measure used to assess bone health, tends to underpredict losses in mechanical strength, especially in the cancellous region[56,57]. This is troublesome because cancellous bone is especially vulnerable to degradation (due to microgravity or otherwise). To truly determine the

strength of a material, the material must be broken. Destructive testing is, of course, problematic when trying to assess the strength of bone in human astronauts. However, our animal model for microgravity allows us to measure the strength of cancellous bone after simulated spaceflight, giving us insight into otherwise-unmeasurable outcomes.

2.5.1. Physical Testing

In 2000, Hogan et al. developed a procedure called reduced platen compression (RPC), which they used to destructively test rat cancellous bone[89]. To do this, they cut a slice from the end of the rat femur and compressed only the cancellous core of the slice, leaving the surrounding cortical bone intact. The result was a testing protocol that was twice as sensitive to changes in cancellous strength compared to compressing the whole cross section of the specimens (including cortical bone)[89].

RPC is different from most cancellous compression in the literature because it leaves the cortical shell intact. Most mechanical testing of cancellous specimens is done in larger bone samples, such as cow[90–93] or cadaver[92–96] bone. In these procedures, researchers machine a cancellous core out of the larger bone and then test that large, purely cancellous specimen. Our lab previously attempted to machine cancellous cores from rat bone with limited success[97]. Although the procedure did work, the samples from the much-smaller rat bones were often fragile, irregular, and unsuited for testing.

Our lab has not since attempted to machine cancellous cores from rat bone, but we would still like to be able to fully isolate cancellous bone from the cortical shell. Or, at the very least we would like to determine to what extent the cortical shell influences the results of RPC, which we label as a test of cancellous bone. The cortical shell

constrains lateral expansion of the cancellous region under compression, and we do not know exactly to what extent this affects RPC results.

2.5.2. Finite Element Method Simulation

One way that we can gain insight into RPC testing and isolate cancellous from cortical rat bone is to use finite element method simulation. FEM has become a powerful tool for bone researchers. This is largely because voxels from μCT images can be converted directly to elements for FEM. The researcher van Rietbergen introduced direct voxel conversion from μCT images in 1995[98]. Since then, μCT and computing technology have improved substantially, and FEM simulation of bone is now commonplace in the literature and is even sometimes used clinically to estimate bone strength[99,100].

One of the innovations that has occurred since 1995 is deriving FEM material input parameters on a specimen-by-specimen basis. Studies that have used this method report that determining tissue modulus uniquely for each specimen improved the fidelity of their simulations[101,102]. Of these methods, Easley et al. derived a relationship between μCT tissue mineral density and trabecular bone tissue modulus. They derived their relationship using data from a variety of species and then applied it in finite element models of rat trabecular bone[103]. We believe Easley et al.'s relationship is robust and applicable to our modeling of rat trabecular bone. Thus, we have adopted their relationship for this study.

2.6. Study Objectives

The goal of this study was to investigate exercise and Scl-Ab treatment preventive countermeasures to microgravity-induced bone loss. To do this, we used the well-established hindlimb unloading rat model[13,50,51], and we administered Scl-Ab or a voluntary jumping protocol before hindlimb unloading.

Our first desired outcome was to characterize forces produced during jumping by using a rat force plate system. Then, we tested whether those forces produced osteogenic effects in the rats' forelimbs and hindlimbs. We expected vertical ground reaction forces during jumping to be significantly elevated compared to normal loading, and we expected those elevated forces to be osteogenic in both the forelimbs and hindlimbs.

Our next goal was to assess the impact of the pretreatments and unloading on bone integrity and to directly compare the effectiveness of Scl-Ab and jumping exercise. We did this primarily through micro-computed tomography imaging and mechanical testing. We expected both pretreatments to protect from degradation caused by simulated microgravity. However, we predicted that Scl-Ab would outperform exercise in cancellous bone, while jumping would be more effective in cortical bone at the midshaft.

Our final goal in this study was to implement and refine a finite element simulation of compression of cancellous rat bone. As with imaging and mechanical testing, we expected FEM simulation to find Scl-Ab more effective than jumping in cancellous bone. We also expected simulated mechanical properties to be highly correlated to corresponding measures from physical testing. However, our main goal with the FEM simulation was to streamline the FEM protocol for large-scale use, to

assess its usefulness, and to use our findings to make improvements to the FEM procedure or to our procedure for physical testing of cancellous bone.

This study will provide new and useful insight into the effectiveness of preventive countermeasures to microgravity-induced bone loss. Our study adds to current knowledge through its pretreatment design and use of animal models that have high levels of physiological relevance. In addition, this study expands our lab's capabilities to continue producing biomechanical knowledge through the creation of a force plate system to characterize jumping and through the expansion of our previously-developed FEM protocol[104].

3. METHODS

3.1. Study Design

All procedures were reviewed and approved by the Texas A&M University Institutional Animal Care and Use Committee. All rats were housed singly in an American Associated for Accreditation of Laboratory Animal Care accredited housing facility. Rats were given *ad libitum* access to water. Rats were placed on a reverse 12-hour light/dark cycle (dark 10 AM to 10 PM) in a temperature-controlled room (23 ± 2 °C). Skeletally mature male Sprague-Dawley rats (4.5 months old; Envigo, Houston, TX) were acclimated to the animal facility and to the voluntary jumping protocol for 6 weeks.

After the first week of acclimation, all rats (regardless of eventual group assignment) were food restricted so that their body mass reached 90% of their arrival weight. Food restriction was necessary to promote interest in the food reward used during operant conditioning of jumping. Roughly half of ambulatory control and hindlimb unloading control animals were not food restricted. This subset of control animals was from the larger study of which this current project is a part. For food restricted animals, between 10 g and 15 g of standard rat chow (Teklad 8604, Envigo, East Millstone, New Jersey, USA) was provided to the rats each day during the operant conditioning and exercise periods, with the goal of first reducing their body mass and then maintaining a well-conditioned body condition score. Rat body weights and body condition scores were recorded twice per week. No rats ever deviated from a well-

conditioned body condition score. Food was provided *ad libitum* to all animals starting with the onset of hindlimb unloading (d28) and continuing to the end of the study (d112).

During acclimation, all rats were operantly conditioned in a custom cage to jump onto and off of a 10-inch-high platform using 45 mg sucrose pellets (Bio-Serv, Flemingtion, NJ, USA) as a reward. Following acclimation, rats were assigned to aging control (CON), HU control (HUC), anti-sclerostin antibody treatment (SCL) and voluntary jumping exercise (VJE) groups by body weight and jumping ability. VJE animals underwent an exercise program of 30 jumps/day, 5 days/week for 28 days. SCL animals were given 25 mg/kg body weight of anti-sclerostin antibody (Eli Lilly and Company, Indianapolis, IN) once a week for four weeks (28 days). This dosing scheme was recommended by scientists from Eli Lilly and Company, who provided the Scl-Ab. SCL, VJE, and HUC animals were then exposed to 28 days of HU, followed by 56 days of recovery. During HU and recovery, animals were given standard chow *ad libitum*. Subsets of animals were sacrificed after pretreatment (d28), after hindlimb unloading (d56), and at the end of recovery (d112). A visual representation of this experimental design can be seen in Figure 1 on the following page.

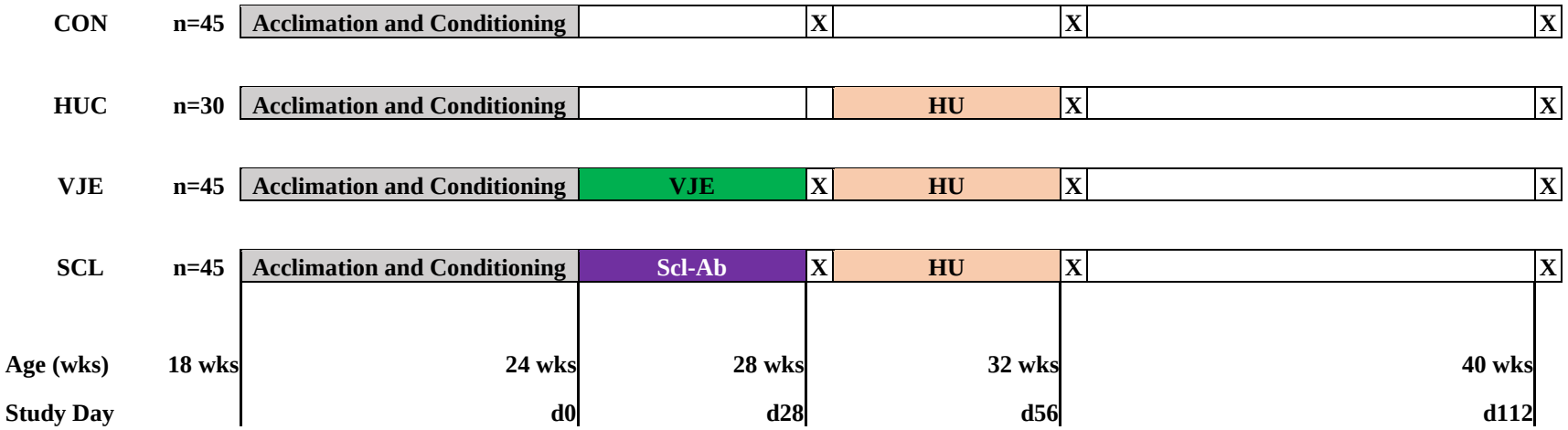

Figure 1. Study design.
"X" marks timepoints where animals were euthanized for *ex vivo* data collection, n=15/group at each timepoint.
CON: ambulatory control group
HUC: hindlimb unloading (HU) control group
VJE: voluntary jumping exercise group
SCL: sclerostin antibody (Scl-Ab) treatment group

3.1.1. Anti-Sclerostin Antibody Treatment

Anti-sclerostin antibody was provided by Eli Lilly and Company (Indianapolis, IN). Scl-Ab was suspended in saline. Eli Lilly's recommended dosing of 25 mg/kg body weight was administered as stipulated in our material transfer agreement. Each rat in the SCL group received a subcutaneous treatment injection once per week during the full 28-day pretreatment period, for four total injections of 25 mg/kg body weight each.

No sham injections were administered to jumping rats or rats in control groups. One subcutaneous injection per week was not deemed stressful enough to necessitate replication. In addition, previous work in our laboratory[105] that did not administer vehicle injections found results consistent with studies that did use vehicle injections for control groups[106].

3.1.2. Voluntary Jumping Exercise and Operant Conditioning

Conditioning rats to jump onto and off of a 10-inch-high platform was accomplished using a clicker for sound stimulus and positive reinforcement with 45 mg sucrose pellets (Bio-Serv, Flemington, NJ, USA). A photo of the custom jumping cage is in Figure 2. Conditioning began with the platform set to a height of 4 inches. At first, any interaction with the platform was rewarded by a loud click, followed by the placement of a sucrose pellet in the treat receptacle at the base of the cage. Repetitions of this process resulted in increased frequency of platform interaction, and eventually led to the rat consistently climbing onto the platform. Once this level of competence was reached, the platform height was raised in increments of 0.5, 1, or 2 inches up to the ultimate goal of 10 inches. As the height was raised, rats eventually became unable to

climb onto the platform and began jumping onto the platform instead. An individual rat was considered prepared to perform exercise when it could perform 20 jumps up and down from a 10-inch platform in less than 10 minutes. Roughly half of conditioned rats reached this level of jumping competence. In order to effectively test the impact of this VJE protocol on bone outcomes, rather than an intention-to-treat effect, only those rats competent in jumping were assigned to the VJE treatment group. Those animals assigned to the VJE group performed 30 jumps/day, 5 days/week for 28 days.

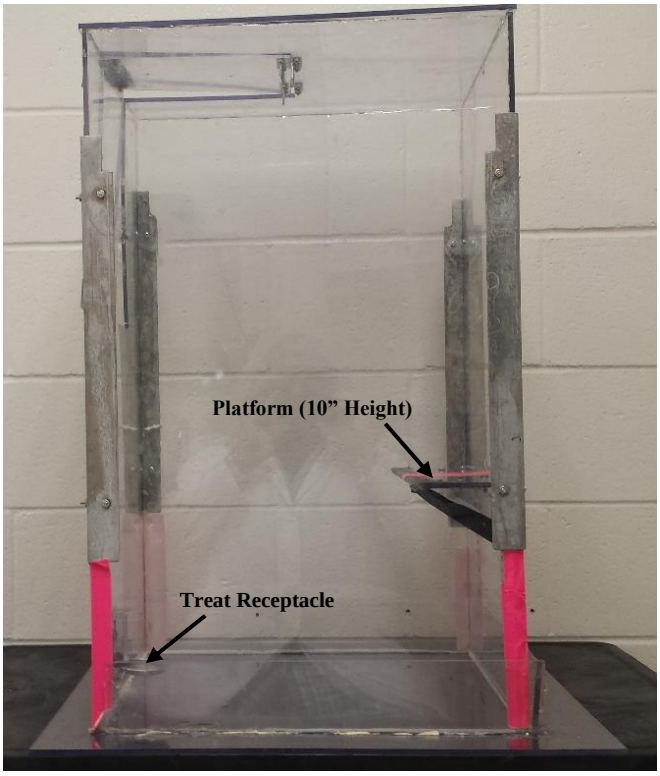

Figure 2. Custom jumping cage.
Rats were trained to jump onto the platform and then return to the treat receptacle for a sucrose reward. A platform height of 10” was used for fully-trained animals, but platform height is adjustable in 0.5” increments to allow for training progression.

3.1.3. Hindlimb Unloading

HU was performed using a modified version of the method described by Morey-Holton et al.[11–13]. In this model, a custom-made harness suspends the animal by the tail, lifting the hindlimbs from the ground (Figure 3). Though the hindlimbs are not allowed to touch the cage floor, the forelimbs maintain weight-bearing contact, and a pulley and bar system gives the animal full access to its cage and water supply. All animals were monitored twice daily during HU, with particular attention paid to tail health. Blood circulation to the tail tip can become reduced by the vertical orientation of the tail and constriction from the harness. We did not have any issues with tail health in this study.

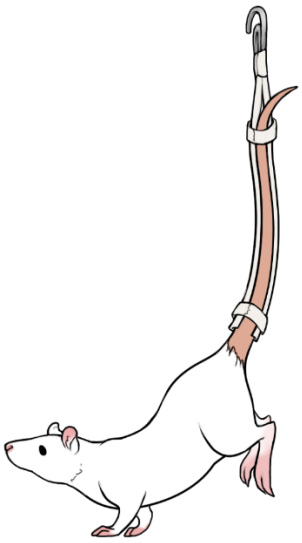

Figure 3. Hindlimb-unloaded rat. Reproduced with permission[62].
Upper hook of tail harness was linked to a pulley and bar system that allowed rats to freely walk on their front limbs and access the entirety of their 18" x 18" cages.

HUC, SCL, and VJE animals were exposed to 28 days of HU, followed by 56 days of recovery. CON animals did not undergo any HU. Recovery to normal weight-bearing ambulation was achieved by removing the tail harness and placing each animal

in a standard cage (singly-housed). All animals were housed singly, whether in HU or not.

3.1.4. Tissue Collection

Subsets (n=15) of animals from each treatment group were euthanized at the end of the pretreatment period (d28), at the end of the HU period (d56), and at the end of recovery (d112). Rats were injected with the fluorochrome label calcein (25 mg/kg body weight) nine and two days before termination. Rats were anesthetized via intraperitoneal injection of ketamine hydrochloride (Henry Schein Animal Health, Dublin, OH, USA) and Dexdomitor (dexmeditomidine hydrochloride, Zoetis, Parsippany, NJ, USA) in a 3 to 2 ratio. Rats were then euthanized by exsanguination (following cardiac puncture to collect whole blood) and decapitation. The left femur and humerus were excised, cleaned, wrapped in gauze, and stored in a phosphate-buffered saline solution at -20 ºC for subsequent imaging and mechanical testing. The right proximal tibia and humerus were excised and used for histological analysis. They were fixed in 10% phosphate-buffered formalin for 24 hours and then switched to 95% ethanol and stored at 4 ºC.

3.2. Outcome Measures

Ex vivo bone outcomes at the left femur were assessed for all animals in this study. This was done primarily through micro-computed tomography (μCT) imaging and mechanical testing. A finite element method (FEM) simulation of one of the mechanical tests was conducted to provide further insight into the effects of the treatments on the mechanical properties of the femur. Additionally, the jumping protocol itself was characterized by measuring vertical ground reaction forces (GRFs) produced by rats

during jumping. GRF data from forelimb landing and hindlimb jumping was paired with histomorphometry and peripheral quantitative computed tomography (pQCT) imaging from the respective limbs to determine the relative impacts of the jumping protocol on bone structure and bone cell activity.

3.2.1. Ground Reaction Force Measurement

Vertical ground reaction forces during jumping were measured as a surrogate for force acting on the bones of a subset of our animals (n=4). A custom rectangular force platform was cut into the floor of our jumping cage. Four 20 N load cells (Honeywell, Golden Valley, MN)[20] were placed at the corners of the platform. Animals were allowed to jump as usual. During this process, data were continuously collected via NI LabView (version 17.0f2) and an NI USB-6000 DAQ (National Instruments, Austin, TX). Jumps and landings were manually marked by a Boolean input in the LabView interface. A schematic of the GRF measurement apparatus can be seen in Figure 4.

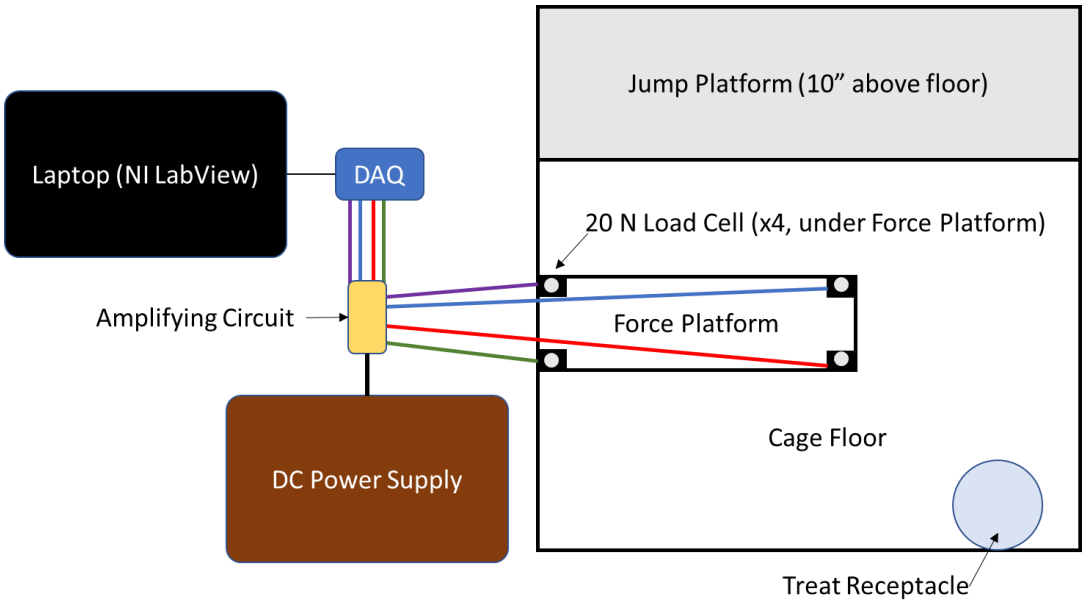

Figure 4. Schematic of GRF measurement system, as viewed from above.

Data analysis was carried out using MATLAB (version 8.5, The MathWorks, Inc., Natick, MA). Force plate output was passed through a low-pass filter to attenuate high frequency electrical noise[22]. Peak force and average rate of force development were reported for each sample. Average rate of force development (RFD) was defined as the average slope of the line from the point that the vertical GRF exceeds 110% of the rat’s body weight to the peak force of the same jump/landing. This procedure was adapted from calculations of RFD in humans[107,108]. A labeled representative force curve from a single jump and landing pair can be seen below in Figure 5. Peak force and RFD from three hindlimb jumps and three forelimb landings were averaged into one jump sample and one landing sample for each animal.

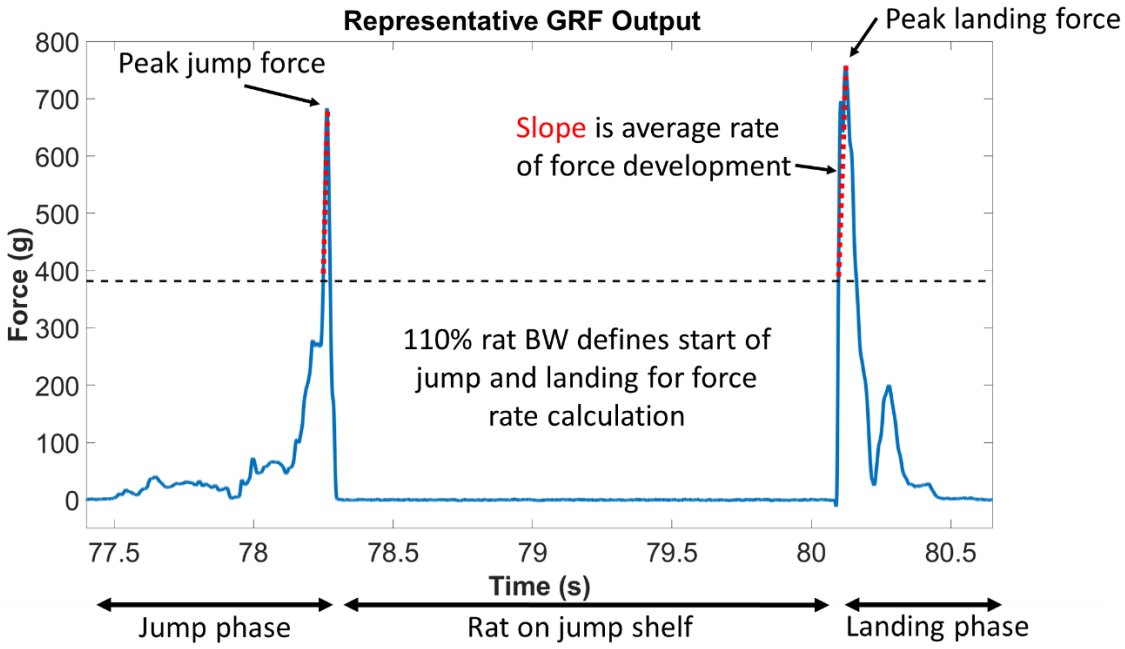

Figure 5. Representative force plate output for a single jump cycle and derivation of average rate of force development during jumping (take-off) and landing during voluntary jump exercise.

Statistical analysis was done in R (version 4.0.2, The R Foundation, Vienna, Austria). To account for the low number of samples per group (n=4), non-parametric statistics were used to assess differences in means for GRF data. A Friedman test with a Durbin-Conover post hoc test was used to compare peak jumping force, peak landing force, and body weight. This method is analogous to conducting a repeat-measures ANOVA and a standard post-hoc test. A Wilcoxon signed-rank test was used in place of a paired t-test to compare rate of force development between jumps and landings. Statistical significance was determined at $\alpha=0.05$.

3.2.2. *Ex Vivo* pQCT Imaging

Ex vivo peripheral quantitative computed tomography (pQCT) imaging was performed at the distal femur metaphysis (DFM) and proximal humerus (PH) on a subset of VJE and CON samples excised immediately after the pretreatment period (d28, n=10). A Stratec XCT Research-M device (Norland Corp., Ft. Atkinson, WI) was utilized with a voxel size of 100 μm and scanning beam thickness of 500 μm. CON and VJE group means were compared with an unpaired t-test for each bone site (R, version 4.0.2). No statistical comparison was performed between the femur and humerus. All pQCT measurements were taken by Dr. Corinne Metzger of the Bone Biology Lab, Texas A&M University, College Station Department of Health and Kinesiology.

3.2.3. Histomorphometry

After fixing in phosphate-buffered formalin, the right proximal tibia and right proximal humerus were serially dehydrated and embedded in methyl methacrylate (Aldrich M5, 590-9, St. Louis, MO, USA) per standard procedures[109]. The proximal tibia was microtomed in serial frontal sections of 8μm and 4μm thicknesses, starting at approximately 50% of the anterior-posterior depth of the metaphysis.

Von Kossa stain and tetrachrome counterstain was applied to the 4μm sections. These sections were analyzed for static cancellous histomorphometry with an OsteoMeasure Analysis System v 3.3 (OsteoMetrics, Inc., Atlanta, GA, USA) at a magnification of 400X. The 8μm sections of the proximal tibia and humerus were used for assessing dynamic histomorphometry outcomes using the fluorochrome label calcein, which binds to circulating calcium and is deposited on mineralizing surfaces. This

allowed for measurement of mineral apposition rate (MAR, micron/d), mineralizing surface per total bone surface perimeter (%MS/BS), and bone formation rate (BFR, $\mu m^3/\mu^2/d$). All sample preparation and histomorphometric image analysis was performed by Dr. Corinne Metzger of the Bone Biology Lab, Department of Health and Kinesiology, Texas A&M University, College Station, in accordance with standard procedures and nomenclature[109].

3.2.4. µCT Imaging

Cancellous densitometric and architectural parameters were assessed with high resolution imaging of the left distal femur metaphysis (DFM) with micro-computed tomography (µCT) analyses performed by collaborator Dr. Larry Suva (Professor and Head, Department of Veterinary Physiology & Pharmacology, Texas A&M University). A Scanco µCT 50 (Scanco Medical, Brüttisellen, Switzerland) was used to scan a 1.2 mm thick section of the DFM at a voxel size of 6 µm. In addition to standard trabecular analysis, these µCT scans were also used to construct finite element models of the DFM. Image stacks for a subset of femurs (n = 29) were generated of the scan region for conversion into 3D models of the DFM, as discussed more thoroughly in the finite element methods section further below.

3.2.5. Three-Point Bend Mechanical Testing

Cortical bone mechanical properties at the femoral midshaft were measured with a three-point bending test. Before testing, the anteroposterior and mediolateral surface diameters of each sample were measured at the midshaft using digital calipers (Mitutoyo, Kawasaki, Kanagawa, Japan). The sample was then placed anterior side

down onto round steel pin supports with a pin diameter of 3 mm and with a support span of 15 mm (Figure 6). Quasi-static loading was applied by an Instron 3345 (Instron, Norwood, MA) at the mid-diaphysis at a rate of 2.54 mm/min until fracture. Load was measured with a 1 kN load cell (Instron, Norwood, MA), and displacement was measured by the Instron 3345 itself.

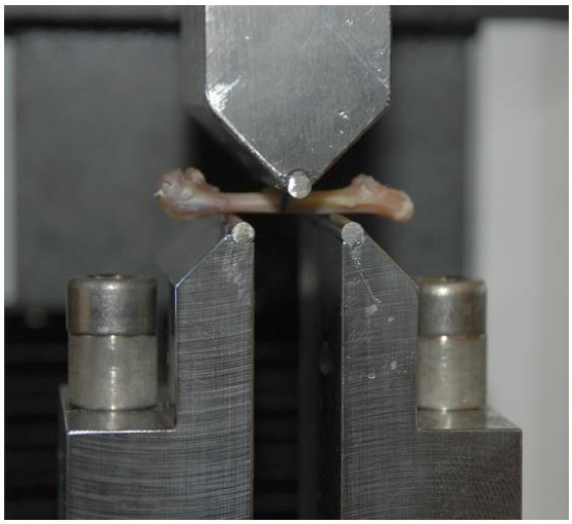

Figure 6. Three-point bend mechanical testing of rat femur.
Femur is placed anterior side down and loaded on the posterior surface at the midshaft.

Raw load vs. displacement data from testing was passed to a custom MATLAB script (ver. 9.8). This script was used to determine extrinsic mechanical properties. Stiffness was determined by manually selecting a linear region of the load vs. displacement curve before yield. The slope of this linear region is stiffness. The linear region was then extrapolated down to the x-axis. This x-intercept was used as the starting point from which all displacements were measured. The yield point was determined by a secant method. A line with a slope 97% of the selected linear region was drawn up from the linear region's x-intercept. The point where the 97% slope line

intersects the load vs. displacement curve is the yield point. Finally, energies absorbed were calculated by summing the area under the load vs. displacement curve in various regions of interest. For a much-needed visual illustration of this method, see Figure 6Figure 7 on the following page.

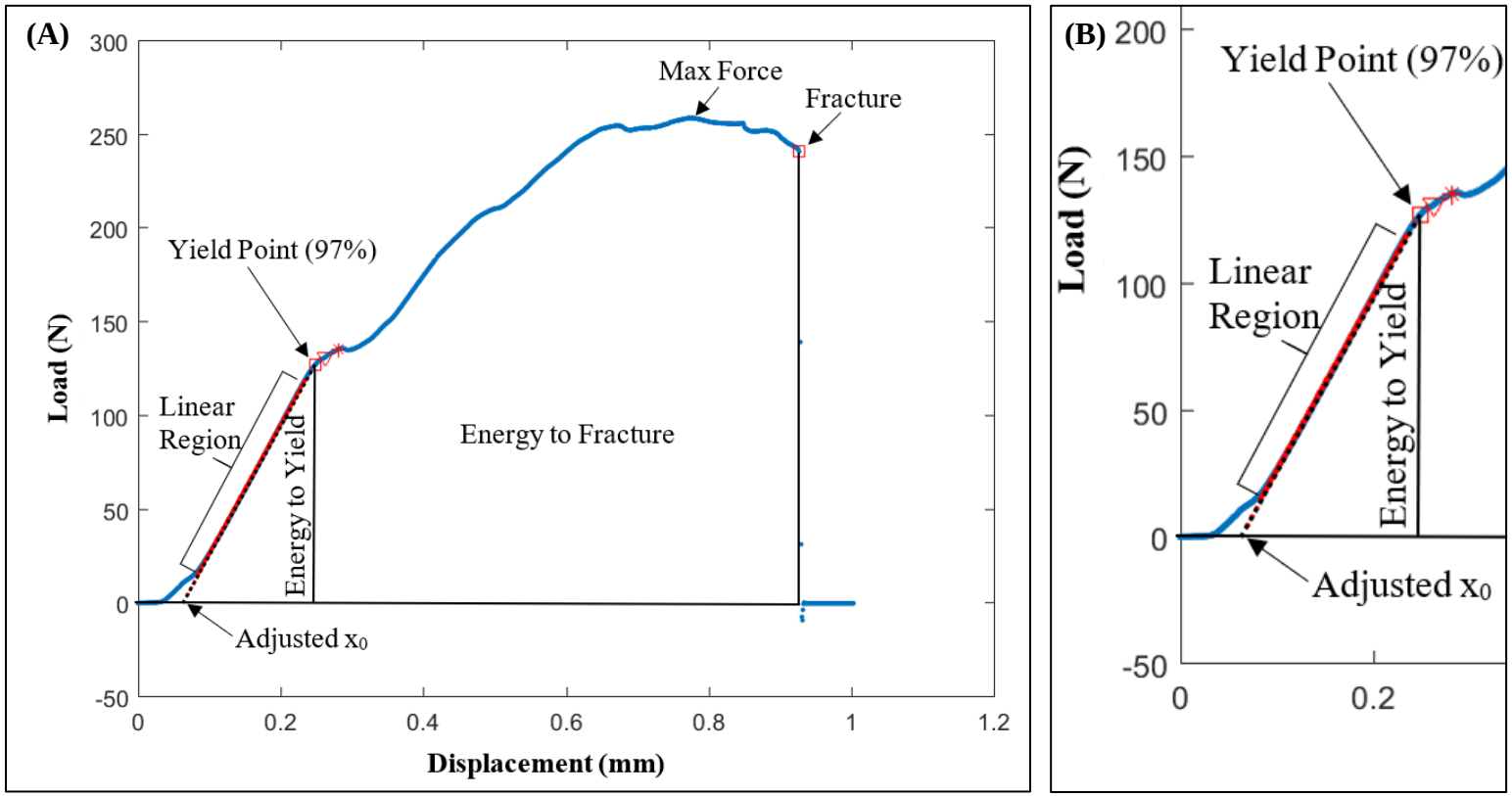

Figure 7. Three-point bending extrinsic property determination.
(A) Representative overall load vs. displacement curve and analysis, (B) details of linear region and yield analysis

Intrinsic mechanical properties were estimated using classical beam theory, which is standard for three-point bending of long bones[30]. Yield stress was calculated as follows:

$$\sigma_{yield} = \frac{F_{yield} L \left(\frac{D_{AP}}{2}\right)}{4I} \quad \textbf{(1)}$$

where F_{yield} is the yield force determined by the secant method described above, L is the support span (15 mm in this case), D_{AP} is the anterior-posterior diameter of the bone at the loading point, and I is the area moment of inertia of the cross section at the loading point.

The area moment of inertia, I was determined from previous *ex vivo* pQCT scans at the femur midshaft[78]. To avoid error caused by non-matching alignment of the femurs during scanning and testing, the following equation was used to approximate the area moment of inertia:

$$I = \frac{I_{polar}}{2} \quad \textbf{(2)}$$

I_{polar} is the polar area moment of inertia measured by pQCT. This equation assumes that the cross section of the femur midshaft is circular, which is roughly accurate. The resulting approximation of I is valid for any loading direction.

Ultimate stress was calculated much the same as yield stress:

$$\sigma_{ult} = \frac{F_{ult} L \left(\frac{D_{AP}}{2}\right)}{4I} \quad \textbf{(3)}$$

where F_{ult} is the highest force sustained by the femur before fracture, and the other parameters are unchanged from the yield calculation. (L is the support span, D_{AP} is the

anterior-posterior diameter of the bone at the loading point, and *I* is the area moment of inertia of the cross section at the loading point.)

Elastic modulus was calculated as follows:

$$E = \frac{kL^3}{48I} \quad \textbf{(4)}$$

where *k* is the stiffness of the sample determined by the slope of the selected linear region. *L* and *I* are the same as in stress calculations.

Finally, pre-yield toughness (or resilience) was calculated as:

$$U_{T,pre-yield} = \frac{\frac{3}{4} W_{yield} (D_{AP})^2}{LI} \quad \textbf{(5)}$$

where W_{yield} is the work (energy) absorbed by the femur before its yield point. As before, *L* is the support span, *I* is the area moment of inertia, and D_{AP} is the anterior-posterior diameter.

3.2.6. Reduced Platen Compression Mechanical Testing

Cancellous bone mechanical properties were measured by reduced platen compression testing (RPC) of specimens taken from the distal femur metaphysis (DFM). Samples 2.0 mm thick were cut from the DFM starting at the most distal point of the intercondylar fossa. A Well precision diamond wire saw (Well Diamond Wire Saws, Inc., Norcross, GA) was used to make all cuts (Figure 8). High-resolution photographs were made of the sample and edited in ImageJ (NIH, Bethesda, MD) to determine the size of the loading platen. The diameter of the loading platen was chosen to be 70% of the diameter of the largest circle that can inscribe the endocortical perimeter of the proximal surface of the specimen, which is the smaller cut surface for distal femur

metaphysis specimens (Figure 9A). Using the Instron 3345, quasi-static loading at 0.25 mm/min was applied only to the cancellous region of the sample, not the cortical shell (Figure 9).

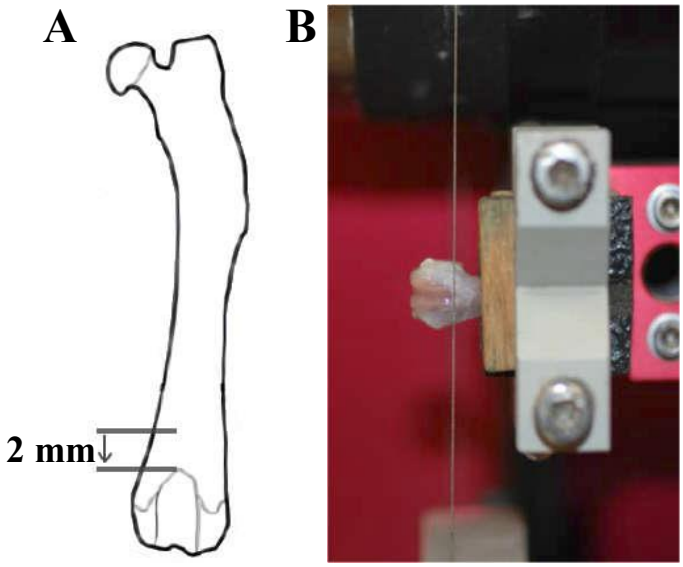

Figure 8. Reduced platen compression specimen location.
(A) Schematic of RPC specimen location, (B) corresponding specimen being cut on the diamond wire saw

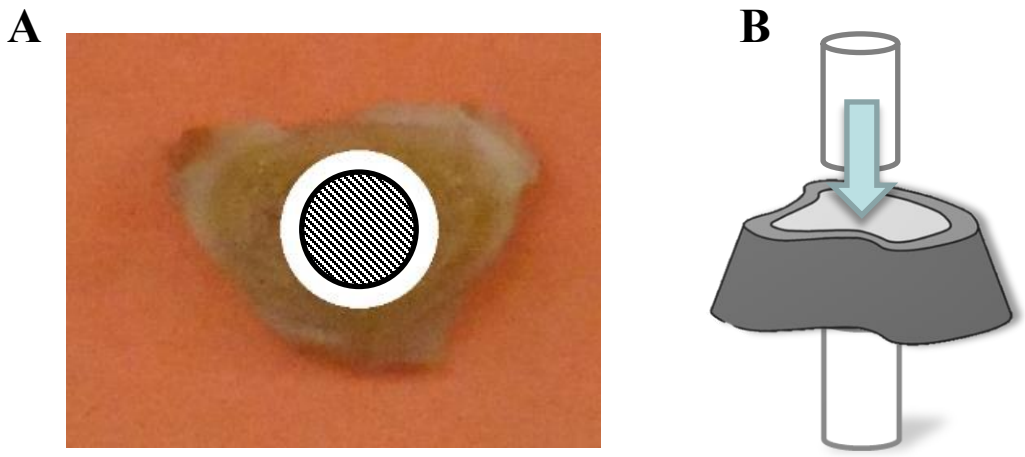

Figure 9. Reduced platen compression testing details
(A) RPC specimen with largest inscribed cortical circle (white) and corresponding calculated size (striped), (B) schematic of RPC testing, loading is applied only to cancellous core of specimen

The same custom MATLAB script that was used in three-point bending was used to analyze RPC load vs. displacement data. A linear region on the load-displacement curve was manually selected to determine the stiffness of each specimen. The yield point was determined using the 97% secant method, as previously described for three-point bending. The maximum force was determined manually, since the compressed samples continue to resist greater and greater loads even after initial failure.

Since extrinsic properties calculated from the RPC tests are strongly influenced by the platen size used, only intrinsic structural properties were reported for this test. Elastic modulus was calculated as

$$E = \frac{kh}{A_{platen}} \quad \textbf{(6)}$$

where *k* is the stiffness determined by the slope of the selected linear region, *h* is the measured specimen height, and A_{platen} is the measured area of the platen used in testing the specimen.

Stresses were calculated assuming purely uniaxial loading with a simple *F/A* equation:

$$\sigma_{yield} = \frac{F_{yield}}{A_{platen}} \quad \textbf{(7)}$$

$$\sigma_{ultimate} = \frac{F_{max}}{A_{platen}} \quad \textbf{(8)}$$

where F_{yield} and F_{max} are the forces of interest and A_{platen} is the measured area of the platen used.

Finally, the above structural properties were also normalized by µCT-measured bone volume fraction (BV/TV)[110]. This was done to account for the amount of cancellous bone in each specimen and should give a more valid approximation of the tissue-level properties of the cancellous bone tested during RPC.

3.2.7. Statistical Analysis of Mechanical Testing and µCT

Statistical analysis for µCT and mechanical tests (three-point bending and RPC) was performed in R (version 4.0.2). Where appropriate, a one-way ANOVA with a Tukey HSD post hoc test was used to compare differences between means of CON, HUC, SCL, and VJE groups. Only groups at the same experimental time point were compared. If ANOVA assumptions were not satisfied, means were compared with a Welch's ANOVA with a Games-Howell post hoc test, a Kruskal Wallis Test with a

Dunn's post hoc, or a robust linear multiple comparison method[111], as appropriate. Statistical significance was determined at $\alpha = 0.05$.

3.2.8. Finite Element Simulation

All distal femur metaphyses from the VJE ($n = 15$) and SCL ($n = 14$) animals euthanized at day 56 were used as samples for a linear finite element simulation of compression of cancellous bone. These groups and timepoints were selected to allow us to make another head-to-head comparison of jumping exercise and Scl-Ab treatment immediately after unloading. TIFF image stacks of each DFM specimen were generated during μCT scanning. These images were loaded into MATLAB (version 8.5, The MathWorks, Inc., Natick, MA), and binarized. The binarized image stacks were used to construct a three-dimensional model of the same volume that was cut from the DFM and used in physical RPC testing, cortical shell included. MATLAB was also used to mesh each specimen. To begin, all bone elements were assigned a standard elastic modulus of 10 GPa and Poisson's ratio of 0.3[112]. The resulting input files were uploaded to the Texas A&M High Performance Research Computing Ada cluster and executed on Abaqus (Dassault Systèmes, Vélizy-Villacoublay, France). The exact details of the above process are given in the work of Zachary Kohn[104]. His process was streamlined for this project but not substantively changed.

In this study, two loading cases were considered for each specimen (Figure 10). First, the RPC test described above was simulated. A circle located in the centroid of the cancellous region with a diameter 70% of the largest circle that could be inscribed within the cortical shell was found. Elements within this region in the most distal three layers of

the RPC volume were displaced 0.1 mm in the z-direction. The z-direction is parallel to the long axis of the femur bone, which is to say it is perpendicular to the cut surfaces of the specimens. Elements within the circular region on the most proximal three layers of the volume were fixed in the z-direction. A single node on the proximal face was fixed in the x- and y-directions to prevent rigid body motion. Otherwise, nodes were not constrained in the x- or y-direction. Specimens whose trabeculae were too sparse on the distal face to achieve adequate boundary nodes were excluded from analyses. A sample image for the RPC loading case is shown in Figure 10A, with orange arrows indicating boundary conditions.

The second loading case simulated was compression of the full, isolated cancellous structure, which is also called "full trabecular" loading in this study. The cancellous structure was isolated from the cortical shell using an image opening algorithm in MATLAB. Then, a displacement of 0.1 mm in the z-direction was applied to all nodes in the most distal three layers of nodes, while all nodes in the most proximal three layers were fixed in the z-direction. Again, a single point on the proximal face was fixed in the x- and y-directions to prevent rigid body motion, but nodes were otherwise not constrained in the x- or y-direction. A sample image for the full trabecular loading case is shown in Figure 10B, with orange arrows indicating boundary conditions.

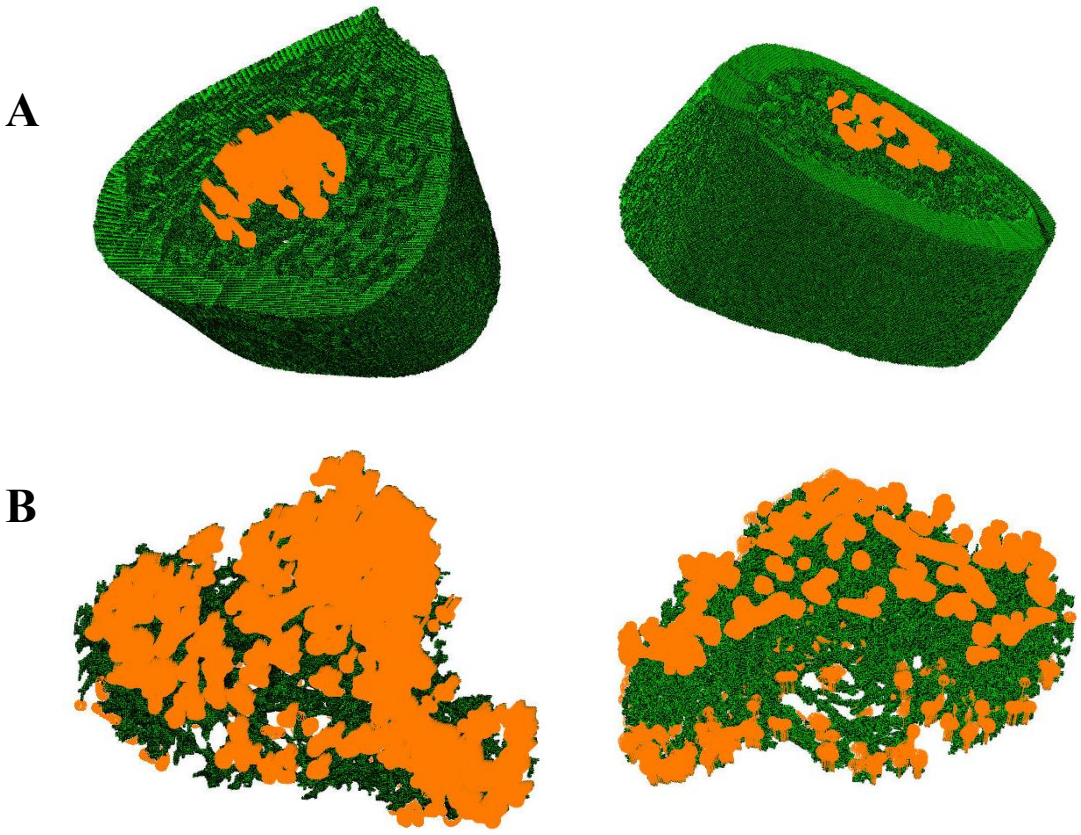

Figure 10. FEM boundary conditions.
Boundary conditions (indicated by orange markers) were applied to the top and bottom three layers of nodes for each type of FEM simulation. (A) Boundary conditions for FEM RPC simulations were applied to only nodes inside the virtual platen circle. (B) Boundary conditions for full trabecular compression were applied to all nodes in the top and bottom three layers of the model.

Post-processing was done in MATLAB. Specimens were assumed to yield when 5% of their elements reached 7000 microstrain[113]. This method was adapted from Pistoia et al., who used a similar method to predict fracture in FEM models of human distal radii. Strain of model elements was calculated with a strain-energy-based effective strain calculation[104],

$$U = \frac{1}{2}(\sigma_{max}\epsilon_{max} + \sigma_{mid}\epsilon_{mid} + \sigma_{min}\epsilon_{min}) \quad \textbf{(9)}$$

$$\epsilon_{eff} = \sqrt{\frac{2U}{E}} \quad \textbf{(10)}$$

where U is the strain energy density, $\sigma_{max,mid,min}$ are the principal stresses at the centroid of the element, $\epsilon_{max,mid,min}$ are the corresponding principal strains in the same direction, E is the elastic modulus of the material specified in the Abaqus model, and ϵ_{eff} is the effective strain at the centroid of the element.

The yield strain for each specimen was calculated as the strain at which the specimen's 95th percentile element would reach the critical strain (7000 microstrain),

$$\epsilon_y = \frac{\epsilon_{crit}}{\epsilon_{95}} * \frac{\Delta h}{h} \quad \textbf{(11)}$$

where ϵ_{95} is the effective strain at the centroid of the 95th percentile element, ϵ_{crit} is the critical strain, Δh is the applied displacement given in the model boundary conditions (0.1 mm), and h is the overall height of the specimen (2 mm). Only trabecular elements were considered when determining the 95th percentile element for RPC boundary conditions (BCs). All elements were considered for full trabecular compression BCs.

Yield stress was calculated as

$$\sigma_y = \frac{\epsilon_{crit}}{\epsilon_{95}} * \frac{F}{A} \quad \textbf{(12)}$$

where $\frac{\epsilon_{crit}}{\epsilon_{95}}$ is the same scaling factor used to calculate yield strain, F is the total reaction force exerted by the specimen, and A is the area over which the compressive displacement was applied to the model. For the RPC condition, A was set to the circular

area of boundary nodes. For the condition of compression of the full, isolated trabecular structure, *A* was set to the average of the total area of the top and bottom faces of the specimen. See Figure 11 below for a visual representation of the compressive areas.

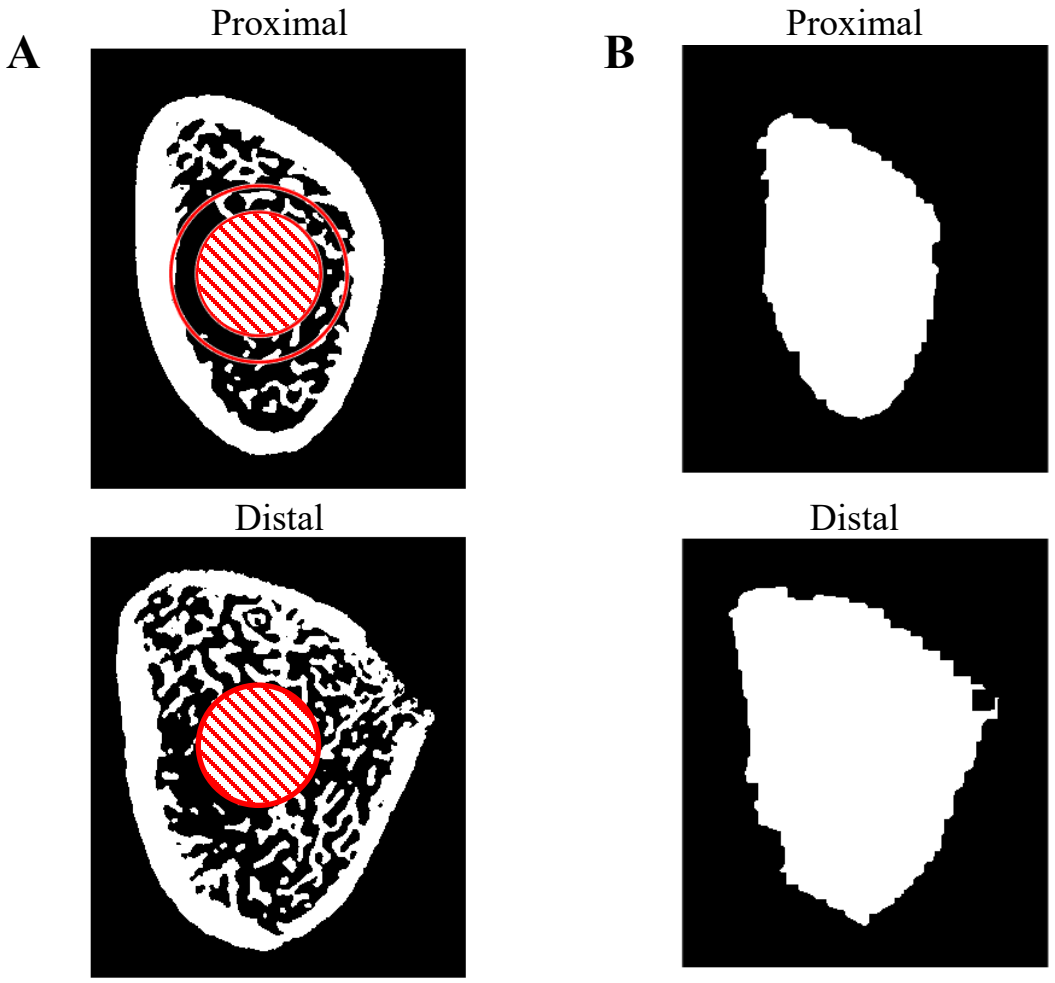

Figure 11. Compressive area for FEM model of RPC and full trabecular compression test simulations.
(A) Compressive area for RPC FEM simulation is the red-striped area of the virtual RPC platen. The outer red circle on the distal surface is the inscribed endocortical circle drawn by the input generation script in MATLAB. (B) Compressive area for full trabecular compression was set to the average of the trabecular areas of the distal and proximal faces (average of the two white regions).

Finally, the elastic modulus of each specimen was calculated as follows

$$E = \frac{\sigma_y}{\epsilon_y} \tag{13}$$

where σ_y and ϵ_y are the previously calculated yield stress and yield strain for the specimen.

After specimen properties were calculated based on the uniform tissue modulus applied in the Abaqus models, a new tissue modulus was calculated specimen by specimen using tissue mineral density from μCT scanning,

$$E_{tissue} = 1.127 * 10^{-4} BMD^{1.746} \tag{14}$$

This formula was previously used by Easley et al.[103] in finite element models of rat vertebrae. A unique tissue modulus was calculated for each specimen based on that specimen's tissue mineral density. Based on this specimen-specific tissue modulus, a scaling parameter was calculated for each specimen,

$$Ratio_E = \frac{E_{tissue,\mu CT}}{E_{tissue,Abaqus}} \tag{15}$$

where $E_{tissue,\mu CT}$ is the tissue modulus calculated from Equation (14), and $E_{tissue,Abaqus}$ is the tissue modulus specified in the Abaqus model (10 GPa). This scaling factor was multiplied by the previously calculated yield stress and specimen modulus to determine structural properties based partially on tissue mineral density.

Cancellous load share was calculated for the RPC-type simulations using the following equation[114]

$$\%\sigma_{cancellous} = 100 * \frac{\Sigma\sigma_{\text{axial,cancellous}}}{\Sigma\sigma_{\text{axial,all}}} \tag{16}$$

where $\Sigma\sigma_{axial,all}$ is the sum of all axial (z-direction) stresses reported by Abaqus in the middle two layers of elements, and $\Sigma\sigma_{axial,cancellous}$ is the sum of the axial stresses only from elements of those layers in the cancellous compartment.

Elastic modulus and yield stress from physical RPC testing and FEM simulation were correlated using a Pearson's R test. Physical RPC testing was correlated to both FEM-simulated RPC and to FEM simulation of full trabecular compression. For each boundary condition type, one correlation was performed with all animals pooled together, and a correlation was performed with the animals compartmentalized by VJE and SCL treatment group. Correlations compartmentalized by group are shown in Appendix B.

Means of VJE and SCL elastic modulus, yield stress, and yield strain were compared with a Welch's t-test. A non-parametric Wilcoxon rank sum test was used to compare means if the data were non-normal. All RPC comparisons were done with a Wilcoxon rank sum test (also known as a Mann-Whitney test) due to the low number of usable boundary conditions in the VJE group (n = 6). Significance was determined at α = 0.05.

4. RESULTS

4.1. Animals

Table 1 below gives the number of animals per group for the *ex vivo* measures presented in this study. Four animals were removed from the study due to poor adaptation to hindlimb unloading (HU). Otherwise, animals tolerated HU and our two pretreatments, jump training or Scl-Ab injections, without issue.

Table 1. Number of animals per group.

	Baseline	**End of Pretreatment**	**End of HU**	**End of Recovery**
	d0	*d28*	*d56*	*d112*
CON	7	18	16	22
HUC	---	---	13	14
VJE	---	15	15	15
SCL	---	15	14	15

CON = Ambulatory control
HUC = Hindlimb unloading control
VJE = Voluntary jumping exercise
SCL = Anti-sclerostin antibody treatment

Body weight of our animals was measured at each major timepoint (Figure 12).

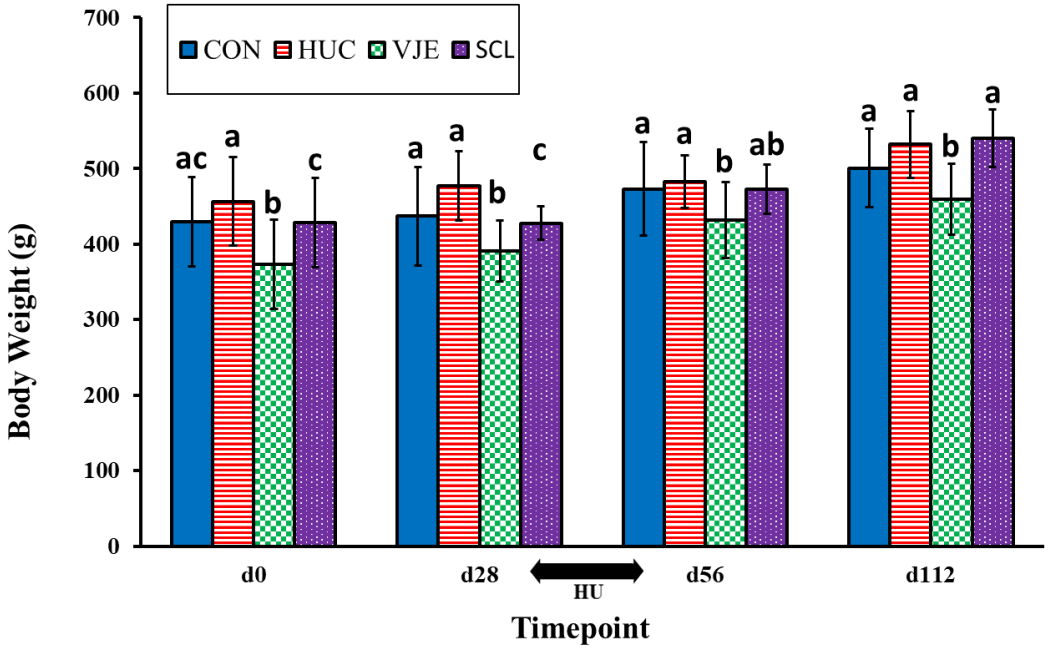

Figure 12. Animal body weights before and after 28 days of hindlimb unloading (HU).
Data are mean ± SD.
Groups at the same time point not sharing a letter are significantly different, $\alpha = 0.05$.
Note that *n* available for this *in vivo* measure (n = 14-63) were higher than for *ex vivo* analyses. All animal body weights were included at d0, and sample size decreases to ~15 as animals were terminated over the course of the study.

Starting from baseline (d0), VJE animals had lower body weight compared to all other groups (-13.26% vs CON, -18.33% vs HUC, -15.01% vs SCL). This trend continued at the end of pretreatment (d28), (-10.43%vs CON, -17.95% vs HUC, -9.35%vs SCL). At the end of unloading (d56) VJE animals had lower body weight than CON (-8.67%) and HUC (-10.56%), but their weight was not different from SCL rats. At the end of recovery (d112), the jumping animals still had lower body weight than all other groups (-8.18% vs CON, -13.53%vs HUC, -17.39%vs SCL). SCL animals had lower body weight than HUC animals at baseline (-6.07%). At the end of pretreatment,

SCL animals had lower body weight than CON (-2.06%) and HUC (-10.27%) animals. CON and HUC animals were no different in mean body weight at any time point.

4.2. Voluntary Jumping Exercise Validation

To validate our rat jumping model, ground reaction forces (GRFs) were measured during jumping to determine if the jumping protocol produces meaningful, osteogenic elevations in bone loading. We paired GRF measurements with pQCT at the femur and humerus and histomorphometry at the tibia and humerus to characterize the effects of jumping in the forelimbs and hindlimbs. These *ex vivo* measures were taken on animals terminated immediately after the exercise pretreatment (d28).

4.2.1. Ground Reaction Force Measurements

Mean peak vertical GRF during jumping and landing is presented as multiples of mean body weight in Figure 13 below. In addition, Figure 13 shows a comparison of loading rate (another important parameter affecting the bone response) between landing and jumping.

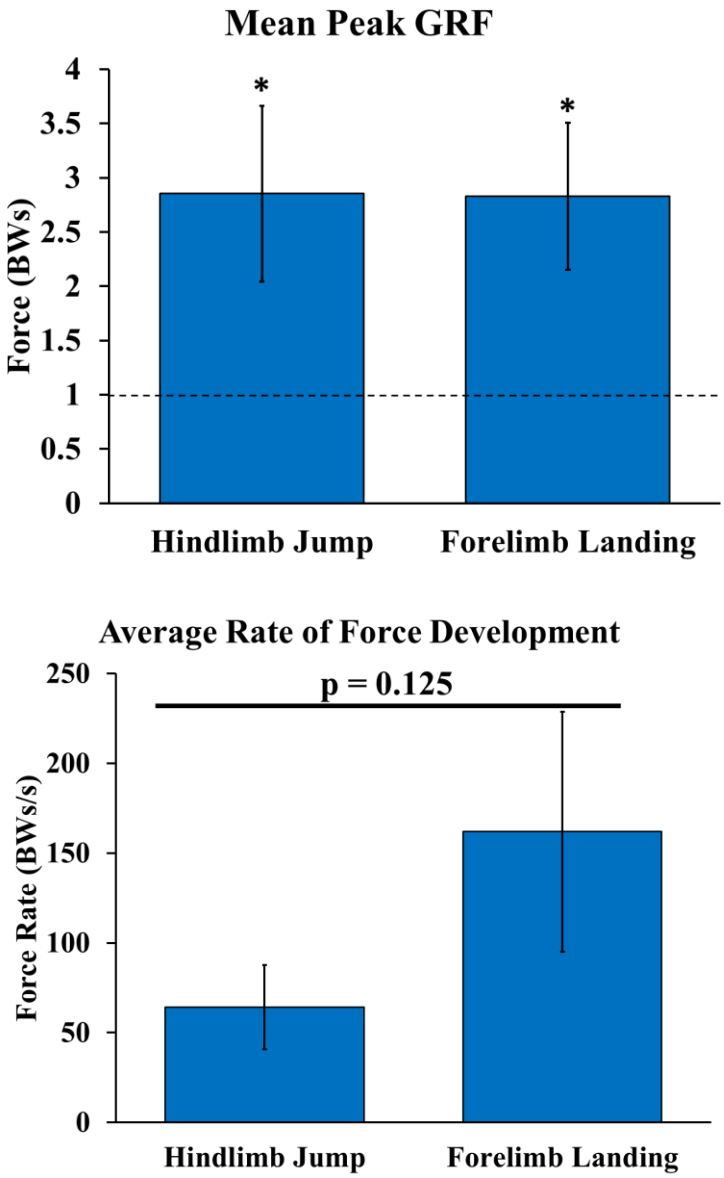

Figure 13. Mean peak vertical GRFs and average rate of force development as multiples of bodyweight during voluntary jumping exercise.
Data are mean ± SD.
*denotes peak GRF is significantly different from body weight, $\alpha = 0.05$.
Hindlimb jumps and forelimb landings were not significantly different, $\alpha = 0.05$.
$n = 4$ per group

Mean peak GRFs for hindlimb jumps and forelimb landings were both significantly higher than rat body weight (both 1.8x greater). There was no difference in the magnitude of GRF produced by jumping and landing. Forelimb landings produced an average rate of force development 1.5x greater than those of hindlimb jumps. This difference was not significant at $\alpha = 0.05$. However, force rate means did produce the greatest p-value achievable ($p = 0.125$) for the sign-test comparison of $n = 4$.

4.2.2. Bone Outcomes at the Forelimbs and Hindlimbs

To assess the effect of our jumping exercise on the bone structure and volumetric bone mineral density (vBMD) of our rats, we conducted pQCT scanning on metaphyseal regions of interest at the distal femur and proximal humerus. Cortical vBMD from the metaphyseal compartment for each bone site is illustrated in Figure 14.

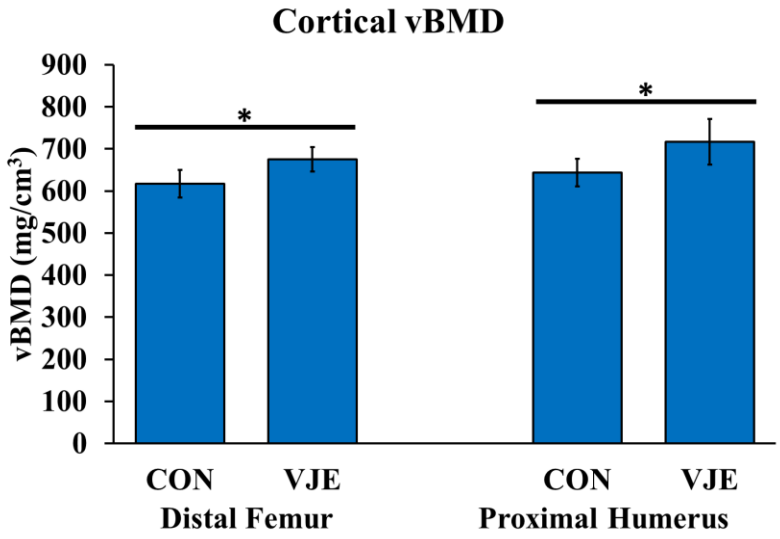

Figure 14. Cortical volumetric bone mineral density (vBMD) at the distal femur metaphysis and proximal humerus after 28 days of voluntary jump training, assessed by ex vivo pQCT.
Data are mean ± SD.
*denotes significantly different means, α = 0.05.
n = 9-10 per group

Cortical vBMD was higher at the distal femur metaphysis (DFM) and proximal humerus (PH) in VJE animals (+9% at DFM, +11% at PH). No differences were found in cancellous vBMD at either site. See Table A.3 of Appendix A for full pQCT data of VJE and SCL and d28.

Next, bone outcomes were further assessed with static histomorphometry at the proximal tibia metaphysis (PTM) and proximal humerus (PH). Cancellous %BV/TV (a measure of cancellous bone mass) at these two bone sites is shown below (Figure 15).

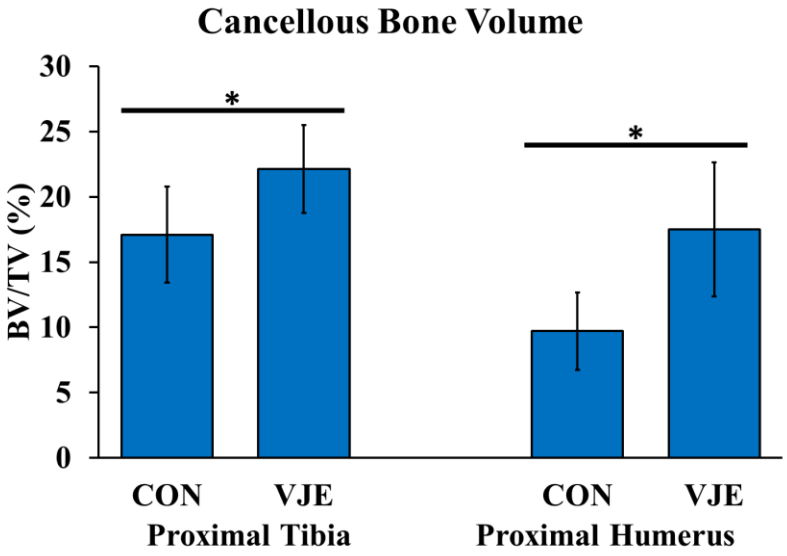

Figure 15. Percent cancellous bone volume per tissue volume (%BV/TV) at proximal tibia metaphysis and proximal humerus after 28 days of voluntary jump training.
Data are mean ± SD.
*denotes significantly different means, $\alpha = 0.05$.
n = 6-10 per group

BV/TV values were 30% higher in VJE rats vs. CON at the PTM and 80% higher at the PH.

Finally, bone cellular activity was assessed with histomorphometry at the proximal tibia metaphysis (PTM) and PH. Relative osteoclast surface, an indicator of resorptive activity, and kinetic indices of osteoblast activity are shown in Figure 16.

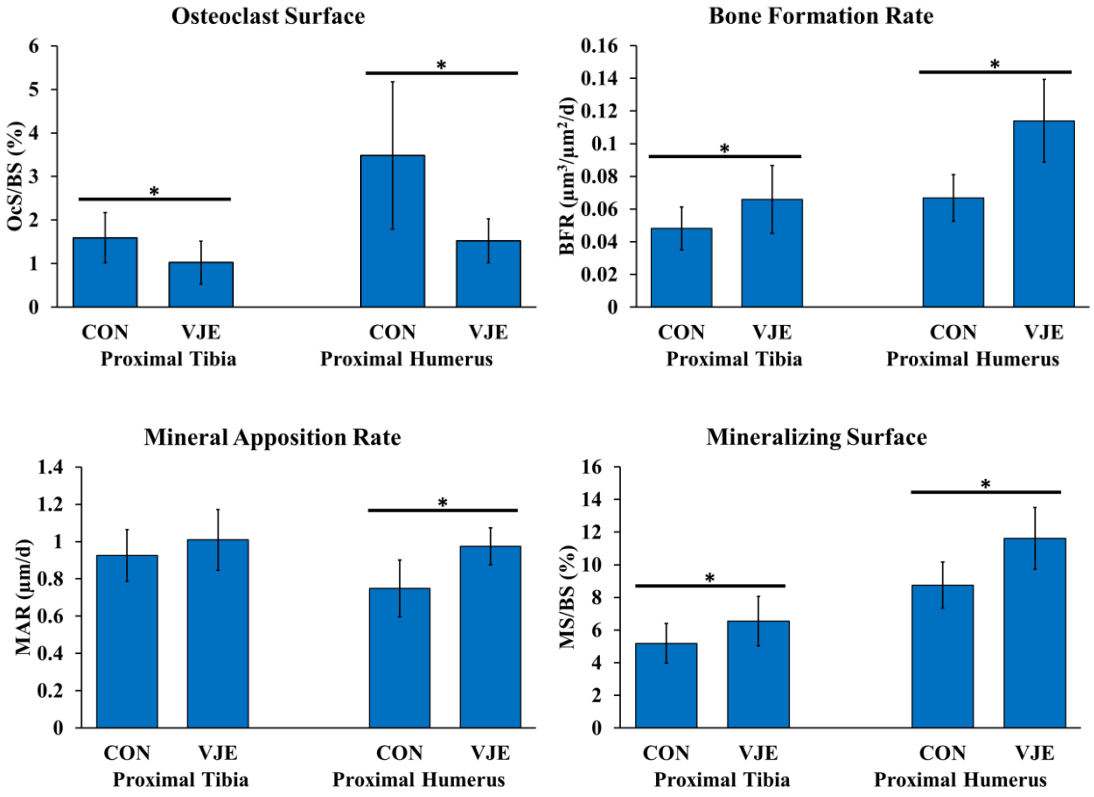

Figure 16. Relative osteoclast surface (%OcS/BS), bone formation rate (BFR), mineral apposition rate (MAR), and mineralizing surface (%MS/BS) at the proximal tibia metaphysis and proximal humerus after 28 days of voluntary jump training.
Data are mean ± SD. *n* = 6-10 per group
*denotes significantly different means, $\alpha = 0.05$.

Osteoclast surface, an indicator of the extent of bone resorption, was lower in jumping animals vs. that observed in CON at both sites (-36% at PTM, -53% at PH).

Mineral apposition rate (MAR; a measure of osteoblast "vigor") and % mineralizing surface (%MS/BS; a measure of how many osteoblast teams are actively forming bone) were elevated in the humerus of VJE animals (+30% and +33%, respectively). In the tibia, only mineralizing surface was elevated in VJE vs. CON (+26%). Hence, BFR (a product of MAR and %MS/BS) increased more dramatically at the PH (+71%) than at the PTM (+37%).

4.2.3. Jumping Validation Summary

Overall, our measurements of GRFs and bone outcomes in our jumping animals confirm that our exercise protocol elevates loading enough to be osteogenic in our animals' hindlimbs and forelimbs. We found elevated GRFs compared to body weight in the forelimbs and hindlimbs. Compared to sedentary controls, VJE animals showed significant improvements in bone formation rate, relative osteoclast surface, bone volume fraction, and cortical volumetric bone mineral density. However, percent differences in histomorphometric measures were much higher at the PH compared to the PTM.

4.3. Three-Point-Bend Mechanical Testing

A three-point-bend mechanical test was conducted at the femoral midshaft for all groups of animals at all time points. This test allowed us to assess the effects of our two treatments and unloading on the mechanical properties of cortical bone. Extrinsic properties (stiffness, ultimate force, and yield force) are shown on the following page (Figure 17).

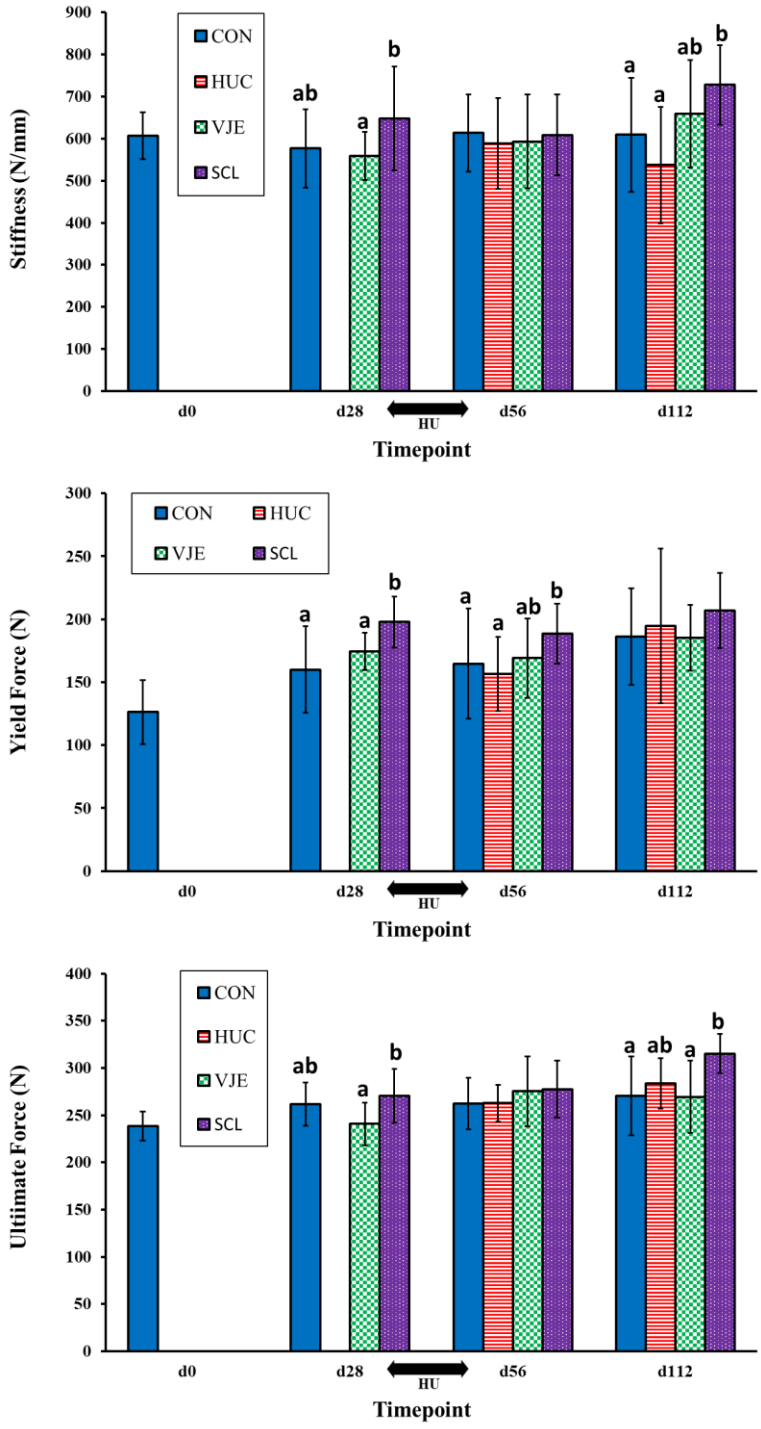

Figure 17. Extrinsic properties from three-point bending to failure at the femoral midshaft before and after 28 days of hindlimb unloading (HU).
Data are mean ± SD.
Groups at the same time point not sharing a letter are significantly different, $\alpha = 0.05$.
$n \sim 15$ per group

VJE, CON, and HUC were not statistically different from one another for any three-point bending extrinsic property. However, SCL animals did have elevated extrinsic properties compared to other groups. At the end of pretreatment, SCL yield force was enhanced above CON levels (+23.6%). In addition, SCL animals at the end of pretreatment exhibited significantly higher yield force, maximum force, and stiffness compared to VJE animals (+13.4%, +12.4%, and +15.8%, respectively). SCL enhancements in yield force (but not max force or stiffness) carried through unloading; SCL animals exhibited higher yield force than both CON (+14.4%) and HUC (+20.3%) at d56. At the end of recovery, SCL stiffness was elevated compared to HUC (+35.5%) and CON (+19.5%). At this same time point, SCL max force was elevated compared to CON (16.4%) and VJE (+16.9%), but not HUC.

Next, we examined intrinsic properties from this same three-point bending test. These properties indicate whether pretreatment or unloading had any impact on bone quality at the femoral midshaft. The intrinsic properties elastic modulus, yield stress, and ultimate stress are shown below in Figure 18.

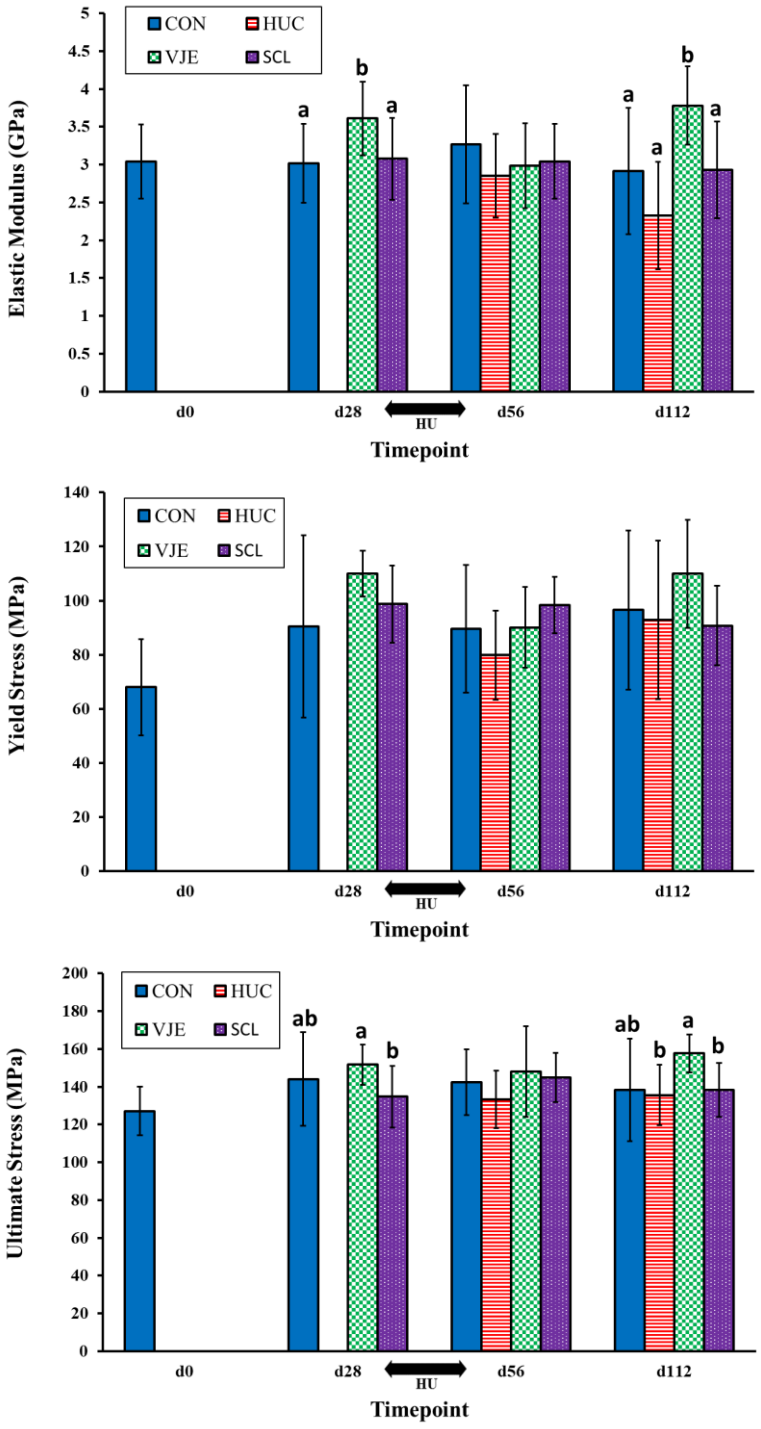

Figure 18. Intrinsic properties from three-point bending to failure at the femoral midshaft before and after 28 days of hindlimb unloading (HU).
Data are mean ± SD.
Groups at the same timepoint not sharing a letter are significantly different, $\alpha = 0.05$.
$n \sim 15$ per group

Unlike in extrinsic properties, SCL animals did not have significantly different means in any intrinsic property at any timepoint. Instead, VJE animals showed a few increases in intrinsic properties throughout the course of the study. At the end of pretreatment, VJE had elevated elastic modulus compared to CON (+19.7%) and SCL (+14.8%). In addition, VJE's ultimate stress was elevated compared to SCL (+11.2%). No significant differences in any intrinsic property emerged at the end of HU. However, at the end of recovery, VJE animals once again showed improvements in elastic modulus and ultimate stress. VJE had higher elastic modulus than all other groups at d112 (+29.5% vs CON, +62.7% vs HUC, + 29.1% vs SCL). In addition, VJE had elevated ultimate stress compared to HUC (+16.3%) and SCL (+12.3%). Yield stress showed no significant differences at any time point.

4.3.1. Three-Point Bend Summary

Interestingly, the improvements we found in three-point bending were not congruent between extrinsic and intrinsic properties. SCL animals showed improvements in stiffness, max force, and yield force at certain points in the study. However, SCL animals showed no improvements in the intrinsic properties of modulus, yield stress, and ultimate stress. Instead, VJE animals showed elevated modulus and ultimate stress at the end of pretreatment and at the end of recovery. So, it appears that Scl-Ab treatment improved the structural strength of the femoral midshaft, but not the material strength. The opposite appears to be true for jump training, which had no effect

on the bulk strength of the femoral midshaft, but did improve the material strength of the bone.

4.4. microCT Imaging at the Distal Femur

Cancellous bone microarchitecture at the distal femur metaphysis (DFM) was assessed with micro-computed tomography (μCT) for all animals and time points of this study. Results for bone volume fraction (BV/TV) and trabecular thickness at the DFM are presented in Figure 19 on the following page.

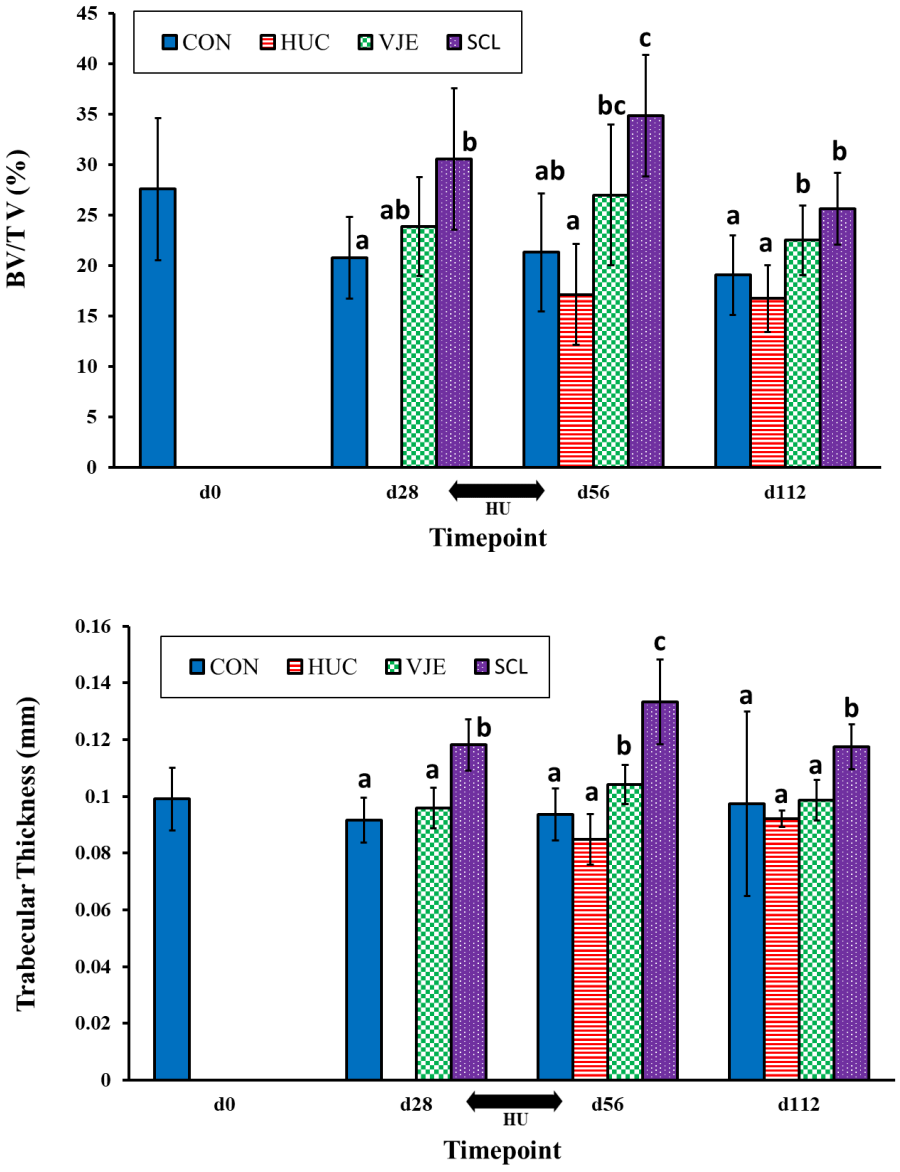

Figure 19. Cancellous microarchitecture (by µCT) at the distal femur metaphysis before and after 28 days of hindlimb unloading (HU)

Bone volume fraction (BV/TV), Trabecular thickness (Tb.Th)

Data are mean ± SD.

Groups at the same timepoint not sharing a letter are significantly different, $\alpha = 0.05$.

n ~ 15 per group

At the end of the pretreatment period, BV/TV of the SCL group was significantly elevated compared to CON (+47.2%). The SCL group also showed elevations in trabecular thickness (Tb.Th) compared to CON (+29.0%) and compared to VJE (+-23.2%). The VJE group was no different from CON in any μCT measure at the end of the pretreatment period.

After the 4-week unloading period, the benefits of sclerostin treatment persisted. In BV/TV and Tb.Th, SCL had elevated values compared to both reference groups: CON (+63.5% BV/TV, +42.3% Tb.Th) and HUC (+103% BV/TV, +57.1% Tb.Th). SCL also had elevated Tb.Th compared to VJE (+27.8%). Despite showing no statistically significant effects immediately after the exercise protocol, the VJE group had elevated BV/TV compared to HUC at the end of the unloading period (+57.6%). In addition, VJE had elevated Tb.Th compared to CON (+11.3%) and HUC (+22.9%). HUC was not significantly reduced compared to CON at the end of unloading for BV/TV or Tb.Th.

After unloading, animals recovered with normal cage activity for 8 weeks. At the end of recovery, SCL animals had elevated BV/TV compared to both reference groups (+34.5% vs CON, +53.2% vs HUC). SCL animals also had elevated Tb.Th compared to all other groups (+42.3 % vs CON, +57.1 % vs HUC, +27.8 % vs VJE). VJE showed elevations in only BV/TV compared to HUC (+34.5%) and CON (+18.0%).

We found no significant differences in trabecular spacing, trabecular number, or connectivity density at any time point. These data can be found in Table A.6 of Appendix A. Similarly, there were few statistically significant differences in trabecular tissue mineral density (TMD), as seen in Figure 20 below.

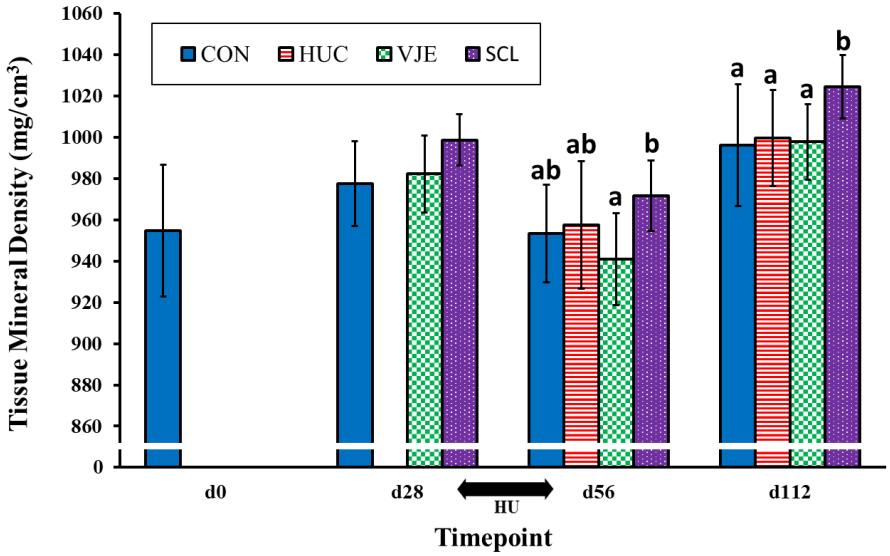

Figure 20. Cancellous tissue mineral density at the distal femur metaphysis before and after 28 d of hindlimb unloading (HU)
Data are mean ± SD.
Groups at the same timepoint not sharing a letter are significantly different, $\alpha = 0.05$.
$n \sim 15$ per group

After four weeks of unloading, TMD of SCL animals was elevated compared only to VJE (+3.3%). At the end of recovery, SCL animals had elevated vBMD compared to all other groups (+2.8% vs CON, +2.5% vs HUC, +2.7% vs VJE). Otherwise, no group comparisons reached significance at $\alpha = 0.05$. However, SCL did trend significantly higher than CON at d28 ($p = 0.0659$).

4.4.1. microCT Summary

Overall, treatment with Scl-Ab produced positive changes in cancellous bone in our rats. These enhancements persisted through 4 weeks of HU and through a subsequent 8-week recovery period. Our jumping exercise protocol produced no enhancements immediately after the 4-week pretreatment, but VJE animals did exhibit

elevated BV/TV and Tb.Th compared to reference groups 4 weeks and 12 weeks after exercise ceased. So, it seems that exercise had delayed benefits on the cancellous bone of the rat femur. However, Scl-Ab treatment produced more statistically significant enhancements and greater percent differences than exercise did. In addition, SCL had elevated tissue mineral density at d112 and elevated Tb.Th at all timepoints when directly compared to VJE. Thus, μCT suggests that Scl-Ab treatment was more anabolic than jumping exercise in the cancellous bone of the DFM.

4.5. Reduced Platen Cancellous Compression

The mechanical strength of the same DFM cancellous structure was evaluated with reduced platen compression (RPC). Standard RPC structural measures were further normalized by BV/TV to give a better approximation of material-level cancellous properties. Elastic modulus as measured by RPC is shown on the next page in Figure 21.

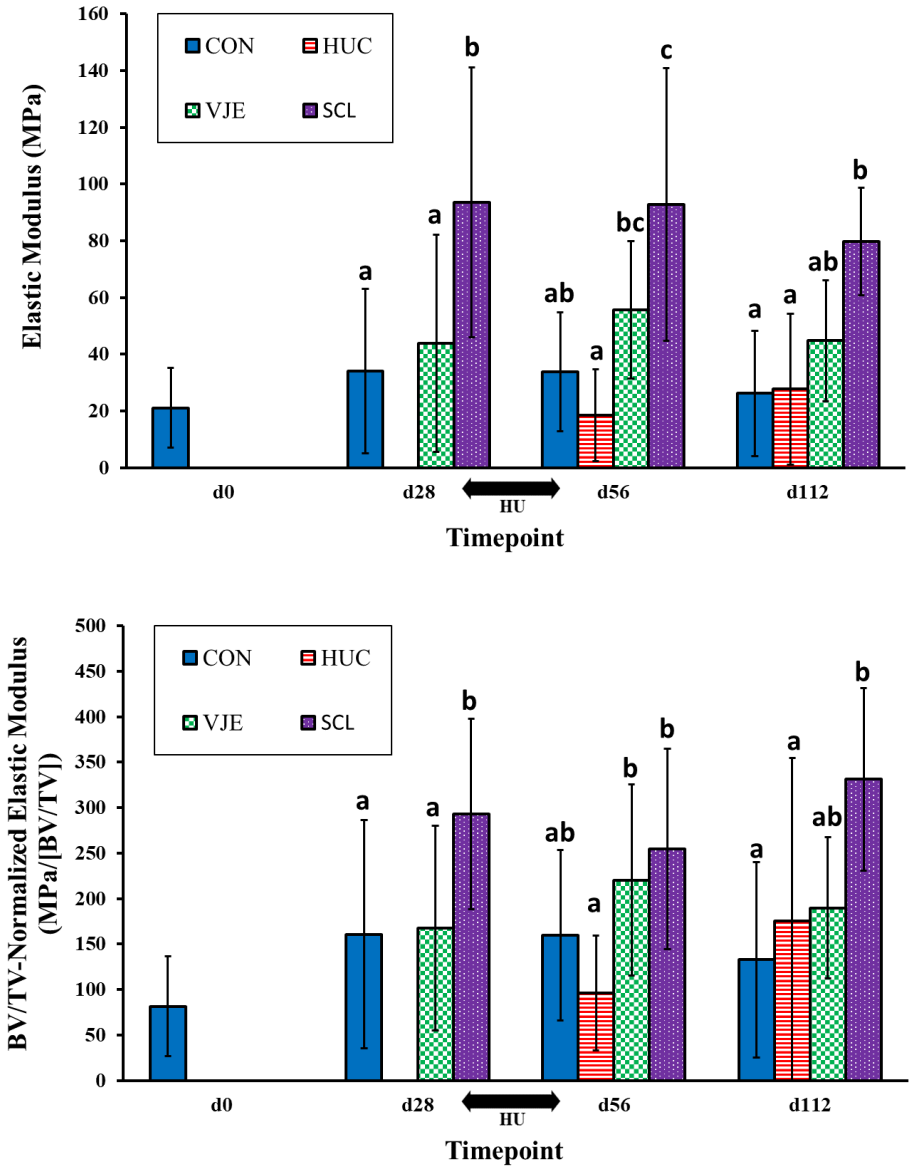

Figure 21. Elastic modulus (absolute and relative to BV/TV) of distal femur cancellous bone as determined by reduced platen compression testing before and after 28 days of hindlimb unloading (HU).
Data are mean ± SD.
Groups at the same timepoint not sharing a letter are significantly different, $\alpha = 0.05$.
n ~ 15 per group

At the end of pretreatment, SCL modulus was elevated compared to CON (+175.5%) and VJE (+113.5%) and remained enhanced above CON levels at the end of unloading (+174.4%). SCL modulus was also 5 times higher than HUC modulus immediately after the unloading period. These increases persisted in SCL vs HUC (+188.1%) and CON (+203.8%) at the end of recovery. VJE modulus was elevated compared to HUC (+66.6%) at the end of unloading, but VJE was otherwise not different from either reference group at any time point.

We then normalized these results by μCT-measured BV/TV to account for the amount of cancellous bone in each specimen, creating a more valid approximation of the tissue-level properties of the cancellous bone[110]. After normalization by BV/TV, group comparisons were largely unchanged. As before, SCL modulus was elevated compared to CON (+82.5%) and VJE (+74.9%) at the end of pretreatment. SCL normalized modulus was higher only than HUC (+164.7%) at the end of unloading. Increases persisted in SCL vs HUC (+88.8%) and CON (+149.4%) at the end of recovery. VJE modulus was elevated compared to HUC at the end of unloading (+129.2%), but VJE was otherwise not different from either reference group.

Yield stress showed very similar trends in group differences to elastic modulus. Yield stress measured by RPC is presented on the following page with and without normalization by BV/TV (Figure 22).

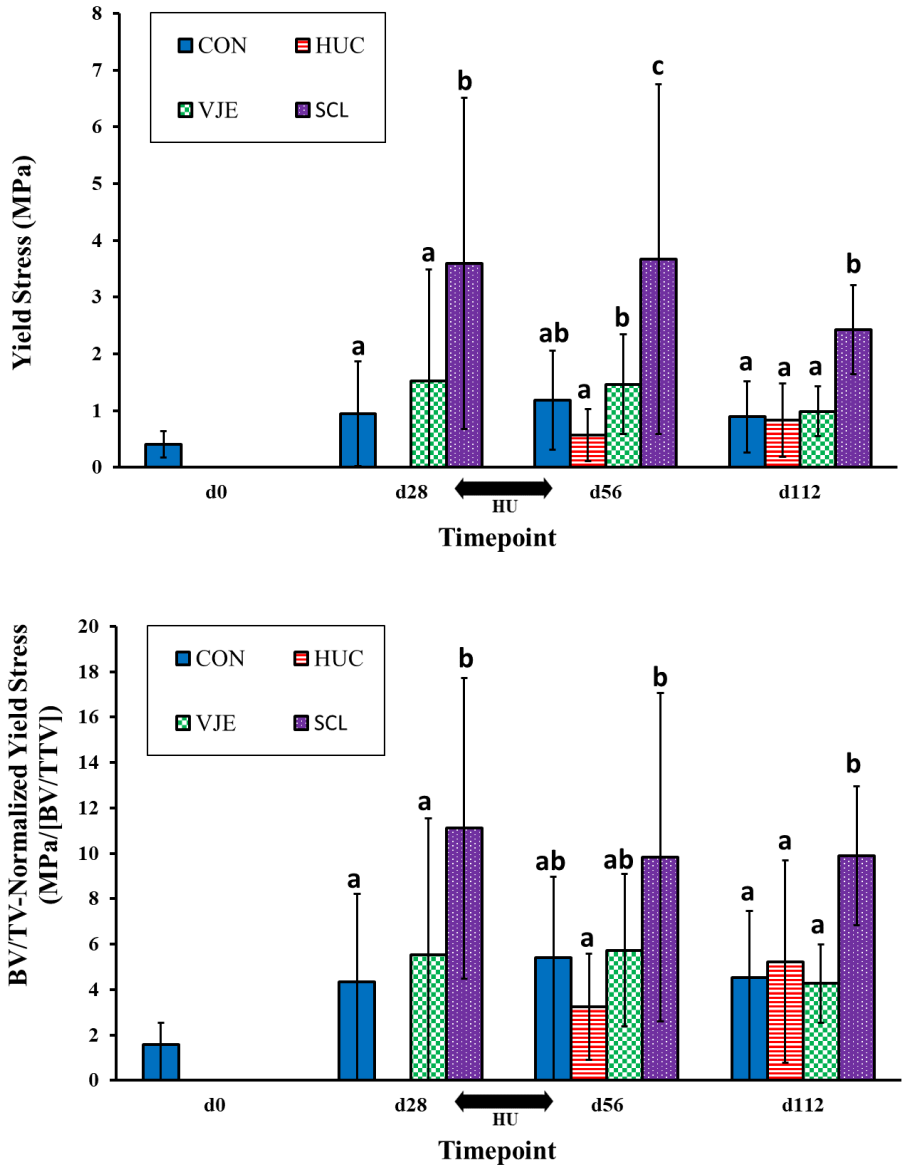

Figure 22. Yield stress (absolute and relative to BV/TV) of distal femur cancellous bone as determined by reduced platen compression testing before and after 28 days of hindlimb unloading (HU).
Data are mean ± SD.
Groups at the same timepoint not sharing a letter are significantly different, $\alpha = 0.05$.
$n \sim 15$ per group

At the end of pretreatment, SCL yield stress was elevated compared to CON (+280.6%) and VJE (+135.5%). SCL yield stress remained higher than all other groups after unloading (+208.8% vs CON, +545.6% vs HUC, +150.1% vs VJE). These increases in SCL vs all other groups persisted at the end of recovery (+172.5% vs CON, +190.0% vs HUC, +145.2% vs VJE). VJE yield stress was elevated compared to HUC at the end of unloading (+158.1%), but VJE was otherwise not different from either reference group at any time point.

Just as with RPC elastic modulus, normalization of yield stress by BV/TV did not greatly affect group comparisons. At the end of pretreatment, SCL normalized yield stress was still elevated compared to both CON (+155.2%) and VJE (+100.4%). However, after unloading, SCL was higher than only HUC (+203.5%). By the end of recovery, SCL was once again elevated vs all other groups (+118.8% vs CON, +89.3% vs HUC, +131.9% vs VJE). VJE normalized yield stress was not different from either reference group at any point.

A final mechanical property, RPC ultimate stress follows the same trends as yield stress and modulus. This can be seen in Figure 23 on the following page.

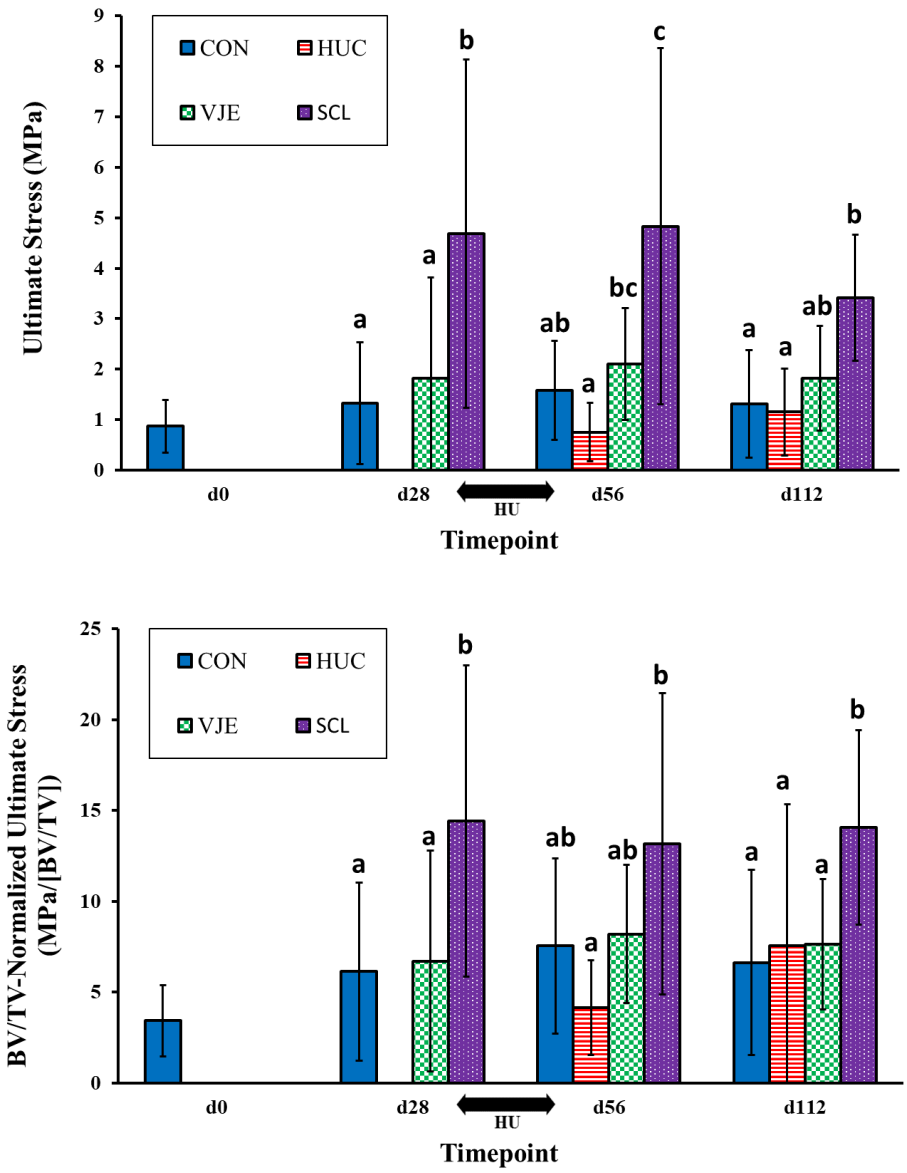

Figure 23. Reduced platen compression ultimate stress
Data are mean ± SD.
Groups at the same time point not sharing a letter are significantly different, $\alpha = 0.05$.
n ~ 15 per group

At the end of pretreatment, SCL ultimate stress was elevated compared to CON (+253.5%) and VJE (+157.3%). SCL ultimate stress remained enhanced above CON levels (+206.9%) and was higher than HUC (+545.1%) at the end of unloading. These increases persisted in SCL vs HUC (+197.1%) and CON (+161.0%) at the end of recovery. VJE ultimate stress was elevated compared to HUC at the end of unloading (+129.5%), but VJE was otherwise not different from either reference group.

As before, normalization by BV/TV did not greatly affect group comparisons of ultimate stress. At the end of pretreatment, SCL normalized ultimate stress was still elevated compared to both CON (+135.2%) and VJE (+115.0%). However, after unloading, SCL was higher than only HUC (+217.1%). By the end of recovery, SCL normalized ultimate stress was elevated compared to all other groups (+112.1% vs CON, +-85.6% vs HUC, +84.2% vs VJE). VJE normalized ultimate stress was not different from either reference group at any point.

4.5.1. RPC Summary

Overall, RPC testing found potent gains in trabecular bone mechanical strength from Scl-Ab treatment. Scl-Ab enhanced every cancellous mechanical property above ambulatory control levels at every timepoint, including immediately after the end of hindlimb unloading. Jumping exercise produced no enhancements above control levels, but it did protect cancellous bone strength from losses caused by hindlimb unloading. VJE values were higher than HUC at the end of unloading for every non-normalized property. In addition, VJE values were never lower than CON, despite VJE animals going through 28 days of unloading. Normalizing mechanical properties by BV/TV had

little effect on the overall trends seen in RPC testing. However, normalization did close the gap somewhat between SCL and all other groups. This can be seen visually, and it is reflected in the percent differences reported, which are lower after normalization where SCL is involved.

4.6. Finite Element Method Simulation of Cancellous Bone Compression Testing

To better understand the results of our physical RPC testing, we conducted finite element method (FEM) simulation on VJE and SCL specimens from day 56 (end of unloading). We conducted simulations using two different model configurations. We simulated the physical RPC test that we conducted, and we isolated the RPC specimens' trabecular structure from the cortical shell and simulated compression of that entire, isolated trabecular compartment. This branch of the study is less focused on rigorously comparing treatments than the previous sections. We did use FEM to further compare the effects of Scl-Ab and our jump training on bone integrity at the end of the 28-day unloading period. However, we primarily undertook this simulation hoping to more qualitatively understand the behavior of our physical RPC test and to refine our FEM modeling procedure.

4.6.1. Boundary Conditions

We began our FEM analysis by examining the boundary conditions we applied to our 3D models. Figure 24 and Figure 25 show the nodes where boundary conditions were applied at the top face for the full trabecular compression case. This study's labeling convention was to label SCL animals "X####" and VJE animals "J####."

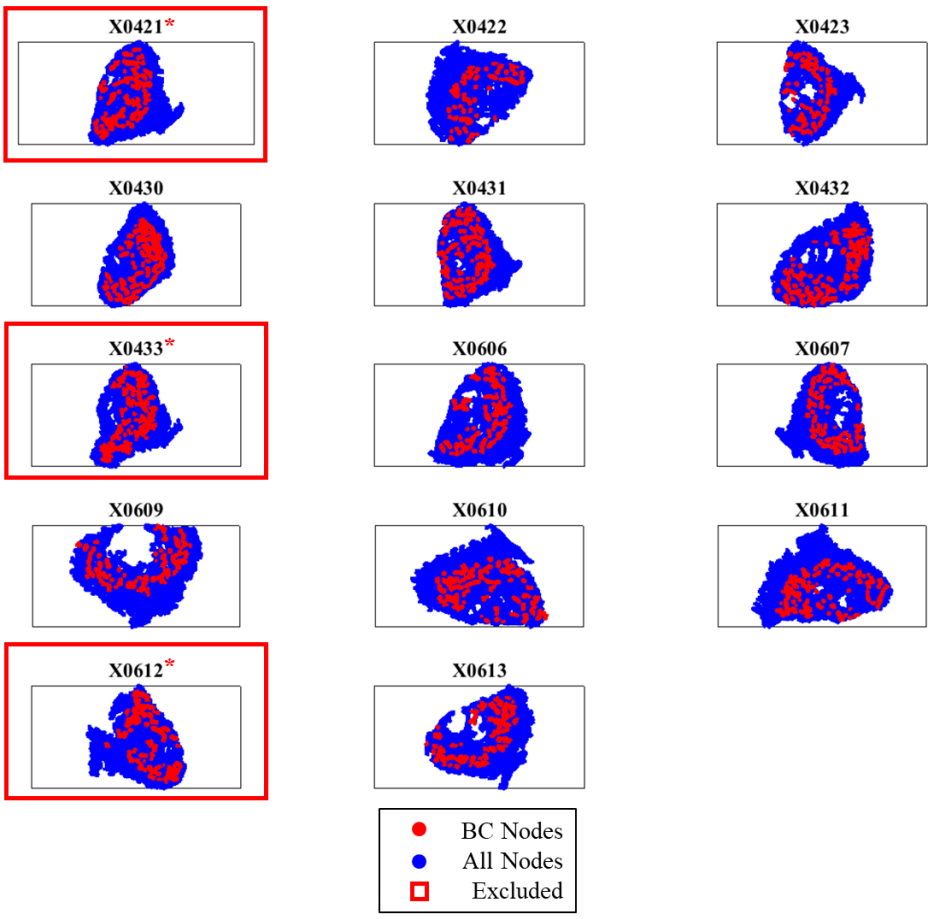

Figure 24. Top face boundary nodes for full trabecular compression of SCL specimens

0.1 mm of displacement was applied to each red BC node. Blue nodes are all nodes of the 3D model of each specimen projected onto a 2D plane. Only top face BC nodes are shown, as the top face was the limiting factor for sample inclusion. *X0421, X0433, and X0612 were excluded because the MATLAB image segmenting procedure incorrectly categorized a large portion of the trabecular structure as cortical bone.

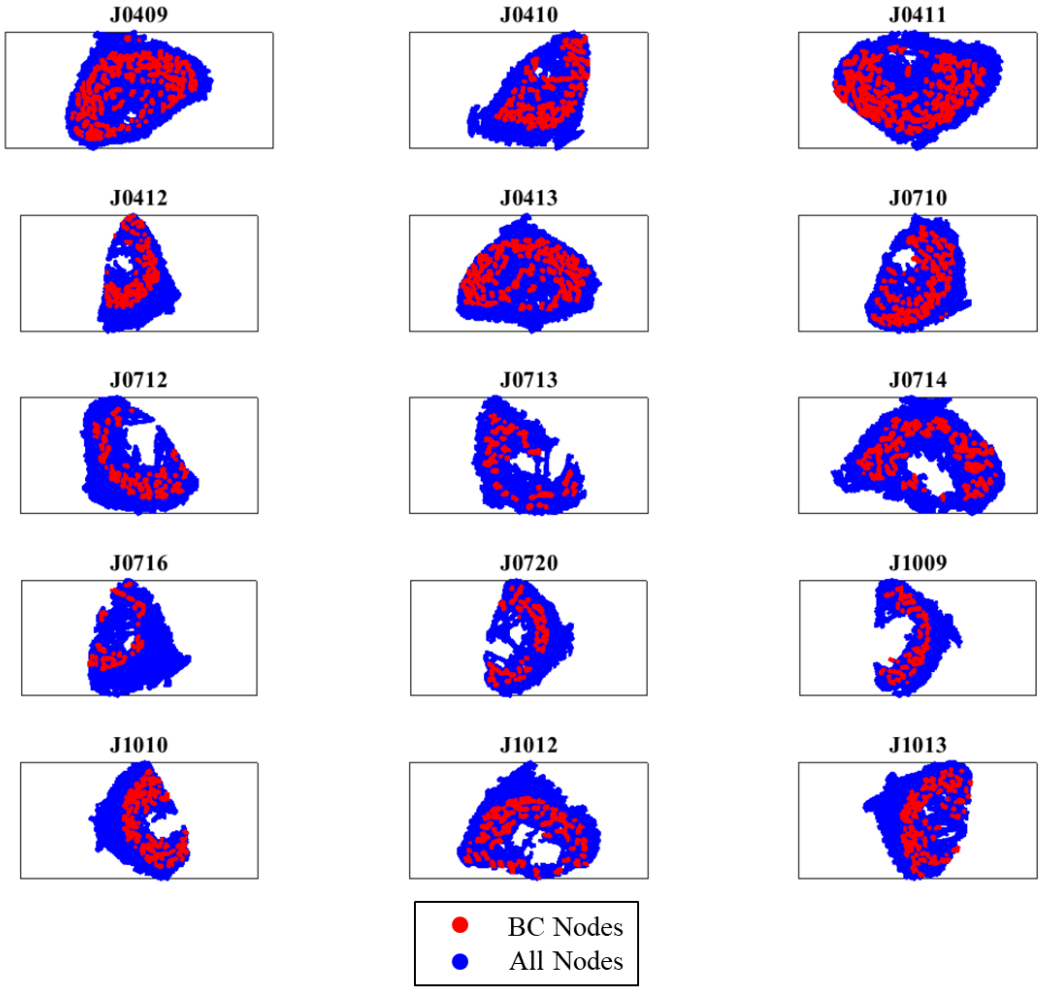

Figure 25. Top face boundary nodes for full trabecular compression of VJE specimens
0.1 mm of displacement was applied to each red BC node. Blue nodes are all nodes of the 3D model of each specimen projected onto a 2D plane. Only top face BC nodes are shown, as the top face was the limiting factor for sample inclusion.

The boundary conditions of full trabecular compression visually seem to have been successfully applied for all VJE and SCL animals. Boundary conditions were applied to the majority of nodes on the top face of the models. However, three SCL trabecular simulations were excluded because the MATLAB image segmenting procedure incorrectly categorized a large portion of the trabecular structure as cortical

bone. No other full trabecular compression simulations were excluded from this study. Figure 26 below shows the improper differentiation of cortical and cancellous bone in the three excluded SCL specimens.

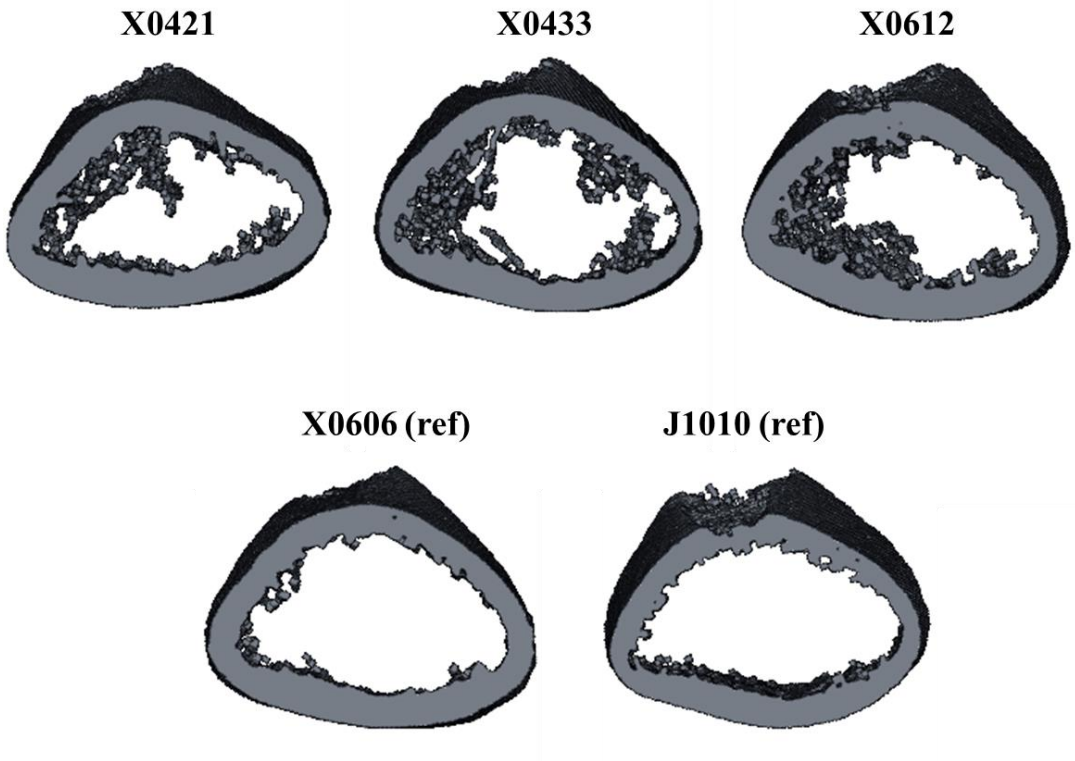

Figure 26. Bone categorized as cortical in excluded SCL simulations.
X0421, X0433, and X0612 were excluded from trabecular simulations due to improper inclusion of cancellous bone along with the cortical shell. X0606 and J1010 are representative of the accuracy of cortical differentiation in other specimens.

X0421, X0433, and X0612 were excluded from trabecular simulations. The elements categorized as cortical shell included a large number of trabecular elements. The trabecular elements in the top three panels of Figure 26 are the irregular structures

that intrude towards the center of the otherwise empty cancellous space. These irregular intrusions are not present in the bottom two panels, which are representative of the typical accuracy of our cortical-trabecular separation algorithm. The top specimens in the top three panels of Figure 26 were excluded from full trabecular simulation outcomes and yield outcomes of RPC simulations, as both of those categories required accurate distinction of trabecular and cortical elements. No other specimens were excluded for this reason.

On the other hand, many samples were excluded in the RPC configuration. Boundary condition nodes for RPC simulations are shown in Figure 27 and Figure 28 on the following pages.

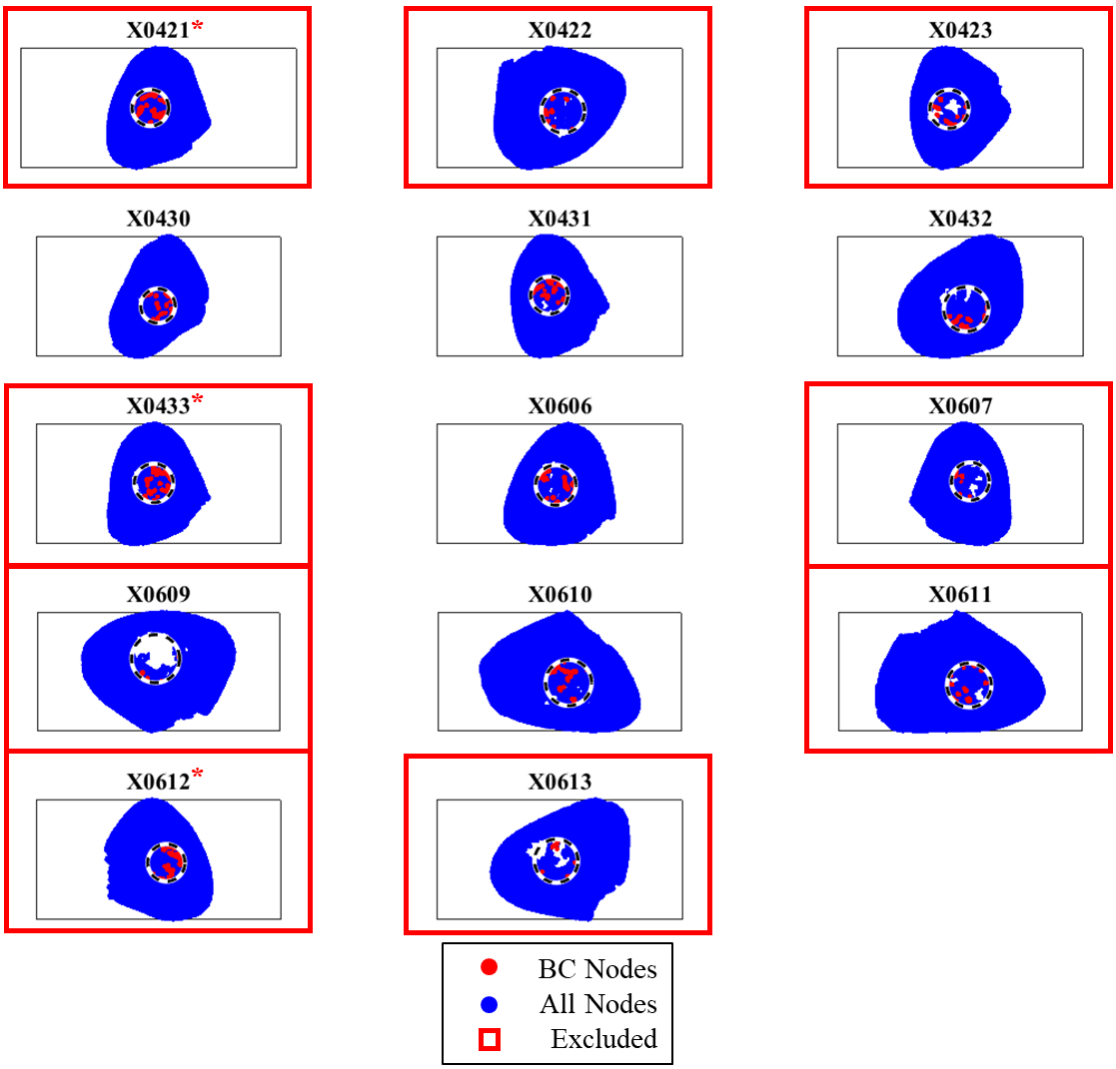

Figure 27. Top face boundary nodes for RPC compression of SCL specimens
*X0421, X0433, and X0612 were excluded for only measures of yield because the MATLAB image segmenting procedure incorrectly categorized a large portion of the trabecular structure as cortical bone. Other samples were excluded due to having too few BC nodes. Calculated platen area is shown by the black dotted line circle. Only nodes within this circle were considered for boundary nodes. 0.1 mm of displacement was applied to each red BC node. Blue nodes are all nodes of the 3D model of each specimen projected onto a 2D plane. Only top face BC nodes are shown, as the top face was the limiting factor for sample inclusion.

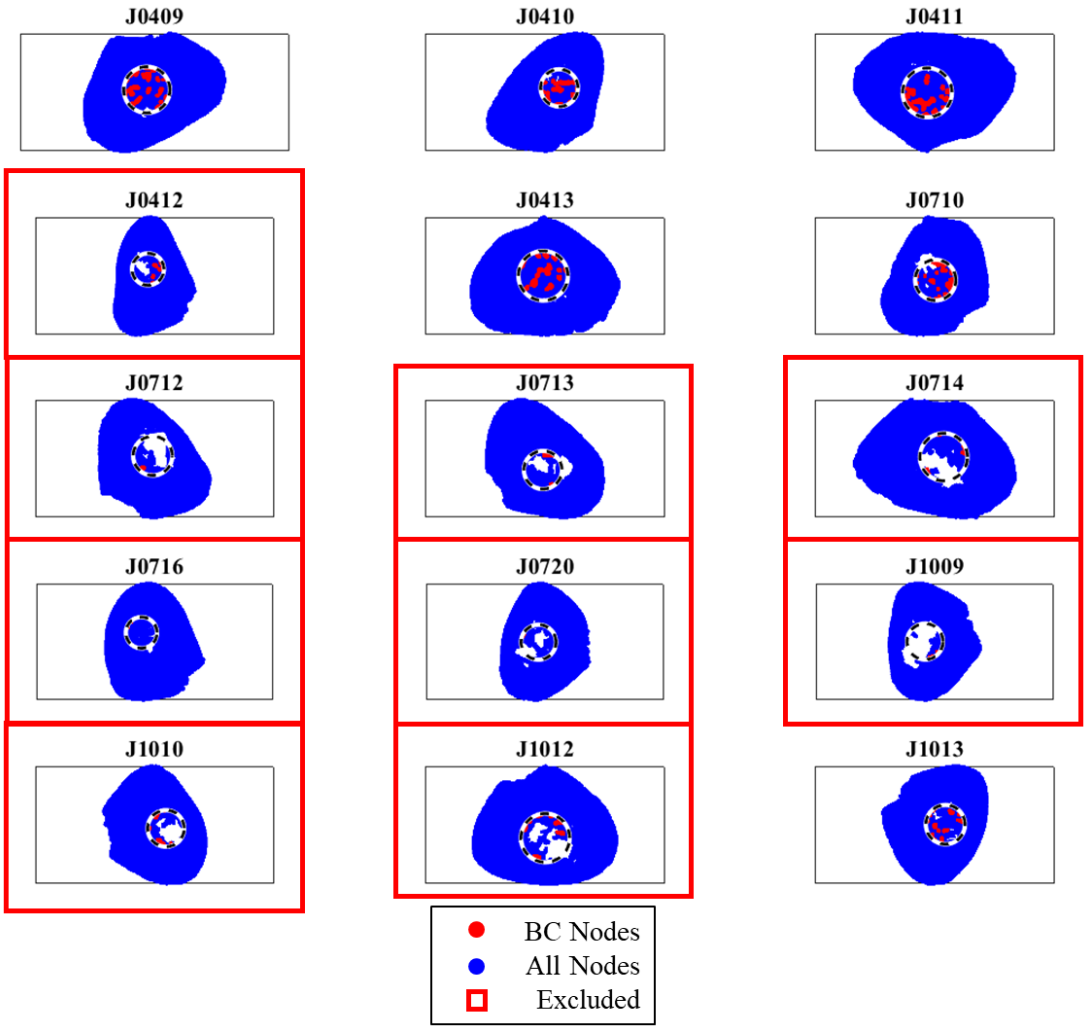

Figure 28. Top face boundary nodes for RPC compression of VJE specimens Samples were excluded due to having too few BC nodes. Calculated platen area is shown by the black dotted line circle. Only nodes within this circle were considered for boundary nodes. 0.1 mm of displacement was applied to each red BC node. Blue nodes are all nodes of the 3D model of each specimen projected onto a 2D plane. Only top face BC nodes are shown, as the top face was the limiting factor for sample inclusion.

Six RPC SCL models and nine RPC VJE models were excluded from this study because the top face was too sparse to support meaningful BC nodes. In addition, three SCL simulations were excluded because the model generation script improperly categorized a large portion of their especially-dense trabecular structures as cortical

bone. This mistake does not affect calculations of elastic modulus. However, it does alter the search volume for yielded elements, so measures of yield were excluded for these simulations.

4.6.1.1. Boundary Conditions Summary

Full trabecular compression boundary conditions were applied without issue, but 3/14 SCL simulations were excluded due to poor peeling of the cortical elements from the trabecular elements. RPC boundary conditions were problematic. In total, 9/15 VJE models were excluded, and 9/14 SCL models were excluded. All but three of these models were excluded because the trabecular structure of their top faces was too sparse for boundary conditions to be adequately applied.

4.6.2. FEM Mechanical Properties

After excluding problematic simulations, we calculated mechanical properties for those remaining. We did this first without altering the standard tissue elastic modulus that was assigned to all models during model generation. Then, we scaled the resulting specimen moduli and yield stresses using specimen-specific tissue moduli that we calculated from μCT tissue mineral density (TMD). This calculation used a relationship between TMD and tissue modulus derived from a variety of species that was previously applied in finite element modeling of rat vertebrae[103]. VJE and SCL group comparisons for scaled and unscaled specimen-level elastic modulus are shown in Figure 29. Group comparisons were performed only within a single model configuration; no statistical comparisons were performed between RPC simulations and full trabecular compression (Trab) simulations for any property.

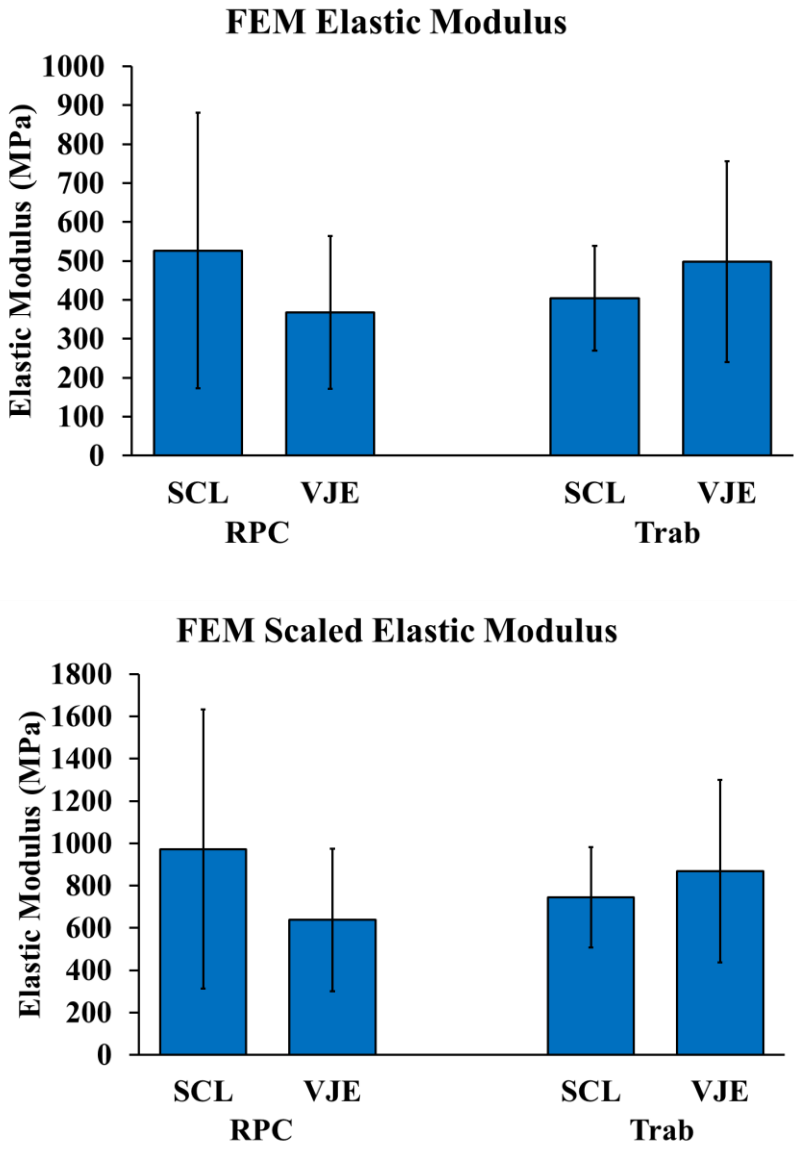

Figure 29. FEM elastic modulus treatment comparison
"Scaled Elastic Modulus" was calculated using specimen-specific tissue modulus scaled by µCT TMD.
Data are mean ± SD.
No group comparisons were statistically significant, $\alpha = 0.05$.
n = 11-15 per Trab group
n = 6-8 per RPC group

Specimen elastic modulus was not different between VJE and SCL, regardless of the model configuration and use of scaled or unscaled tissue modulus. Scaling tissue elastic modulus did not produce statistically significant comparisons or alter the visual trends of the results. The main effect of scaling with TMD was increasing the magnitude of the mean modulus by 170-180%. Magnitudes of elastic modulus were fairly comparable between the RPC and full trabecular model configurations. However, in RPC simulations SCL was non-significantly higher than VJE, while the opposite was true for full trabecular simulations.

Out next outcome, estimated yield stress, can be found below in Figure 30.

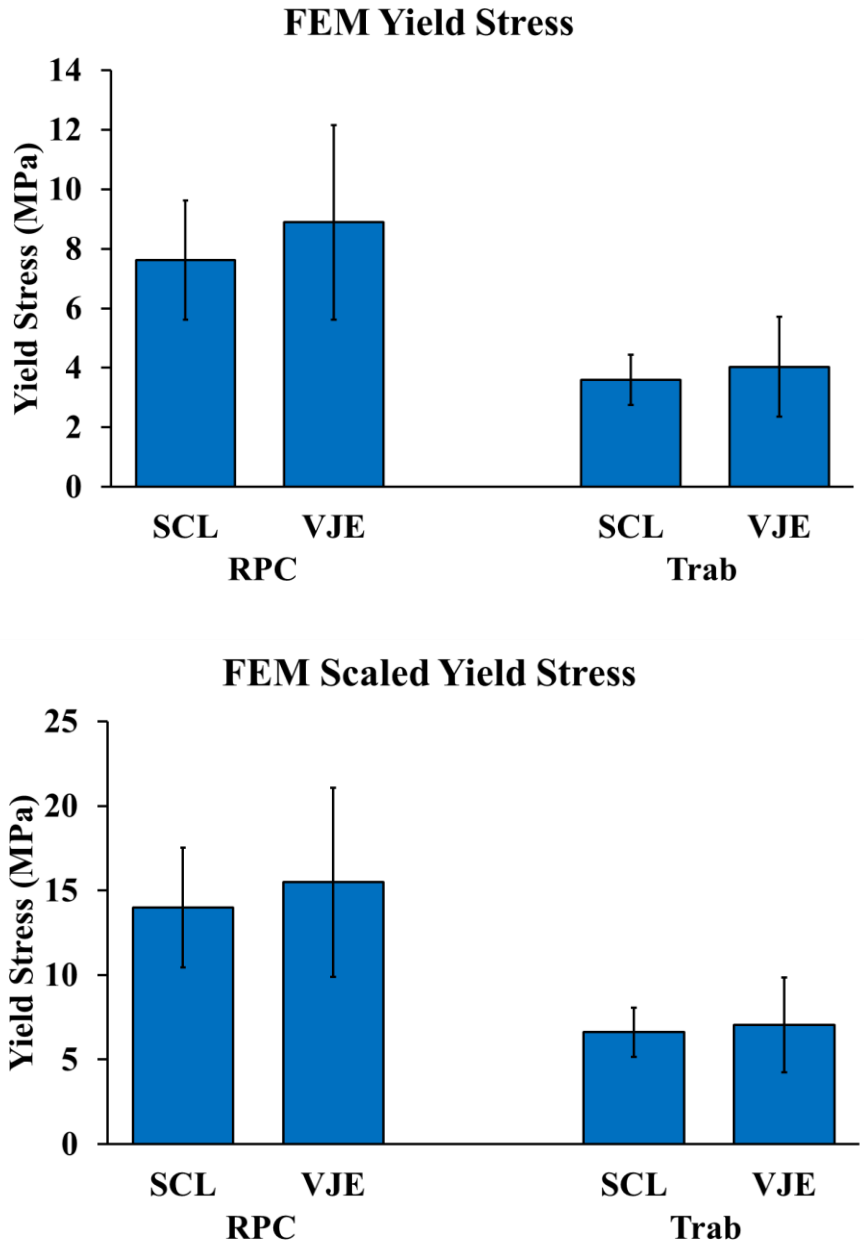

Figure 30. FEM yield stress treatment comparison
"Scaled Yield Stress" was calculated using specimen-specific tissue elastic modulus scaled by µCT TMD.
Data are mean ± SD.
No group comparisons were statistically significant, $\alpha = 0.05$.
n = 11-15 per Trab group
n = 5-6 per RPC group

As with specimen elastic modulus, VJE and SCL mean yield stress means were not statistically different, regardless of the model configuration and use of scaled or unscaled tissue modulus. Also, as before, scaling tissue modulus with TMD uniformly increased the magnitude of the mean yield stresses by 170-180%, but did not differentiate groups from one another. Magnitudes of RPC yield stress were much higher compared to Trab simulations (2.1-2.8 times higher, but not statistically compared).

A final mechanical property that we examined was estimated yield strain, presented below in Figure 31.

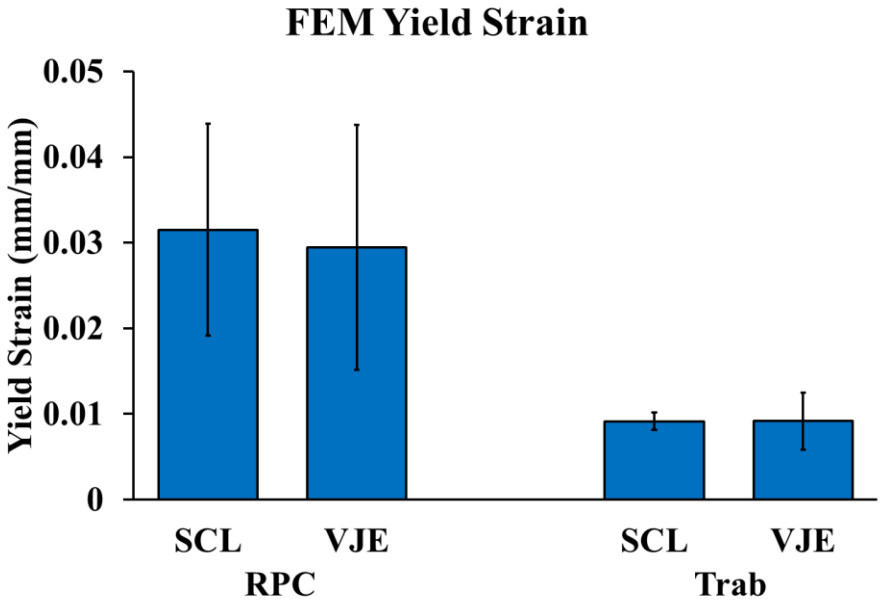

Figure 31. FEM yield strain treatment comparison
Data are mean ± SD.
No group comparisons are statistically significant, $\alpha = 0.05$.
n = 11-15 per Trab group
n = 5-6 per RPC group

RPC mean yield strain was not different between SCL and VJE for the RPC or full trabecular configuration. The average RPC yield strains were 3.2-3.4 times higher

than full trabecular yield strains (but again were not statistically compared). Scaling tissue modulus with TMD does not affect strain.

Next, we examined the fraction of the total load carried by trabecular bone in the RPC simulations (Figure 32). This measure gives us insight into the influence of the cortical shell on RPC testing. (We would prefer the cortical influence to be nonexistent, as we intend to evaluate just trabecular bone with RPC testing.)

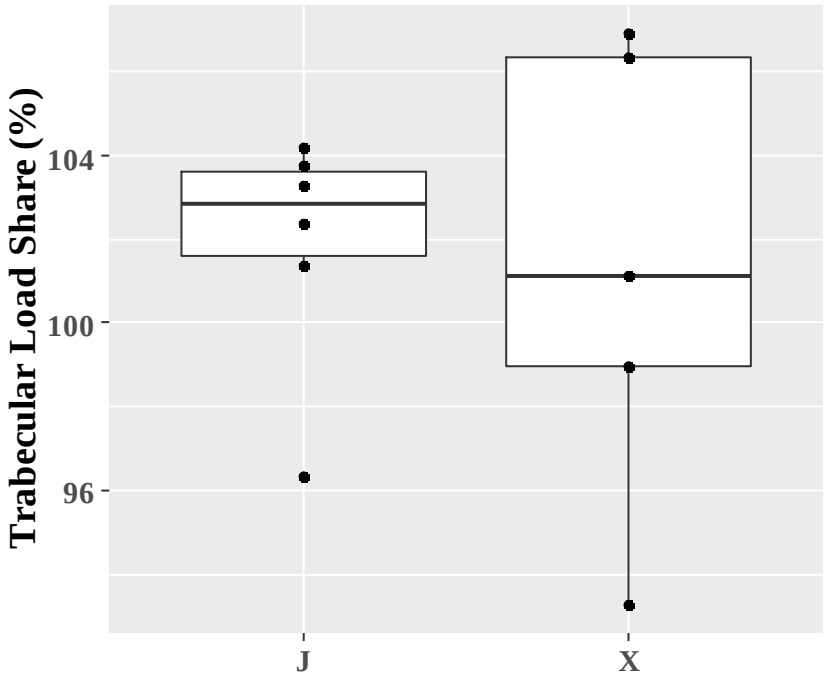

Figure 32. Boxplot of trabecular load sharing in RPC simulation
"J" indicates jumping animals; "X" indicates Scl-Ab-treated animals.
Values of load share over 100% indicate that the cortical shell of the specimen was in axial tension.

Interestingly, the trabecular load share for many of the RPC simulations was greater than 100%. This means that the cortical shells of those specimens were actually

in tension rather than compression. In five VJE samples the cortical shell carried tension, while only 3 SCL cortical shells were in tension. All VJE trabecular load shares were within 5% of 100%, indicating that the cortical shell had a relatively small effect on the load distribution. SCL trabecular load share deviated further from 100%, with the greatest deviation being 107% trabecular load.

Next, we conducted a number of correlations to see how closely our simulations followed the results of our physical RPC testing. Correlations in this section are presented by model type with VJE and SCL animals pooled together. Correlation plots with simulations further separated by group can be found in Appendix B. Figure 33 shows correlations between results derived from physical RPC testing and from FEM-simulated RPC testing.

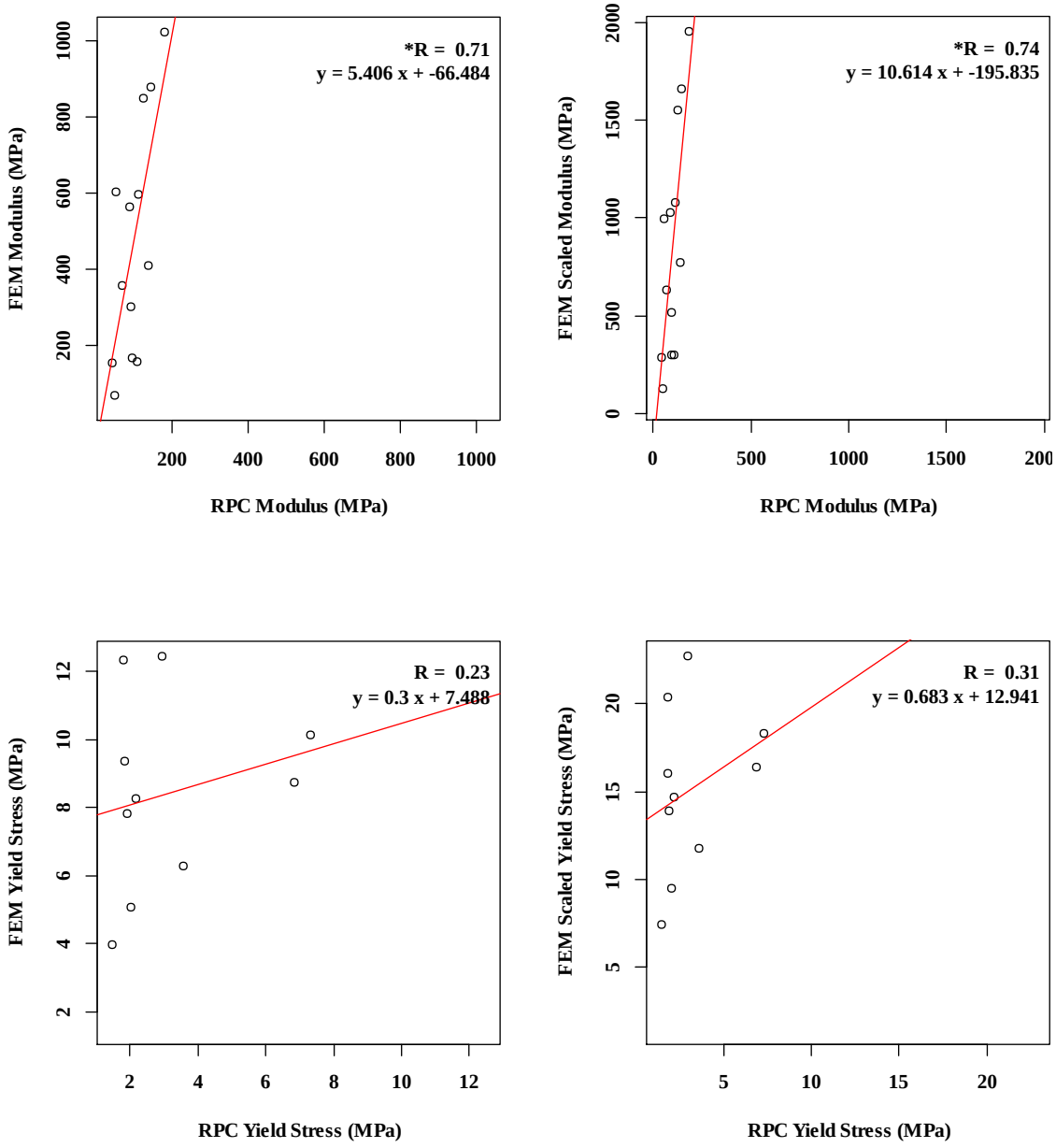

Figure 33. Correlation of RPC and FEM-simulated RPC modulus and yield stress.
"FEM Scaled" measurements in the right two panels were calculated using specimen-specific tissue elastic modulus scaled by μCT TMD.
*correlation is significant, $\alpha = 0.05$.

Modulus correlations between RPC simulations and physical RPC testing were significant, while yield stress correlations were not. R values were reflective of fairly

strong modulus relationships and weak relationships in yield stress. Assigning each specimen a tissue modulus determined by uCT-derived tissue mineral density (TMD) produced marginal improvements in correlation R value. The magnitudes of modulus found by RPC FEM simulation and physical RPC testing were strikingly different. FEM modulus was on average 4-5 times the modulus found from physical testing. After scaling by TMD, FEM values were 8-9 times higher on average compared to physical RPC modulus.

Correlations between the full trabecular compression model configuration and RPC mechanical testing is shown below in Figure 34.

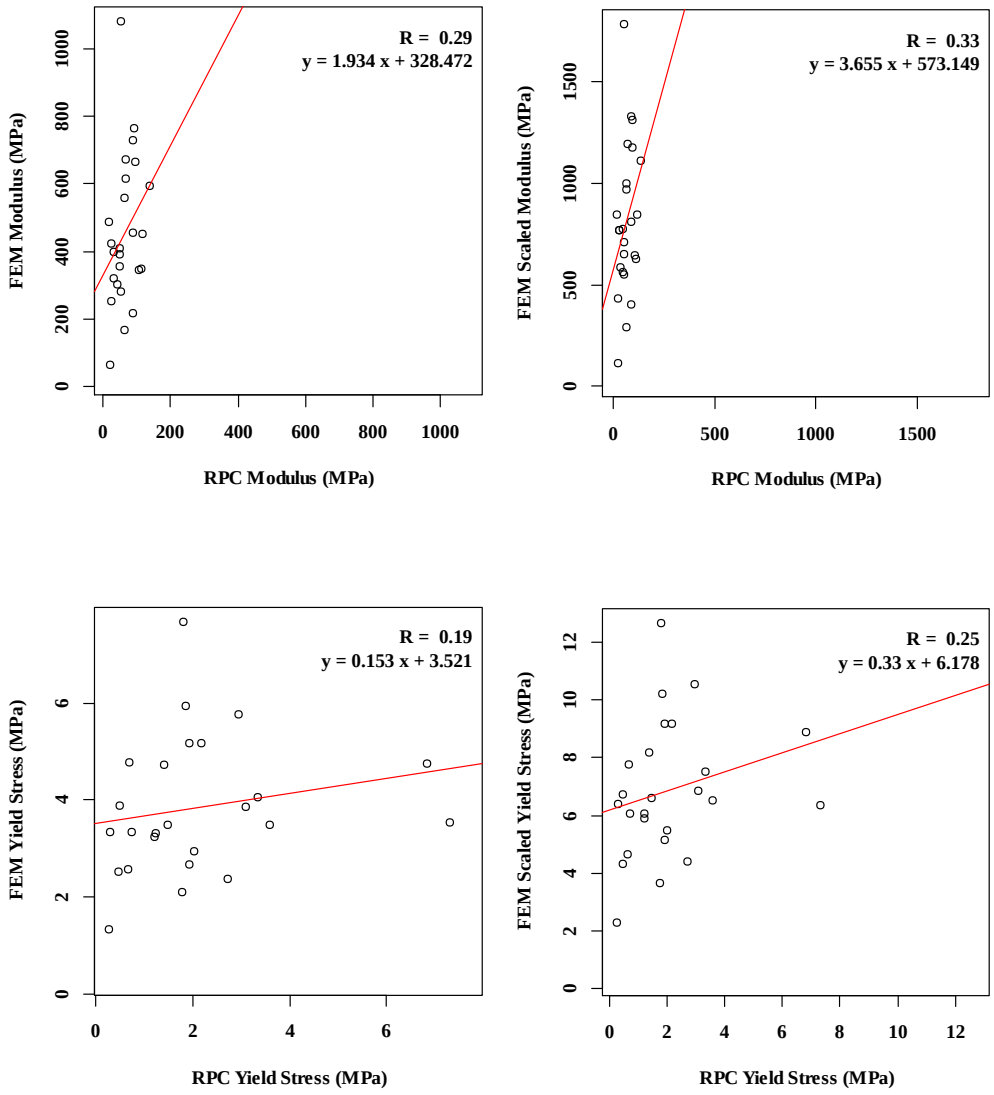

Figure 34. Correlation of results of physical RPC and full trabecular compression FEM simulation for modulus and yield stress
"FEM Scaled" measurements in the right two panels were calculated using specimen-specific tissue elastic modulus scaled by μCT TMD.
No correlations were significant, $\alpha = 0.05$.

Correlations between simulations of full trabecular compression and physical RPC were not significant, and R values were reflective of a weak relationship at best.

Assigning each specimen a tissue modulus determined by TMD produced only marginal

improvements in correlation R value. As with RPC simulation, the magnitudes of modulus found by trabecular FEM simulation were much higher than those found by physical testing. FEM trabecular modulus was on average 5-9 times higher than modulus from physical testing. TMD scaling raised these differences to 9-15 times higher.

Next, we tried to visualize the strain distribution of each simulation using contour plotting in Abaqus. However, the models had so many low-strain elements that the high-strain areas were only faintly visible, if at all. Appendix B contains a few examples of these largely useless contour plots.

Instead of using contour plots, we plotted the "failed" (5% highest strain) elements of each specimen projected onto a 2D plane. While this gives less information than a full strain distribution, these 2D plots do give very clear and legible indications of regions of high stress/strain in each simulation. Figure 35 and Figure 36 below show the failed elements for each simulation from what is essentially a birds-eye view of the specimen. The visualization figures only display specimens whose models were included for both model configurations.

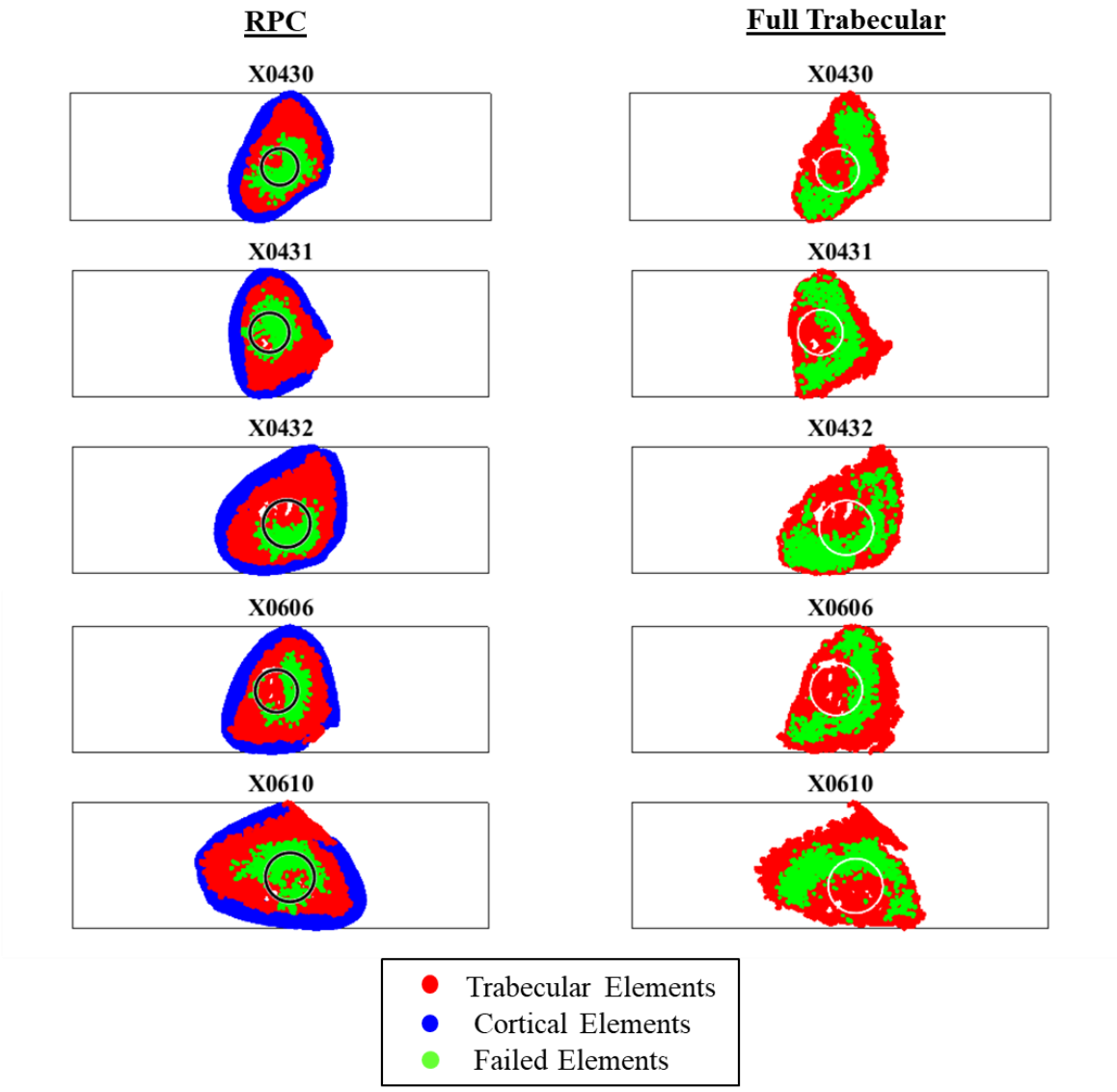

Figure 35. Failure elements in FEM compression of SCL specimens
This figure shows all elements of the 3D model of each specimen projected onto a 2D plane. Green failed elements are the 5% of trabecular elements with the highest effective strain. Calculated platen area is shown by the black circle and reproduced for reference in faint white on the full trabecular specimens. “X” denotes SCL group; “J” denotes VJE.

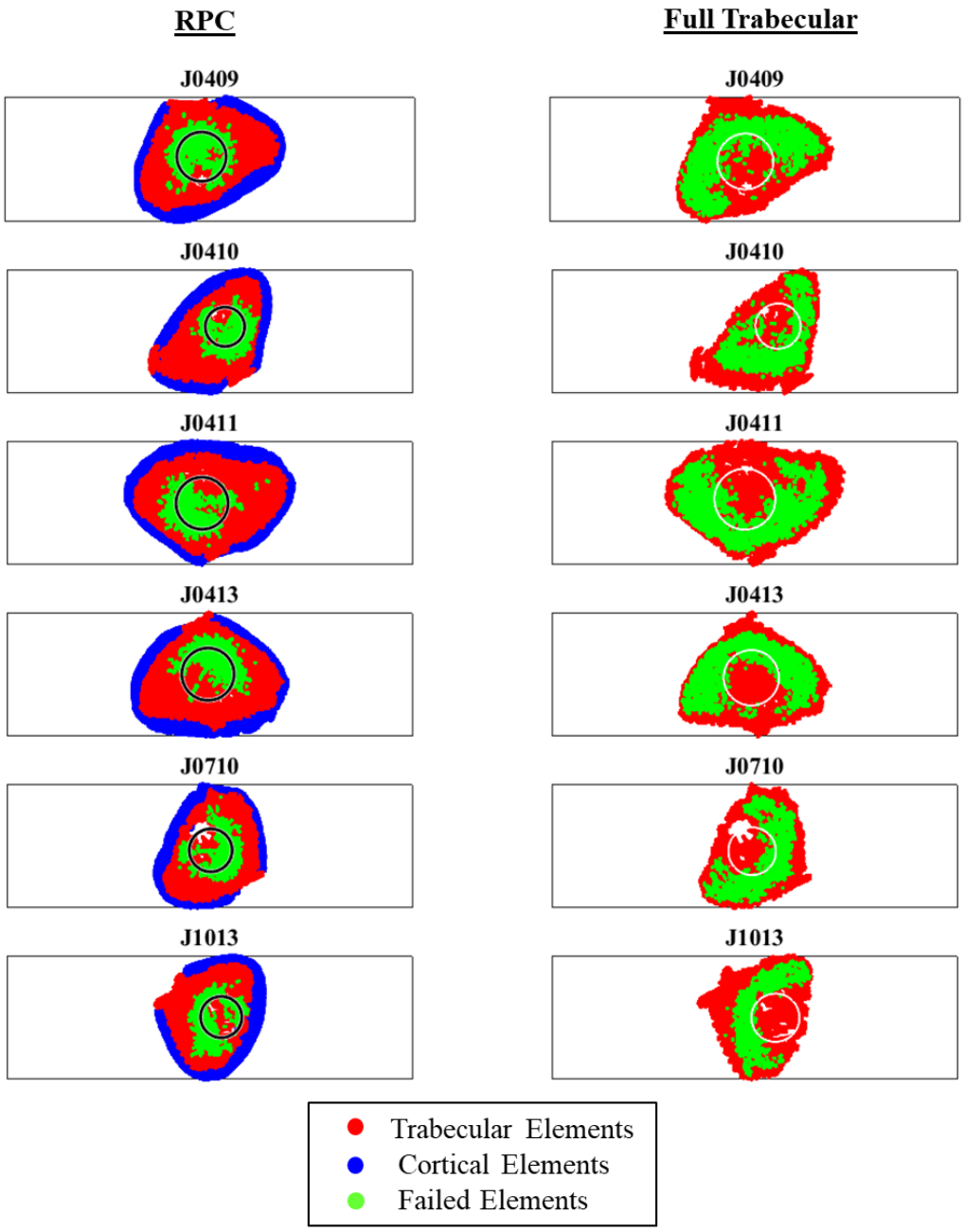

Figure 36. Failure elements in FEM compression of VJE specimens
This figure shows all elements of the 3D model of each specimen projected onto a 2D plane. Green failed elements are the 5% of trabecular elements with highest effective strain. Calculated platen area is shown by the black circle and reproduced for reference in faint white on the full trabecular specimens. “X” denotes SCL group; “J” denotes VJE.

Failed elements for RPC simulations tended to be localized to the volume within and directly around the virtual platen area. The failed elements often were concentrated away from the flat, posterior edge of the specimen. The trabeculae tended to be visually sparser closer to the proximal side of the specimens. VJE and SCL specimens did not seem to have discernible differences in distribution of failed elements.

The failed elements in full trabecular simulations were concentrated away from the virtual platen area (which is reproduced just for reference on the full trabecular models). The failed elements in the full trabecular simulations tended to form a rough arc around the virtual platen area. These arcs seemed to avoid the central, proximal area of the trabecular specimens. Just as with the RPC simulation, this avoided area was where trabeculae were visually sparsest. VJE and SCL trabecular specimens did not seem to have discernible differences in distribution of failed elements.

Next, we plotted similar 2D projection plots from a side view to assess how failed elements were distributed through the height of the specimens. These figures are Figure 37 and Figure 38.

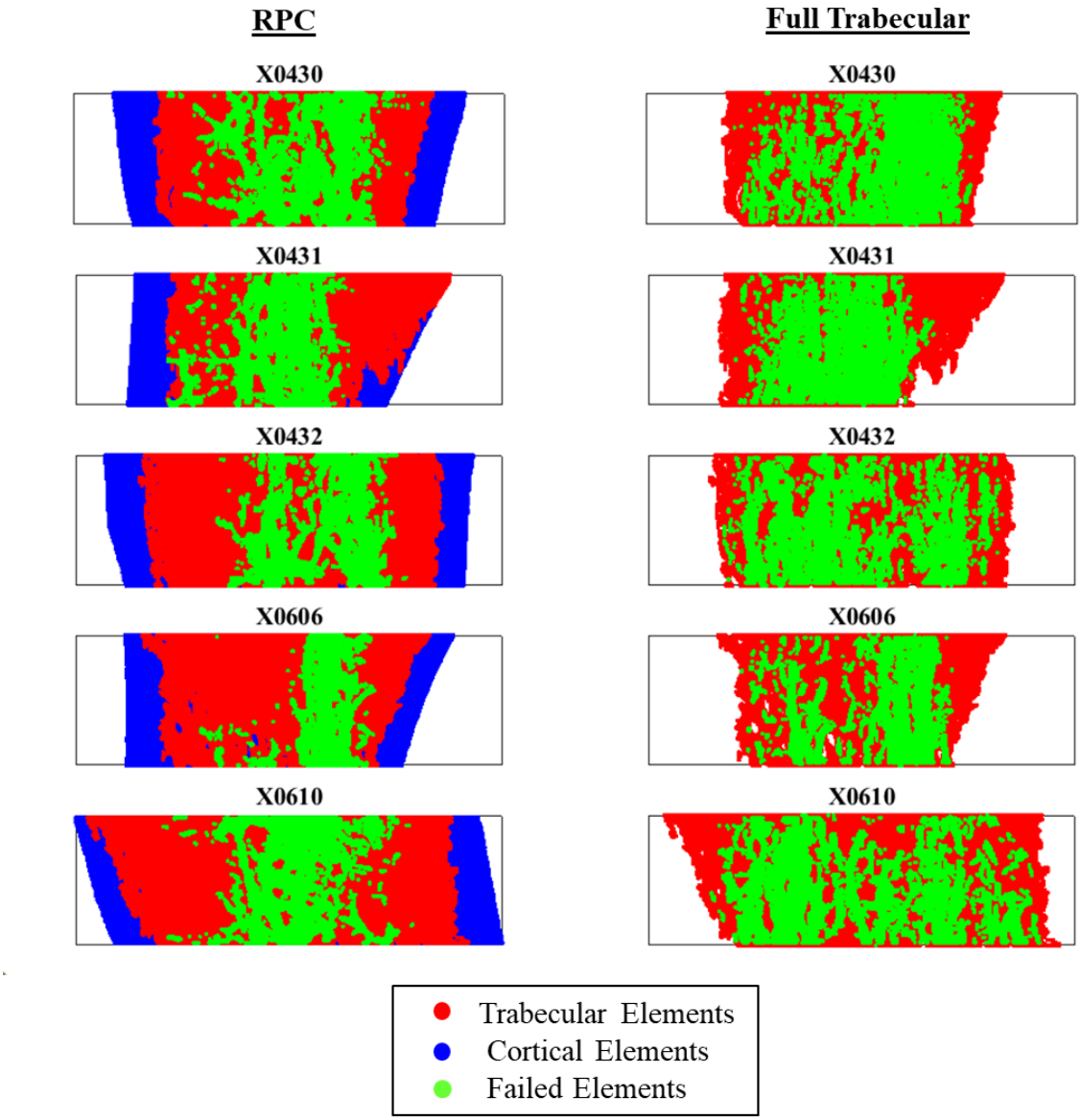

Figure 37. Failure elements in FEM compression of SCL specimens
This figure shows all elements of the 3D model of each specimen projected 2D plane that is perpendicular to the face of the specimen. Green failed elements are the 5% of trabecular elements with highest effective strain. Calculated platen area is shown by the black circle and reproduced for reference in faint white on the full trabecular specimens. "X" denotes SCL group; "J" denotes VJE.

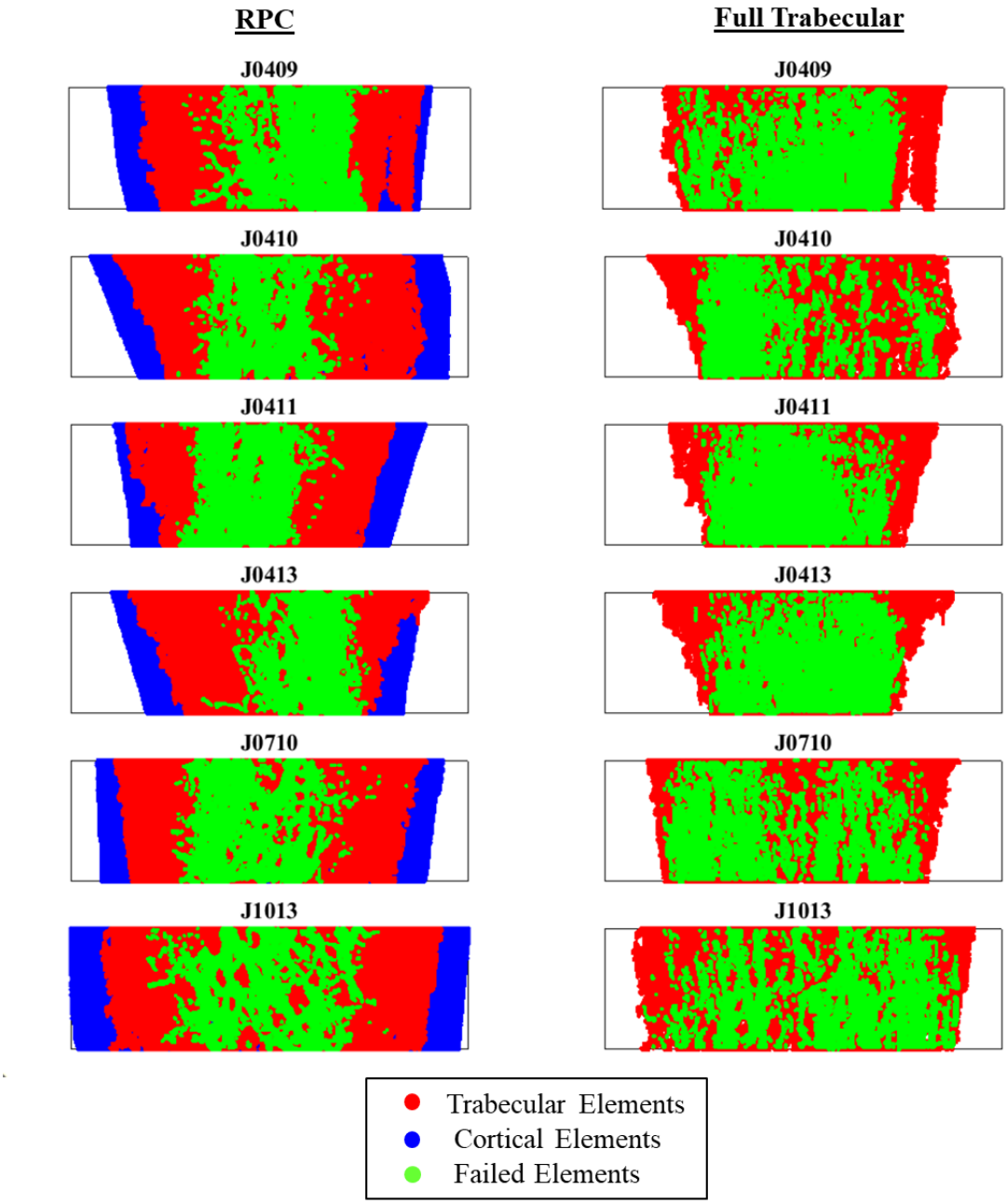

Figure 38. Failure elements in FEM compression of VJE specimens
This figure shows all elements of the 3D model of each specimen projected 2D plane that is perpendicular to the face of the specimen. Green failed elements are the 5% of trabecular elements with highest effective strain. Calculated platen area is shown by the black circle and reproduced for reference in faint white on the full trabecular specimens. "X" denotes SCL group; "J" denotes VJE.

Failed elements were distributed fairly uniformly throughout the height of each specimen, regardless of treatment group or simulation type.

Finally, we performed a correlation between results from trabecular and RPC simulations in an attempt to add mathematical insight into whether our two model configurations produce similar or distinct outcomes. These correlations are below in Figure 39.

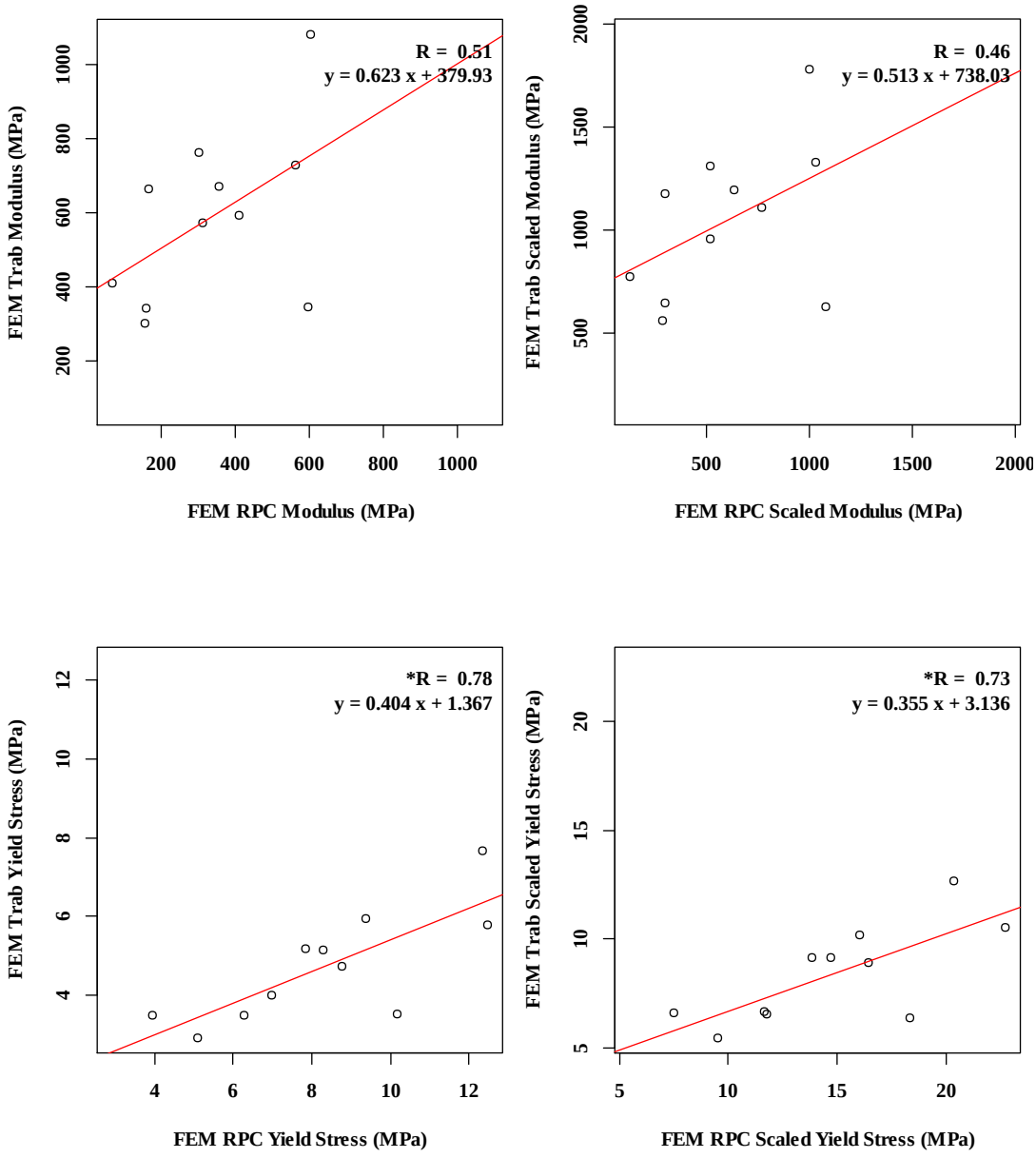

Figure 39. Correlations of FEM-simulated RPC and FEM simulation of full trabecular compression

"FEM Scaled" measurements in the right two panels were calculated using specimen-specific tissue elastic modulus scaled by μCT TMD.

No correlations were significant, $\alpha = 0.05$.

Correlations of the elastic modulus between simulation configuration (RPC and full trabecular compression) were not significant. Yield stress was significantly correlated between the two model types. R values for modulus and scaled modulus were reflective of a modest relationship (n.s.). Yield stress R values indicated a reasonably strong relationship between the two simulation types. Assigning each specimen a tissue modulus determined by TMD marginally lowered R values.

4.6.2.1. FEM Mechanical Property Summary

There were no differences between SCL and VJE FEM outcomes regardless of model configuration. Using tissue mineral density from μCT to determine specimen-specific tissue moduli did not change these results. Calculations of load sharing in RPC simulations found that the cortical shell carried a small amount of tension in most simulations.

We conducted a number of correlations to compare physical and virtual testing. RPC simulated elastic modulus was fairly strongly correlated to RPC physical elastic modulus. Otherwise, no correlations between FEM simulation and RPC physical testing were statistically significant. Assigning each specimen a tissue modulus determined by TMD produced marginal gains in correlation strength.

The highest-strain regions of each simulation type had minimal overlap. Highest-strain regions for RPC testing tended to be concentrated near or within the boundaries of the virtual platen used to compress these models. Full trabecular compression simulations tended to have highest-strain regions that wrapped around the virtual platen area, but did not extensively intersect with the virtual platen area. Yield stress from full

trabecular simulations and RPC simulations were significantly correlated to one another, but elastic modulus was not correlated between the two model configurations.

5. DISCUSSION AND CONCLUSIONS

5.1. Voluntary Jump Training Elevates Loading and Builds Bone through Unloading.

Our measurements of GRFs and bone outcomes in our jump-trained animals confirms that the mechanical loading imposed by our exercise protocol is osteogenic. We found that jumping GRFs were on average 1.8 times higher than body weight of the rat, and we found increases in bone formation rate and decreases in a measure of bone resorption (%OcS/BS) in the tibia and humerus of our animals after 28 days of training. This anabolic bone response led to improved bone outcomes at the femur, tibia, and humerus in jump-trained animals compared to unexercised controls. Tibia and humerus cancellous BV/TV assessed by histomorphometry was elevated by jumping, and pQCT-determined metaphyseal cortical vBMD at the femur and humerus was higher in jumping animals compared to unexercised controls.

We did not see statistically significant anabolic effects of jump training at the end of the 28-day pre-treatment period in our other measures, which were assessed with ANOVA or an equivalent rather than the higher-powered t-test of the above measures. However, for 13 of the 15 measures presented in the Results section, VJE means were non-significantly higher than CON means at the end of jump training (d28). In addition, jumping did significantly elevate cancellous bone outcomes compared to unloading controls at the end of unloading. At the end of unloading, μCT analyses revealed higher BV/TV and trabecular thickness in jump-trained animals compared to hindlimb-unloading controls. Elastic modulus, yield stress, and ultimate stress in the cancellous

bone of the femur were also elevated in VJE rats compared to unloading controls at the end of unloading. Based on the anabolic bone response we found at the end of the training period and the increased GRFs we found during jumping, the results presented show that our jumping protocol is an effective model for physiological, anabolic resistance exercise. In addition, jumping's effectiveness through four weeks of unloading suggests that resistance exercise could also be a viable preventive countermeasure for microgravity-induced bone loss.

Our jumping protocol is most similar to a protocol used by a group from Japan, but that group tends to use their jump training paradigm in growing animals[15,17,70]. It is well-established that the bones of young, growing animals respond more strongly to mechanical stimuli compared to skeletally mature animals because of the naturally higher levels of bone turnover in growing bones[115–117]. In addition, the Japanese group focuses mainly on pQCT and extrinsic properties of the tibia midshaft[15,70,118]. Our current study used skeletally mature rats and reported mainly metaphyseal outcomes from the femur (and some from the tibia and humerus).

Our study's focus on metaphyseal and cancellous bone is not typical for studies of resistance exercise models. Most previous studies have focused on the cortical midshaft. However, our lab did investigate cancellous bone outcomes in a previous model of resistance exercise[119]. Six-month-old, male Sprague Dawley rats—the same animal specifications as used in our current study—jumped up and depressed an illuminated bar 12 inches above their cage floor. Rats trained while wearing a 30 g vest (~8% of body weight). At the proximal tibia metaphysis, trained animals gained 30%

BV/TV and trabecular thickness and had 50% decreased osteoclast surface as measured by cancellous histomorphometry[119]. In those same measures at the proximal tibia, our VJE animals gained 30% BV/TV and lost 35% osteoclast surface, but we did not find changes in trabecular thickness. Our voluntary jumping protocol produces similar anabolic changes in cancellous bone as these previously published results for resistance exercise.

We believe that our unique positive reinforcement conditioning is a step forward compared to previous resistance exercise models, which have overwhelmingly relied on negative shock reinforcement. Positive reinforcement eliminates the need for costly electrical equipment that can be difficult to use and maintain, and the lack of a shock grid on our cage floor allowed us to employ a very simple force plate setup to measure ground reaction forces. The previous studies discussed have not quantified ground reaction forces, likely because it would be quite complicated to install the necessary shock grid and a force plate in the cage floor. Finally, positive reinforcement by sugar treat likely reduces stress in our animals compared to negative reinforcement by shock avoidance. We did not formally measure stress outcomes, but future work should quantify stress behaviors or serum stress markers in our VJE animals build a stronger case for the advantages of our procedure. Nonetheless, we believe we have created a physiologically relevant resistance exercise model that has distinct advantages compared to existing rodent models.

5.2. Strain and Strain Rate from Jumping Could Drive Forelimb-Hindlimb Differences.

Improvements in histomorphometry-measured BV/TV, %OcS/BS, %MS/BS, and MAR were more drastic at the proximal humerus than at the proximal tibia metaphysis in VJE animals. These findings suggest a stronger anabolic response at the humerus. Peak GRFs in the forelimbs and hindlimbs were almost identical, but GRFs do not measure bone strain, which is what triggers bone remodeling. GRFs of the same magnitude could produce different strains in the humerus compared to the tibia. In fact, one study found that quietly standing rats support 80% of their body weight on their hindlimbs[120]. Since it seems rats are accustomed to supporting larger loads on their hindlimbs, it is likely that the bones of their hindlimbs would adapt to carry larger loads than the bones of their forelimbs. Thus, the same force applied to the hindlimbs would translate to lower strains than would be produced by the same load in the forelimbs. The relatively higher strain in the forelimbs would trigger more robust osteogenic remodeling in the humerus compared to the tibia. The spatial distribution of strains could also be different, giving rise to focally higher strains in the humerus even for the same overall GRF magnitude.

Another explanation for the difference in osteogenic response is the different loading rates between forelimb landing and hindlimb jumping. We found a much higher rate of force development in the forelimbs (although the non-parametric comparison was too low-powered to assure statistical significance). The higher loading rate should lead to a higher strain rate in the forelimbs than the hindlimbs. In-vivo limb loading models

have shown that high strain rates better enhance bone formation rate[121]. A higher strain rate could explain the increased osteogenic response in the humerus. If this explanation is correct, exercise that specifically targets bone should focus on increasing bone strain rates as well as bone strain.

5.3. Scl-Ab Outperforms Jump Training in Improving Cancellous Architecture and Strength.

Four weeks of treatment with Scl-Ab produced dramatic improvements in cancellous bone in our rats. These enhancements persisted through 4 weeks of unloading and through a subsequent 8-week recovery period. In measures from μCT at the distal femur, Scl-Ab treatment produced more statistically significant enhancements and greater percent differences than exercise did. In addition, SCL rats exhibited elevated TMD at d112 and elevated Tb.Th at all timepoints when directly compared to those values in VJE animals. Thus, μCT suggests that Scl-Ab treatment was more anabolic than jump training in the cancellous bone.

Results from physical RPC testing support this notion. Scl-Ab treatment caused potent gains in trabecular bone strength. Scl-Ab enhanced every cancellous mechanical property above ambulatory control levels at every timepoint, even immediately after 28 days of hindlimb unloading. SCL means were routinely double those of CON animals and double those of VJE animals, and in some cases SCL group means were up to three times higher than those of CON rats. On the other hand, jump training produced no enhancements above control levels prior to unloading. In addition, every RPC measure taken immediately after treatment (d28) was elevated in SCL rats when directly

compared to VJE. SCL was sometimes higher than VJE in RPC measures at d56 and d112 as well.

Normalizing mechanical properties by BV/TV did close the gap somewhat between SCL and all other groups, indicating that SCL gains in cancellous properties are due in part to increased cancellous bone mass. This result is unsurprising, given our findings of 50%-100% increases in BV/TV from Scl-Ab treatment and past studies that have found as much as threefold increases in BV/TV[24]. The fact that normalization by BV/TV did not fully eliminate the relative advantages observed in rats treated with Scl-Ab could suggest that Scl-Ab also improves cancellous bone material properties, in addition to bone mass. However, a more cautious explanation is that the BV/TV of the full specimen, which we used to normalize RPC properties, is not fully reflective of the BV/TV of the central region tested during RPC. The central region tends to be sparser than the cancellous structure as a whole, and we have observed over the years of RPC testing that this same central region seems to be most sensitive to bone loss in unloading control animals.

Even if we are not certain that Scl-Ab enhanced cancellous bone quality, the treatment was still incredibly effective at building bone mass and strength in the cancellous compartment, much more so than exercise. Given our findings and the positive findings of previous studies testing Scl-Ab during disuse [24,84,86,87], Scl-Ab seems to be a promising pharmaceutical countermeasure for spaceflight use.

Previous animal studies have investigated Scl-Ab as a countermeasure for spaceflight-induced bone loss. Most of these studies have given Scl-Ab concurrently

with disuse, while our study investigated Scl-Ab as a pretreatment to disuse. Nevertheless, the trends in our pretreatment study and previous concurrent treatment studies are much the same. Zhang et al. administered Scl-Ab to 4 month-old female Sprague Dawley rats during hindlimb unloading. Scl-Ab treatment doubled cancellous BV/TV compared to untreated animals[82]. Spatz et al. administered Scl-Ab to mice during hindlimb unloading and found gains in trabecular bone mass and cortical bone strength compared to mice that were untreated during unloading[24]. This same group also investigated the effects of Scl-Ab in a partial weightbearing mouse model, which is analogous to loading astronauts would experience on the Moon or Mars. They found that Scl-Ab treatment during partial weight bearing completely prevented bone deterioration in their mice, and even enhanced bone outcomes above fully weight-bearing control levels. This trend held true for whole-body BMD, mechanical strength at the femur midshaft, and cancellous BV/TV. The effect on cancellous bone was especially pronounced, with Scl-Ab-treated animals having 2-3 times the BV/TV of all other groups[84].

Our Scl-Ab pretreatment approach was effective through unloading. The gains it produced were similar to those of previous concurrent studies. Like the concurrent studies, we found increases in mechanical strength at the femur midshaft and large gains in measures of cancellous architecture. Cancellous BV/TV was as much as doubled in Scl-Ab animals compared to untreated controls, which is comparable to the 2-3x increases in BV/TV found in previous studies[82,84]. Unlike the previous studies, we supplemented our assessment of cancellous bone by measuring cancellous mechanical

properties at the femur metaphysis. We found massive gains in Scl-Ab animals in cancellous mechanical outcomes as well (5x yield stress, 5x modulus, and 6x ultimate stress compared to unloading controls). The results of our current study suggest that Scl-Ab pretreatment before a period of disuse is comparably effective to administering Scl-Ab during the disuse period. In addition, the current study demonstrates for the first time that the substantial gains in cancellous architecture typically produced by Scl-Ab treatment translate into substantial gains in cancellous strength.

In addition to previous studies that used concurrent treatments, one prior pretreatment study has been conducted using Scl-Ab. Investigators in this study injected a cohort of young, growing mice with a single large dose of Scl-Ab, and then sent the mice to space aboard space shuttle mission STS-135. Comparisons of magnitudes of treatment impacts are not terribly useful between our study and the STS-135 study. Our study was done in adult rats, while the STS-135 study was done in growing mice. However, the trends we observed are very similar to the findings of the STS-135 study. In the STS-135 study, Scl-Ab treatment eliminated losses in whole-body BMD, losses in cancellous volume and architecture at the tibia, and losses in bone strength at the femur midshaft[25]. Additionally, finite-element modeling found improved strength in a non-weight-bearing vertebrae of the STS-135 animals[86], which is a mixed bone site, meaning that cancellous strength likely contributed at least mildly to this outcome.

Our study corroborates this earlier study's findings that pretreatment with Scl-Ab improves midshaft strength and cancellous architecture and strength, and we do so in a skeletally mature rat model that is more analogous to the adult astronaut population than

the growing mice used in the STS-135 study. In addition, we administered smaller, weekly doses of Scl-Ab over four weeks before unloading, instead of one large dose immediately before spaceflight. Our weekly doses resulted in the same total dose as the STS-135 study, but our dosing scheme is more analogous to clinical Scl-Ab dosing[81]. Taken together, our ground-based analog study and the STS-135 study during actual spaceflight clearly demonstrate that Scl-Ab is an effective preventive countermeasure to subsequent disuse.

5.4. Scl-Ab improves midshaft cortical structure; jump training improves midshaft cortical quality.

Interestingly, the improvements we found in mechanical properties measured by three-point bending were not congruent between extrinsic and intrinsic properties. SCL animals showed improvements in stiffness, maximum force, and yield force at certain points in the study, which are whole-bone extrinsic properties. However, SCL animals exhibited no improvements in the intrinsic material properties of modulus, yield stress, and ultimate stress, so Scl-Ab's effect was clearly on the size and shape of the bone and its cross-section. On the contrary, VJE animals showed elevated material properties of modulus and ultimate stress at the end of pretreatment and at the end of recovery, but no improvements in extrinsic properties at any point in the study. So, it appears that Scl-Ab treatment improved the structural properties of the femoral midshaft, but not the material properties. The opposite appears to be true for jump training, which exerted no effect on the structural properties of the femoral midshaft, but did improve the material properties of the bone.

Previous mechanical testing in rodent models for disuse has found that Scl-Ab produced elevations in structural properties at the midshaft in rats[82,122] and mice[24,84], which agrees with our results. However, none of these studies reported intrinsic properties (which could be derived from their three-point bending results for extrinsic properties).

One study that did report intrinsic properties in nine-week old Scl-Ab-treated rats found that, compared to untreated controls, treated rats had greatly elevated extrinsic properties at the femoral shaft—32% greater stiffness and 34% greater maximum force. At the same time, Scl-Ab had little to no effect on material-level properties. Elastic modulus was increased by 1.7% in Scl-Ab animals, and the researchers found no effect of treatment on ultimate stress[123]. Our study's findings were much the same. We found 10-30% gains in extrinsic properties of stiffness, maximum force, and yield force in Scl-Ab treated rats compared to reference groups, but we found no significant differences in intrinsic properties of elastic modulus, ultimate stress, and yield stress. Our findings reinforce that Scl-Ab works in cortical bone by increasing bone mass, without substantially altering (positively or negatively) the quality of the bone produced.

On the other hand, we did not find any enhancements in extrinsic mechanical properties in jumping animals. It is possible that any positive effects of jump training on extrinsic bone properties were offset by the lower bodyweights of the VJE animals. VJE animals had lower body weight than other groups throughout the study, and smaller body weights should lead to lower bone mass compared to larger animals, with all else being equal. Extrinsic mechanical properties are highly dependent on the size of the

material tested, so lower bone mass in smaller animals should lead to correspondingly lower extrinsic properties. The lower body weights of the VJE animals could explain why we did not see elevations in extrinsic three-point bend properties of the cortical midshaft, while other groups have found elevations in extrinsic properties from jumping.

The Japanese group that uses a very similar jumping protocol to ours has found elevations in cortical bone structural properties (breaking force), but not in intrinsic properties (ultimate stress)[15,70,118]. These findings are opposite of the findings of our current study, which found enhanced intrinsic properties but no change in extrinsic properties of cortical bone. The Japanese group studied a range of animal age, sex, and strain. They studied growing (12 wks) and old (44 wks) male Wistar rats[15], adult female Wistar rats (9 month)[118], and growing female Fischer rats (5 wks)[70]. Our animals were 6-month-old male Sprague-Dawley rats, so differences in our findings and the Japanese group's findings could be at least partially caused by the differences in animals between our study and their studies.

On the other hand, our lab previously did find elevations in intrinsic mechanical properties of the femur midshaft in a model for resistance exercise[124]. This previous study was done in 6 month old, male Sprague Dawley rats, which is the same age, sex, and strain used in our current study. In the previous study, rats jumped up and depressed an illuminated bar 12 inches above their cage floor while wearing a 30 g training vest (~8% of body weight). Animals that trained under this paradigm experienced gains in intrinsic mechanical properties at the femur midshaft. Femurs of exercised animals had 23% higher ultimate stress compared to untrained controls, but no enhancements in

elastic modulus[124]. In our current study, jump-trained animals gained 5-15% ultimate stress and 20-60% elastic modulus at the femur midshaft compared to untrained reference groups.

It seems there is not strong consensus in the literature on whether models of resistance exercise enhance cortical bone intrinsic properties (cortical bone quality). It might be worthwhile then to further assess bone quality in our VJE animals. Raman spectroscopy would allow us to measure mineral/matrix ratio and collagen crosslinking. We would need to find a collaborator skilled in Raman spectroscopy, but undertaking this test would give us further insight into bone quality changes caused by our jumping exercise protocol. Those outcomes could help us or future researchers to resolve discrepancies in bone quality effects between different rodent models of simulated resistance exercise.

5.5. No Evidence of Long-Term Adverse Effects of Scl-Ab

A clinical study found severe bone loss after cessation of all forms of treatment in osteoporosis patients who had previously taken Scl-Ab to elevate their bone mass. In 12 months, the patients lost 80-90% of the BMD gains they had made over one year of Scl-Ab treatment and two years of subsequent treatment with an anitresorptive (denosumab)[88]. Unlike in the human studies, we found no evidence of “rebound” bone loss in our animals after we ceased treatment. In fact, SCL animals had lasting enhancements in almost all measures that we assessed. In many cases, the benefits of only four weeks of Scl-Ab persisted through four weeks of unloading and through a further eight weeks of recovery.

It is possible that the rebound bone loss seen in the clinical study was due to denosumab administration, and that is why we found no losses in our Scl-Ab-only animals. We believe, though, that the difference between our long-term results and the results of the clinical study could be due to the initial bone health of the study subjects. Our rats were healthy before beginning Scl-Ab treatment, while the clinical study was done in osteoporotic postmenopausal women who had T-scores of -2.5 to -3.5 at the total hip or femoral neck[88]. In both studies, Scl-Ab elevated bone mass in the subjects. When the osteoporotic women ceased all forms of treatment, their Scl-Ab-enhanced bones reverted quickly towards their initial, fragile state. When our rats ceased Scl-Ab treatment, their bones were initially exposed to 28 days of disuse, but then returned to a state of normal and healthy weight bearing. We believe that Scl-Ab was still active over a majority of our unloading period, and our rats' return to a healthy bone state after unloading prevented the extreme rebound losses seen in the osteoporotic women.

We did not measure indices of bone formation and resorption for all animals in this study, but previous measurements in these same animals found that bone formation rate and serum CTX-1 (a marker of bone resorption) in SCL and HUC animals were virtually identical at the end of unloading[125]. Based on these findings, it seems that the Scl-Ab was no longer protective by the end of unloading. It is possible that Scl-Ab's influence on bone turnover tapered off at the very end of the unloading period, and that a return to weight bearing restored bone remodeling to a balanced state in our animals. Based on this thinking, our rats may have seen a rebound effect similar to the bone loss experienced by the osteoporotic women if we had extended our unloading period. Future

work in animal models should attempt to investigate whether Scl-Ab prompts rebound bone loss if not taken frequently during long-duration simulated microgravity. These findings would be highly relevant in evaluating Scl-Ab's viability for use on exploration spaceflight missions.

5.6. Puzzling FEM Results are Opportunity for Future Work

Results from FEM-simulated compressive testing of cancellous bone were not what we expected. There were no differences between VJE and SCL outcomes, and FEM outcomes were largely not correlated to physical RPC outcomes. Further, FEM modulus was on average 4-9 times higher than elastic modulus found during physical RPC testing. Assigning each specimen an individualized tissue modulus based on its average tissue mineral density did not substantially improve correlations or differences in absolute values. Instead, specimen-specific moduli exacerbated the absolute differences between physical and virtual compression outcomes by a further 70-80%. Finally, calculations of load sharing for the RPC models found that the cortical shell was actually in tension during a simulated compression test. While these results are unexpected and some are disappointing, they still provide useful information about RPC testing and lay the groundwork for many opportunities for future improvements.

VJE and SCL outcomes from FEM simulation were not statistically different. However, SCL consistently outperformed VJE in μCT and physical RPC in the exact same bone region of interest. We excluded a large number of RPC simulations, which likely had a moderating effect on any group differences. In total, 9/15 VJE models were excluded, and 9/14 SCL models were excluded. The majority of these models were

excluded because their trabecular structures were too sparse to support meaningful application of boundary conditions. However, three of the SCL models were excluded because they were especially dense, and the MATLAB input algorithm incorrectly categorized a large portion of their dense trabecular structure as cortical bone.

Because of the many excluded RPC simulations, it is probably best to not overinterpret the lack of differences between SCL and VJE animals for those models. On the other hand, only three full trabecular simulations were excluded, and the full trabecular simulations still found no differences between SCL and VJE. We expect the full trabecular simulations to be less sensitive than RPC due to the regions where boundary conditions are applied in each model. RPC tests the sparser central region of the specimen, while the full trabecular configuration tests the whole cancellous region. In fact, the two model configurations seem to be poorly related. The highest-strain regions of each simulation type had minimal overlap. The highest-strain elements in full trabecular simulations are not located in the sparse central region tested by RPC. This difference is reflected in the lack of significant correlation between elastic modulus from full trabecular simulations and RPC simulations.

The full trabecular models test the whole trabecular bone volume, while RPC models and RPC physical testing test the lowest density portion of the trabecular structure. Even though the full trabecular models might not be reflective of RPC, these models should still be strongly influenced by architectural parameters of the full trabecular region, where we found substantial improvements in Scl-Ab treated animals. Our μCT measurements revealed 27.8% higher trabecular thickness and 29.2% higher

(but n.s.) BV/TV in SCL rats compared to VJE rats. These differences in trabecular architecture should be reflected in our FEM modeling, yet we found no such differences. In fact, VJE animals had 23% higher simulated elastic modulus than SCL animals (n.s.). This result runs counter to all of our other findings, so we should attempt to improve our modeling protocol.

Our first attempt at improvement was altering the way that we defined the tissue modulus for each specimen. For the original set of FEM simulations, we used a standard literature value of 10 GPa for elastic modulus. Assigning every specimen a uniform tissue elastic modulus somewhere between 6.8-20 GPa is common practice in FEM modeling of bone[126], and using 10 GPa is particularlycommon[112,113,127–129]. However, we thought that we could improve the fidelity of our modeling by assigning each specimen a unique modulus based on the specimen's average tissue mineral density. To do this, we used a previously-derived relationship from the literature to determine a tissue modulus for each specimen using the average tissue mineral density (TMD) of the same specimen[103]. We thought that this process might improve the sensitivity of our simulations and reduce the drastic differences between magnitudes of physical and simulated specimen elastic modulus. Unfortunately, this procedure did not improve our results. In fact, the main effect of scaling by tissue mineral density was to make differences in magnitude of physical and simulated specimen modulus about 70-80% greater.

Despite the lack of meaningful improvements, we believe that future iterations of our models should continue to use tissue mineral density to determine tissue modulus

values. This approach should improve model fidelity compared to assigning a standard tissue modulus to all specimens, and it requires virtually no increase in computing costs or human labor. In addition, previous studies have found improvements when using this or a similar method to assign subject-specific tissue modulus[101–103]. In our case, lack of improvement when using this method is not too surprising, given the minimal effects our treatments had on TMD. The modeled VJE and SCL specimens did have significantly different mean TMDs, but the percent difference in their means was only 3.3%. Using TMD to determine tissue modulus might become more important in the future if we use a treatment that produces substantial changes in cancellous TMD.

Since altering the tissue modulus of our models did not improve our results, we should look elsewhere, specifically to the boundary conditions that we applied to our models. Boundary conditions were visually problematic in our RPC models, leading to 15/29 models being excluded from this study. Full trabecular models seemed to fare better, and none of those models were excluded due to boundary conditions. However, it is still possible that uneven application of boundary conditions to the irregular bone structure resulted in incongruencies from our other findings in the same bone volume.

Future iterations of RPC and full trabecular models should consider including a solid body (i.e. a virtual platen) and apply the boundary conditions to that virtual platen instead of applying them directly to bone. A version of this approach to boundary conditions has been successfully applied by Nawathe et al. in models of femoral neck mechanical testing[130,131]. These groups applied boundary conditions to a regularly shaped PMMA layer, which then transferred the loading conditions to the irregular

femoral head. Adapting Nawathe et al.'s methods to suit our models would allow us to apply boundary conditions evenly to a solid platen, which will then evenly transfer our prescribed loading to the bone specimens. This method should remove inaccuracies that may have arisen from our application of boundary conditions directly to bone.

In addition to changing our application of boundary conditions, we should investigate the MATLAB image analysis techniques that we used to create the 3D bone volume. The process of determining what voxels qualify as bone and what voxels are marrow space often causes overestimation of bone volume[126]. This could explain the large discrepancies we see in values of elastic modulus between simulation and physical testing. When he developed the modeling process used in this study, Kohn tested a number of thresholds for bone/marrow segmentation before settling on our current method[104]. We should revisit these parameters now that we have a larger sample size than the *n* of two in Kohn's work. It is possible that the parameters that Kohn chose were well-suited for his samples, but are not well suited for the samples in this or future studies. Another option is to attempt to use pre-segmented images directly from the μCT. To determine trabecular number, the μCT software does its own segmentation. These pre-segmented images tend to overestimate bone volume, but they are routinely used in FEM of bone[126]. If we have a way to access these image files, we should build our 3D models with them and evaluate the outcome.

In addition, we should examine the MATLAB image algorithm that separates trabecular from cortical bone elements in our models. In this study, we visually inspected the results of this algorithm, and we removed three SCL models that were

clearly differentiated improperly. In the future, we should do a more thorough visual examination of our cortical-cancellous differentiation to ensure that the denser specimens are not being slightly but systematically underpredicted. If the denser specimens tend to have slightly more trabecular elements sorted as cortical elements, it could lead to systematically less bone volume in trabecular models of high-density specimens. If we determine that the cortical-cancellous sorting process is problematic, we could develop a more-geometric method of generating trabecular-only specimens. We could manually or automatically trace the cancellous area on the top and bottom faces of the model and extrapolate those shapes through each of the models' 100 layers.

Finally, we should examine our yield criterion. In this study, we assumed that our models yielded when 5% of their elements reached 0.7% strain. This method is based on the work of Pistoia et al.[113]. This group found that they could predict compressive fracture loads of whole bone specimens of human distal radii (cortical and cancellous bone) using FEM. Their models accurately predicted fracture loads when 2% of the elements in their models reached 0.7% strain[113]. Thus, Pistoia et al. used a linear FEM model to predict fracture, a non-linear phenomenon. This method has since been commonly used to predict fracture strength at the distal radius[126–128,132].

One important difference between our models and Pistoia et al.'s models are that the latter models loaded both the cortical shell and the cancellous core of the distal radius. In addition, other studies that have used their failure prediction method have also tested both cortical and cancellous bone[126–128,132]. These researchers isolate a transverse slice of bone and compress the entire cross section. The stress distributions from these

linear-elastic simulations show that the cortical elements carry very high stresses, while the trabecular elements largely support low stresses[126,128,132].

On the other hand, our RPC testing loads only cancellous bone. As a result, our physical RPC tests are highly non-linear, even for a test of bone. Because of this, we thought it was inappropriate to attempt to predict non-linear fracture with our linear RPC simulation. Instead, we attempted to adapt Pistoia et al.'s method to predict yield, which is nominally a linear phenomenon. We expected much higher strains for a fully cancellous specimen than for Pistoia et al.'s compression of mixed bone. So, we chose 5% instead of Pistoia et al.'s 2% threshold of elements beyond 0.7% strain.

Pistoia et al. arrived at their 2% cutoff after they systematically varied their cutoffs to find which percentage provided the best prediction of fracture force. Future work should replicate this in our models. We should systematically vary the cutoff for yield in the RPC simulation. Then, we should use the correlations between RPC simulation and RPC physical testing to determine the most appropriate cutoff percentage. If we cannot achieve acceptable accuracy with any cutoff percentage, we should abandon this method. It could very well be impossible to use linear-elastic FEM to predict yield in these highly irregular cancellous specimens.

A final unexpected result of our FEM modeling was the discovery that the cortical shell often carries tension in RPC simulations. In 8 of the 11 models, trabecular load share was greater than 100%, indicating that the cortical shell carried axial tension. This runs counter to our traditional assumptions on load sharing in RPC testing. We assumed that the compressive loads placed on the central trabecular region of the RPC

specimens would gradually transfer outward through the trabeculae, which would eventually apply some level of axial compression to the cortical shell. Instead, our results suggest that the main influence of the cortical shell is constraining the trabecular structure as it attempts to expand away from the platens. As materials are compressed, they attempt to expand perpendicular to the direction of compression. For the trabecular region, this results in a radial expansion of the trabecular structure away from the platens. As the trabecular structure expands, it presses against the cortical shell. This compression from the cortical shell again causes expansion perpendicular to the direction of compression, which is now the axial direction. The trabecular structure's attempted axial expansion puts the cortical shell in axial tension.

Our purpose in measuring load sharing was to determine the extent to which the cortical shell influences results determined by RPC testing. Since the purpose of RPC is to determine cancellous bone material properties independent of the cortical shell, the nature and magnitude of cortical shell constraint and load sharing is important to understand. Despite our unexpected findings of tension in the cortical shell, the magnitudes of the tension (or compression) in the cortical shell were quite low. Trabecular load share in our 11 models ranged from 93% to 107%, so our FEM modeling does indeed indicate that the RPC test is predominately a test of cancellous bone.

5.7. RPC Tests the Most Vulnerable Region of the Trabecular Structure

RPC mechanical testing likely underestimates trabecular mechanical properties, especially for animals with less dense trabecular structures. Previous observations during

RPC testing and our FEM modeling both suggest that the central portion of the cancellous compartment tends to be less dense than the areas closer to the cortical shell. This central region is the most responsive to bone loss due to unloading or other physiological factors, and this is the region that RPC testing focuses on. The RPC test is thus especially sensitive to losses in cancellous bone mass, but its results do not reflect properties of the entire trabecular volume.

We do not believe that the RPC test is invalid even if it may not be fully reflective of the entire trabecular structure. RPC still provides a simple method to directly assess cancellous strength. However, we do believe that it is important to be cautious when interpreting RPC results. We should expect large percent differences in RPC testing, and we should not rely on RPC alone to assess cancellous bone. Instead, we should use RPC as a complementary test to strength-surrogate measurements like μCT and histomorphometry, and we should always keep in mind that RPC tests the part of the cancellous structure most vulnerable to bone loss.

5.8. Limitations

While we believe our study has unique strengths and meaningfully contributes to existing knowledge, it is not without limitations. Some of those limitations have been discussed above as they arose. The remaining noteworthy limitations are discussed below.

5.8.1. Male Rat Model Translatability

A limitation of all animal models are inherent differences between the animals used and humans. Rat cortical remodeling and architecture is different from that of

humans. Human cortical bone is remodeled through osteonal remodeling, which is absent in rats. Despite this, rat models are still very valuable for studying bone, especially cancellous bone. In fact, rat models are the preferred pre-clinical models used to study human osteoporosis[133]. Another species difference is that rats are quadrupeds. Rat bone loading distributions during exercise (and everyday activities) are significantly different from bipedal humans. However, rat bone still remodels in response to the loads placed on it[66], much as human bone does.

Another limitation of our model is that we used only male rats. Women make up an increasing share of active astronauts. Astronauts started as an all-male group in the 1960s, but by the 2010s as many as 20% of astronauts were female[134]. Women are about four times more likely than men to develop osteoporosis later in life[135]. Thus, female astronauts could be at greatest risk for adverse bone outcomes from spaceflight. Including female rats in our study would have given us more relevant results for the growing population of women astronauts and would have increased the generalizability of our study.

5.8.2. Unbalanced Study Design

This study design did not include experimental groups that did not undergo 28 days of hindlimb unloading. Inclusion of a weight-bearing VJE group and weight-bearing SCL group would give the study a fully orthogonal design, which would have allowed us to separate unloading-induced effects from treatment effects and to assess interactions between treatments and unloading. However, we believe that the 50%

increase in number of animals necessary for a fully orthogonal study is too great to justify a fully orthogonal design due to the additional animal use, time, and cost.

5.8.3. No Vehicle Injections

CON, HUC, and VJE animals were not given vehicle injections to match the Scl-Ab injections that SCL rats received. One subcutaneous injection per week was not deemed stressful enough to necessitate replicating in other animals. In addition, previous work in our laboratory[105] that did not administer vehicle injections found results consistent with studies that did use vehicle injections for control groups[106].

5.8.4. Lower Body Weight of VJE Animals

In this study, rats were assigned to groups partially by jumping ability. We intended to block assign animals to groups based only on body weight, but the differential progress of animals in mastering the VJE protocol made this impossible. All animals in this study went through the same acclimation and operant conditioning prior to the study's start. However, the animals did not learn to jump at the same rate.

In each cohort of animals, only a fraction of the animals showed meaningful progress in jump training. The majority of the animals were too timid to advance to an acceptable level of competence. Dr. Lenfest, who developed the jumping protocol, attributes the discrepancy in training progress to the shy-bold continuum[78], a widely-accepted behavioral model in humans and animals[136–138]. Individuals with shy natures are more likely to be cautious in new situations, while bold individuals are more curious and investigative. As a result, shy individuals are at less risk of being preyed upon, but they do not readily use unfamiliar resources[78]. Since the sucrose rewards we used to

train our rats certainly qualify as unfamiliar resources, shy rats did not progress far in the jumping protocol. Instead, VJE rats tended to be those with bold natures that were able to adjust to the new jumping cage, new food rewards, and ever-increasing requirements to receive those rewards. As a result, we were largely at the mercy of the number of bold rats we received, and it was necessary for us to assign rats to groups partly based on jumping ability.

After implementing this assignment scheme, we found that the VJE group had significantly lower body weights compared to all other groups throughout most of the study. However, we believe this issue does not stem from our assignment of the best jumpers to the VJE group. Instead, we believe it stems from logistical issues that we encountered mid experiment. Halfway through the study, the provider of our Scl-Ab cancelled their Scl-Ab development program. As a result, we decided to prioritize completion of the Scl-Ab treatment group while we still had guaranteed access to our source of Scl-Ab. As a result, we backloaded the VJE animals into the last few cohorts.

Unfortunately, the rats that we received in ten cohorts over the seven years of this study did not have uniform body weight. The earlier cohorts were made up of heavier rats than those of the later cohorts, which likely caused most of the differences between the group body weights. VJE animals came primarily from later cohorts composed of smaller rats, while the other groups came primarily from earlier cohorts (although some CON and HUC animals were included in VJE cohorts). However, because we assigned animals to groups partially by jumping ability, we cannot rule out that smaller rats tended to be more capable learners or jumpers.

Regardless of their cause, the differences in body weight we observed could be a confounding factor in this study. Compared to lighter animals, animals with higher body weight need larger bones to support their larger body weights. This means that, all else being equal, the larger bones of larger animals will produce elevated bone outcomes in measurements that do not normalize by bone geometry. In this study, extrinsic three-point bending properties and trabecular thickness are such measures that could be most directly influenced by the differences in body weight of our animals.

5.8.5. Low *n* in GRF Measurement

We were able to successfully measure GRFs in very few of our animals. We attempted to measure the GRFs produced by 19 animals, but only four datasets were usable. The rats are actually very particular about their jumping environment. Altering the environment caused the rats to become tentative and unwilling to perform their tasks.

Data from roughly half of the 19 animals were lost because they were trained in a jumping cage that was not outfitted with the cutaway force platform. These rats would not jump when placed in a nearly identical cage outfitted with the force platform. The remaining five or so animals were lost because they were made nervous by the addition of load cells and wires underneath the clear cage floor, because they were unsettled by the instability of the force platform when load cells were installed, or because their jumping or landing motion made it impossible to separate hindlimb force from forelimb force.

In addition, we were not able to use the force platform to measure resting GRFs on the forelimbs and hindlimbs because the rats simply would not be still. No amount of

food bribes or custom-made boxes could convince them to quietly stand for GRF measurement. As a result, we compared GRF measurements to body weight measured by a laboratory scale.

The *n* reported in a number of published papers for rodent GRF measurement is actually fairly comparable to our *n* of four. Welch et al. also used four animals per group when measuring GRFs of rats that they dropped from various heights[23]. Clarke et al. measured walking GRFs in 10 rats[21], and Schott et al. used three and six rats per group to measure standing GRFs[120]. Regardless of previous studies, our GRF measurements would have likely been more convincing if we were able to assess more animals, and our comparisons would have been more relevant if we had been able measure standing GRFs on the forelimbs and hindlimbs separately.

5.9. Conclusions and Future Work

This study presents a number of opportunities for improvement of current laboratory techniques and for future work. Many of these ideas were addressed above as they arose, but others will be discussed below. The first opportunity for improvement is a direct response to the limitations of our GRF outcomes.

5.9.1. All Rats Should Be Jump Trained in Improved, GRF-Capable Cages

If we measure GRFs in the future, we should alter the current jumping cages so that the presence or absence of load cells does not change the rats' jumping routine in any perceptible way. We were only able to record GRFs for 4/19 animals largely because the animals were too nervous to jump in a new or altered environment. Only one of our two jumping cages was GRF capable, and rats refused to jump when moved from

their usual cage to the slightly altered GRF cage. In the future, all jump cages should be identical, so that load cells can be moved to each rat's preferred jumping environment, rather than moving the rat to the load cells. Additionally, around half of the rats that were trained in the GRF cage refused to jump when load cells were used to support a section of the clear cage floor. In the future, cages should be configured so that including load cells does not change the visual environment or the stability of the force platform cutout. Any changes made should not introduce new distractions, especially smells, to the jumping environment, as the rats already have great difficulty focusing.

5.9.2. More Measures of Bone Turnover Should Be Assessed

In addition to the one measure of bone formation rate and osteoclast surface reported in this study, previous work from this lab[78,125] has assessed a number of bone remodeling outcomes in these same animals. Material and time permitting, these histomorphometry and blood serum analyses should be completed for the full study. Full measures of bone remodeling would allow us to present a more complete picture of the acute and long-term bone responses to jump training and sclerostin-antibody given before a period of disuse.

5.9.3. Full Trabecular Compression Model Should Be Developed for Routine Use

The full trabecular compression FEM model has a number of strengths that would make it a highly useful addition to our lab's standard bone assessments. First, the model allows us to isolate the trabecular structure from the cortical shell, creating a pure test of cancellous bone. In addition, the full trabecular model tests a much larger region of interest than RPC modeling or physical testing, which seem to test mainly the central

cancellous region. Thus, full trabecular simulations would provide a very nice complement to physical RPC testing. For these reasons, the full trabecular compression simulation should be developed into an adequately sensitive simulation and used as a standard bone strength measure for future studies.

5.9.4. NASA Should Consider Preventive Scl-Ab for Exploration Missions

NASA's Human Research Program has deprioritized research on bone-related studies of late, judging that risks from bone loss in space are adequately mitigated[45]. However, in the past NASA researchers have shown interest in preventive drug treatment before long-duration spaceflight. A 2013 panel of NASA researchers recommended the potent and long-lasting antiresorptive zoledronate for exploration missions. Zoledronate would likely be a viable preventive treatment in part because it would only need to be administered before spaceflight, instead of during the mission itself[139].

Scl-Ab treatment could also be a viable preventive countermeasure before long-duration missions. Scl-Ab treatment was incredibly effective in our animals, especially in cancellous bone. In addition, Scl-Ab has thus far shown great success in treating osteoporosis in humans[81]. Administering Scl-Ab in the months leading up to spaceflight would preventively build bone in astronauts, allowing them to lose some bone in space without becoming frail. We found no evidence of rebound bone loss in our healthy, young adult rats, suggesting that healthy, exercising astronauts might not experience rebound bone loss in space as long as they continue to load their bones via resistance

exercise. If NASA still has interest in preventive treatments before exploration missions, they should investigate Scl-Ab.

REFERENCES

1. Carpenter RD, LeBlanc AD, Evans H, Sibonga JD, Lang TF. Long-term changes in the density and structure of the human hip and spine after long-duration spaceflight. Acta Astronaut. 2010;67(1–2):71–81.

2. Lang T, LeBlanc A, Evans H, Lu Y, Genant H, Yu A. Cortical and trabecular bone mineral loss from the spine and hip in long-duration spaceflight. J. Bone Miner. Res. 2004;19(6):1006–12.

3. Lang TF, Leblanc AD, Evans HJ, Lu Y. Adaptation of the proximal femur to skeletal reloading after long-duration spaceflight. J. Bone Miner. Res. 2006;21(8):1224–30.

4. Wolff J. Das gesetz der transformation der knochen. Hirshwald. 1892;1:1–152.

5. Smith SM, Heer MA, Shackelford LC, Sibonga JD, Ploutz-Snyder L, Zwart SR. Benefits for bone from resistance exercise and nutrition in long-duration spaceflight: evidence from biochemistry and densitometry. J. Bone Miner. Res. 2012;27(9):1896–906.

6. Leblanc A, Matsumoto T, Jones J, Shapiro J, Lang T, Shackelford L, Smith SM, Evans H, Spector E, Snyder RP, Sibonga J, Keyak J, Nakamura T, Kohri K, Ohshima H. Bisphosphonates as a supplement to exercise to protect bone during long-duration spaceflight. Osteoporos. Int. 2013;24(7):2105–14.

7. Vico L, van Rietbergen B, Vilayphiou N, Linossier M-T, Locrelle H, Normand M, Zouch M, Gerbaix M, Bonnet N, Novikov V, others. Cortical and Trabecular Bone Microstructure Did Not Recover at Weight-Bearing Skeletal Sites and Progressively Deteriorated at Non-Weight-Bearing Sites During the Year Following International Space Station Missions. J. Bone Miner. Res. 2017;32(10):2010–21.

8. Burkhart K, Allaire B, Anderson DE, Lee D, Keaveny TM, Bouxsein ML. Effects of Long-Duration Spaceflight on Vertebral Strength and Risk of Spine Fracture. J. Bone Miner. Res. Wiley Online Library; 2020;35(2):269–76.

9. Adami S, Zamberlan N. Adverse effects of bisphosphonates. Drug Saf. 1996;14(3):158–70.

10. FDA approves new treatment for osteoporosis in postmenopausal women at high risk of fracture [Internet]. FDA. 2019 [cited 2019 Nov 27]. Available from: http://www.fda.gov/news-events/press-announcements/fda-approves-new-treatment-osteoporosis-postmenopausal-women-high-risk-fracture

11. Morey-Holton ER, Globus R. Hindlimb unloading of growing rats: a model for predicting skeletal changes during space flight. Bone. 1998;22(5):83S-88S.

12. Morey-Holton ER, Globus RK. Hindlimb unloading rodent model: technical aspects. J. Appl. Physiol. 2002;92(4):1367–77.

13. Morey-Holton E, Globus RK, Kaplansky A, Durnova G. The hindlimb unloading rat model: literature overview, technique update and comparison with space flight data. Adv. Space Biol. Med. 2005;10:7–40.

14. Bloomfield S, Allen M, Hogan H, Delp M. Site-and compartment-specific changes in bone with hindlimb unloading in mature adult rats. Bone. 2002;31(1):149–57.

15. Honda A, Sogo N, Nagasawa S, Kato T, Umemura Y. Bones benefits gained by jump training are preserved after detraining in young and adult rats. J. Appl. Physiol. 2008;105(3):849–53.

16. Ju Y-I, Sone T, Ohnaru K, Choi H-J, Choi K-A, Fukunaga M. Jump exercise during hindlimb unloading protect against the deterioration of trabecular bone microarchitecture in growing young rats. Springerplus. 2013;2(1):35.

17. Ju Y-I, Sone T, Ohnaru K, Choi H-J, Fukunaga M. Differential effects of jump versus running exercise on trabecular architecture during remobilization after suspension-induced osteopenia in growing rats. J. Appl. Physiol. 2011;112(5):766–72.

18. Okubo R, Sanada L, Castania V, Louzada M, de Paula F, Maffulli N, Shimano AC. Jumping exercise preserves bone mineral density and mechanical properties in osteopenic ovariectomized rats even following established osteopenia. Osteoporos. Int. 2017;28(4):1461–71.

19. Shimano RC, Yanagihara GR, Macedo AP, Yamanaka JS, Shimano AC, Tavares JMR, Issa JPM. Effects of high-impact exercise on the physical properties of bones of ovariectomized rats fed to a high-protein diet. Scand. J. Med. Sci. Sports. 2018;28(5):1523–31.

20. Silva N, Sousa JJ, Peres E, Sousa A, Ruiz-Armenteros AM, Varejão A, Morais R. A cost-effective instrumented walkway for measuring ground reaction forces in rats to assess gait pattern. Measurement. 2017 Jun;103:241–9.

21. Clarke KA. Differential fore- and hindpaw force transmission in the walking rat. Physiol. Behav. 1995 Sep;58(3):415–9.

22. Zumwalt AC, Hamrick M, Schmitt D. Force plate for measuring the ground reaction forces in small animal locomotion. J. Biomech. 2006;39(15):2877–81.

23. Welch JM, Weaver CM, Turner CH. Adaptations to free-fall impact are different in the shafts and bone ends of rat forelimbs. J. Appl. Physiol. 2004;97(5):1859–65.

24. Spatz JM, Ellman R, Cloutier AM, Louis L, van Vliet M, Suva LJ, Dwyer D, Stolina M, Ke HZ, Bouxsein ML. Sclerostin antibody inhibits skeletal deterioration due to reduced mechanical loading. J. Bone Miner. Res. 2013;28(4):865–74.

25. Bouxsein M, Bateman T, Hanson A, Sullivan L, Ortega A, Livingston E, Marshall E, Pruitt T, Stodieck L, Bowman L, Ellman R, Spatz J, Paszty C, Ferguson V, Lau A, et al. Sclerostin Antibody Treatment Improves Bone Mass, Microarchitecture and Mechanical Properties in Mice Exposed to Microgravity: Results from the STS-135 Shuttle Mission. Minneapolis, MN: ASBMR; 2012.

26. Beggs LA, Ye F, Ghosh P, Beck DT, Conover CF, Balaez A, Miller JR, Phillips EG, Zheng N, Williams AA, others. Sclerostin inhibition prevents spinal cord injury-induced cancellous bone loss. J. Bone Miner. Res. 2015;30(4):681–9.

27. Tian X, Jee WS, Li X, Paszty C, Ke HZ. Sclerostin antibody increases bone mass by stimulating bone formation and inhibiting bone resorption in a hindlimb-immobilization rat model. Bone. 2011;48(2):197–201.

28. Cosman F, de Beur SJ, LeBoff M, Lewiecki E, Tanner B, Randall S, Lindsay R. Clinician's guide to prevention and treatment of osteoporosis. Osteoporos. Int. Springer; 2014;25(10):2359–81.

29. Bonewald LF. The amazing osteocyte. J. Bone Miner. Res. 2011 Feb 1;26(2):229–38.

30. Burr DB, Allen MR. Basic and applied bone biology. Academic Press; 2019.

31. Parfitt AM. Osteonal and hemi-osteonal remodeling: the spatial and temporal framework for signal traffic in adult human bone. J. Cell. Biochem. Wiley Online Library; 1994;55(3):273–86.

32. Raisz LG, others. Pathogenesis of osteoporosis: concepts, conflicts, and prospects. J. Clin. Invest. Am Soc Clin Investig; 2005;115(12):3318–25.

33. Parfitt AM. Trabecular bone architecture in the pathogenesis and prevention of fracture. Am. J. Med. Elsevier; 1987;82(1):68–72.

34. Frost HM. The laws of bone structure. CC Thomas; 1964.

35. Frost HM. Bone “mass” and the “mechanostat”: a proposal. Anat. Rec. Wiley Online Library; 1987;219(1):1–9.

36. Collagen Cross-Link Excretion during Space Flight and Bed Rest1 | The Journal of Clinical Endocrinology & Metabolism | Oxford Academic [Internet]. [cited 2019 Nov 22]. Available from: https://academic.oup.com/jcem/article/83/10/3584/2865642

37. LeBlanc A, Schneider V, Shackelford L, West S, Oganov V, Bakulin A, Voronin L. Bone mineral and lean tissue loss after long duration space flight. J Musculoskelet Neuronal Interact. 2000;1(2):157–60.

38. Loff S. Oct. 31, 2000, Launch of First Crew to International Space Station [Internet]. 15 Years Stn. 2015 [cited 2021 Feb 11]. Available from: https://www.nasa.gov/image-feature/oct-31-2000-launch-of-first-crew-to-international-space-station

39. Cauley JA, Lui L-Y, Stone KL, Hillier TA, Zmuda JM, Hochberg M, Beck TJ, Ensrud KE. Longitudinal study of changes in hip bone mineral density in Caucasian and African-American women. J. Am. Geriatr. Soc. 2005;53(2):183–9.

40. Lang T, LeBlanc A, Evans H, Lu Y, Genant H, Yu A. Cortical and trabecular bone mineral loss from the spine and hip in long-duration spaceflight. J. Bone Miner. Res. 2004;19(6):1006–12.

41. Vico L, Collet P, Guignandon A, Lafage-Proust M-H, Thomas T, Rehailia M, Alexandre C. Effects of long-term microgravity exposure on cancellous and cortical weight-bearing bones of cosmonauts. The Lancet. 2000;355(9215):1607–11.

42. Sibonga JD, Evans HJ, Sung H, Spector E, Lang T, Oganov V, Bakulin A, Shackelford L, LeBlanc A. Recovery of spaceflight-induced bone loss: bone mineral density after long-duration missions as fitted with an exponential function. Bone. 2007;41(6):973–8.

43. NASA. The International Space Station Advanced Resistive Exercise Device [Internet]. NASA; [cited 2021 Feb 11]. Available from: https://technology.nasa.gov/patent/MSC-TOPS-59

44. Smith SM, Zwart SR, Heer M, Hudson EK, Shackelford L, Morgan JL. Men and women in space: bone loss and kidney stone risk after long-duration spaceflight. J. Bone Miner. Res. Wiley Online Library; 2014;29(7):1639–45.

45. Risk of Bone Fracture due to Spaceflight-induced Changes to Bone [Internet]. NASA; 2020 [cited 2021 Feb 11]. Available from: https://humanresearchroadmap.nasa.gov/risks/risk.aspx?i=77

46. Sibonga J, Matsumoto T, Jones J, Shapiro J, Lang T, Shackelford L, Smith S, Young M, Keyak J, Kohri K, others. Resistive exercise in astronauts on prolonged spaceflights provides partial protection against spaceflight-induced bone loss. Bone. Elsevier; 2019;128:112037.

47. Garcia M. Exercise Device for Orion to Pack Powerful Punch [Internet]. Future Hum. Spacefl. 2016 [cited 2021 Feb 11]. Available from: https://www.nasa.gov/image-feature/oct-31-2000-launch-of-first-crew-to-international-space-station

48. Scheuring RA, Mathers CH, Jones JA, Wear ML. Musculoskeletal injuries and minor trauma in space: incidence and injury mechanisms in US astronauts. Aviat. Space Environ. Med. Aerospace Medical Association; 2009;80(2):117–24.

49. Risk of Ineffective or Toxic Medications During Long-Duration Exploration Spaceflight [Internet]. NASA; 2020 [cited 2021 Feb 11]. Available from: https://humanresearchroadmap.nasa.gov/risks/risk.aspx?i=177

50. Morey ER. Spaceflight and bone turnover: correlation with a new rat model of weightlessness. Bioscience. American Institute of Biological Sciences Circulation, AIBS, 1313 Dolley …; 1979;29(3):168–72.

51. Globus RK, Morey-Holton E. Hindlimb unloading: rodent analog for microgravity. J. Appl. Physiol. 2016;120(10):1196–206.

52. Bloomfield SA, Martinez DA, Boudreaux RD, Mantri AV. Microgravity stress: bone and connective tissue. Compr. Physiol. Wiley Online Library; 2011;6(2):645–86.

53. Swift JM, Swift SN, Nilsson MI, Hogan HA, Bouse SD, Bloomfield SA. Cancellous bone formation response to simulated resistance training during disuse is blunted by concurrent alendronate treatment. J. Bone Miner. Res. 2011;26(9):2140–50.

54. Allen M, Hogan H, Bloomfield S. Differential bone and muscle recovery following hindlimb unloading in skeletally mature male rats. J. Musculoskelet. Neuronal Interact. 2006;6(3):217.

55. Shirazi-Fard Y, Kupke JS, Bloomfield SA, Hogan HA. Discordant recovery of bone mass and mechanical properties during prolonged recovery from disuse. Bone. 2013;52(1):433–43.

56. Shirazi-Fard Y, Metzger CE, Kwaczala AT, Judex S, Bloomfield SA, Hogan HA. Moderate intensity resistive exercise improves metaphyseal cancellous bone recovery following an initial disuse period, but does not mitigate decrements during a subsequent disuse period in adult rats. Bone. 2014;66:296–305.

57. Shirazi-Fard Y, Anthony RA, Kwaczala AT, Judex S, Bloomfield SA, Hogan HA. Previous exposure to simulated microgravity does not exacerbate bone loss during subsequent exposure in the proximal tibia of adult rats. Bone. 2013;56(2):461–73.

58. Swift JM, Nilsson MI, Hogan HA, Sumner LR, Bloomfield SA. Simulated resistance training during hindlimb unloading abolishes disuse bone loss and maintains muscle strength. J. Bone Miner. Res. 2010;25(3):564–74.

59. Macias BR, Swift JM, Nilsson MI, Hogan HA, Bouse SD, Bloomfield SA. Simulated resistance training, but not alendronate, increases cortical bone formation and suppresses sclerostin during disuse. J. Appl. Physiol. 2011;112(5):918–25.

60. Bloomfield SA, Allen MR, Hogan HA, Delp MD. Site- and compartment-specific changes in bone with hindlimb unloading in mature adult rats. Bone. 2002;31(1):149–57.

61. Black JM. Comparison of the Persisting Effects of Bisphosphonate Treatments Prior to Hindlimb Unloading on Mechanical and Densitometric Properties in the Tibia of Adult Male Rats [PhD Thesis]. 2016.

62. Kosniewski JL. The Efficacy of Bisphosphonate Pre-treatment in Preventing Losses in Densitometric and Mechanical Properties during Hindlimb Unloading and throughout Reambulation in the Distal Femur Metaphysis of Adult Male Rats [PhD Thesis]. 2017.

63. Rubin CT, Lanyon LE. Regulation of bone mass by mechanical strain magnitude. Calcif. Tissue Int. Springer; 1985;37(4):411–7.

64. Rubin C, Gross T, Qin Y-X, Fritton S, Guilak F, McLEOD K. Differentiation of the bone-tissue remodeling response to axial and torsional loading in the turkey ulna. JBJS. LWW; 1996;78(10):1523–33.

65. Lanyon LE, Rubin C. Static vs dynamic loads as an influence on bone remodelling. J. Biomech. Elsevier; 1984;17(12):897–905.

66. Boppart MD, Kimmel D, Yee J, Cullen D. Time course of osteoblast appearance after in vivo mechanical loading. Bone. 1998;23(5):409–15.

67. Morse A, McDonald MM, Kelly NH, Melville KM, Schindeler A, Kramer I, Kneissel M, van der Meulen MC, Little DG. Mechanical load increases in bone formation via a sclerostin-independent pathway. J. Bone Miner. Res. 2014;29(11):2456–67.

68. Schiessl H, Frost H, Jee W. Estrogen and bone-muscle strength and mass relationships. Bone. Elsevier; 1998;22(1):1–6.

69. Hubal M, Ingalls C, Allen M, Wenke J, Hogan H, Bloomfield S. Effects of eccentric exercise training on cortical bone and muscle strength in the estrogen-deficient mouse. J. Appl. Physiol. 2005;98(5):1674–81.

70. Umemura Y, Ishiko T, Yamauchi T, Kurono M, Mashiko S. Five jumps per day increase bone mass and breaking force in rats. J. Bone Miner. Res. 1997;12(9):1480–5.

71. Yanagihara G, Paiva A, Gasparini G, Macedo AP, Frighetto P, Volpon JB, Shimano AC. High-impact exercise in rats prior to and during suspension can prevent bone loss. Braz. J. Med. Biol. Res. 2016;49(3).

72. Fluckey JD, Kraemer WJ, Farrell PA. Pancreatic islet insulin secretion is increased after resistance exercise in rats. J. Appl. Physiol. 1995;79(4):1100–5.

73. Fluckey JD, Vary TC, Jefferson LS, Evans WJ, Farrell PA. Insulin stimulation of protein synthesis in rat skeletal muscle following resistance exercise is maintained with advancing age. J. Gerontol. A. Biol. Sci. Med. Sci. 1996;51(5):B323-M330.

74. Fluckey J, Dupont-Versteegden E, Montague D, Knox M, Tesch P, Peterson C, Gaddy-Kurten D. A rat resistance exercise regimen attenuates losses of musculoskeletal mass during hindlimb suspension. Acta Physiol. Scand. 2002;176(4):293–300.

75. Skinner BF. Science and human behavior. Simon and Schuster; 1965.

76. Lawson R, Watson Jr LS. Learning in the rat (Rattus Norvegicus) under positive vs. negative reinforcement with incentive conditions controlled. 1963;

77. Cooper JJ, Cracknell N, Hardiman J, Wright H, Mills D. The welfare consequences and efficacy of training pet dogs with remote electronic training collars in comparison to reward based training. PloS One. 2014;9(9):e102722.

78. Lenfest SE. Skeletal Effects of Bisphosphonate Treatment and Jumping Resistance Exercise on Adult Rats Exposed to Simulated Microgravity [Internet] [Doctoral dissertation]. Texas A&M University; 2020. Available from: https : / /hdl .handle .net /1969 .1 /191737.

79. van Lierop AH, Appelman-Dijkstra NM, Papapoulos SE. Sclerostin deficiency in humans. Bone. Elsevier; 2017;96:51–62.

80. Lim SY, Bolster MB. Profile of romosozumab and its potential in the management of osteoporosis. Drug Des. Devel. Ther. Dove Press; 2017;11:1221.

81. McClung MR. Romosozumab for the treatment of osteoporosis. Osteoporos. Sarcopenia. Elsevier; 2018;4(1):11–5.

82. Zhang D, Hu M, Chu T, Lin L, Wang J, Li X, Ke HZ, Qin Y-X. Sclerostin antibody prevented progressive bone loss in combined ovariectomized and concurrent functional disuse. Bone. Elsevier; 2016;87:161–8.

83. Tian X, Setterberg RB, Li X, Paszty C, Ke HZ, Jee WS. Treatment with a sclerostin antibody increases cancellous bone formation and bone mass regardless of marrow composition in adult female rats. Bone. 2010;47(3):529–33.

84. Spatz J, Ellman R, Cloutier A, Louis L, van Vliet M, Dwyer D, Stolina M, Ke H, Bouxsein M. Sclerostin antibody inhibits skeletal deterioration in mice exposed to partial weight-bearing. Life Sci. Space Res. Elsevier; 2017;12:32–8.

85. Sullivan L, Ortega A, Bateman T, Hanson A, Livingston E, Marshall E, Pruitt T, Stodieck L, Bowman L, Ellman R, Spatz J, Paszty C, Bouxsein M, Ferguson V, Lau A, et al. Effects of Spaceflight and Sclerostin Antibody on Femoral Neck Strength in Estimated by Finite Element Analysis in Mice flown on Space Shuttle Flight STS-135. Baltimore, MD: ASBMR; 2013.

86. Marshall, E, Sullivan L, Livingston E, Hanson A, Pruitt T, Stodieck L, Bowman L, Ellman R, Spatz J, Paszty C, Bouxsein M, Ferguson V, Bateman T, Lau A. Effects of Spaceflight on the “Non-Weight Bearing” L5 Vertebra Measured by Finite Element Analysis in Mice Flown on Space Shuttle Flight STS-135. Baltimore, MD: ASBMR; 2013.

87. Lau A, Ortega A, Bouxsein M, Bateman T, Hanson A, Marshall, E, Sullivan L, Livingston E, Pruitt T, Stodieck L, Bowman L, Ellman R, Spatz J, Paszty C, Ferguson V, et al. Effects of Spaceflight and a Sclerostin Antibody Countermeasure on the Mechanical Properties of Bone in Mice. Minneapolis, MN: ASBMR; 2012.

88. Horne AM, Mihov B, Reid IR. Bone loss after romosozumab/denosumab: effects of bisphosphonates. Calcif. Tissue Int. Springer; 2018;103(1):55–61.

89. Hogan HA, Ruhmann SP, Sampson HW. The mechanical properties of cancellous bone in the proximal tibia of ovariectomized rats. J. Bone Miner. Res. 2000;15(2):284–92.

90. Ashman RB, Corin JD, Turner CH. Elastic properties of cancellous bone: measurement by an ultrasonic technique. J. Biomech. Elsevier; 1987;20(10):979–86.

91. Keaveny TM, Guo XE, Wachtel EF, McMahon TA, Hayes WC. Trabecular bone exhibits fully linear elastic behavior and yields at low strains. J. Biomech. 1994;27(9):1127–36.

92. Kopperdahl DL, Keaveny TM. Yield strain behavior of trabecular bone. J. Biomech. 1998;31(7):601–8.

93. Keaveny TM, Pinilla TP, Crawford RP, Kopperdahl DL, Lou A. Systematic and random errors in compression testing of trabecular bone. J. Orthop. Res. Wiley Online Library; 1997;15(1):101–10.

94. Öhman C, Baleani M, Perilli E, Dall'Ara E, Tassani S, Baruffaldi F, Viceconti M. Mechanical testing of cancellous bone from the femoral head: experimental errors due to off-axis measurements. J. Biomech. Elsevier; 2007;40(11):2426–33.

95. Martens M, Van Audekercke R, Delport P, De Meester P, Mulier J. The mechanical characteristics of cancellous bone at the upper femoral region. J. Biomech. Elsevier; 1983;16(12):971–83.

96. Linde F, Sørensen HCF. The effect of different storage methods on the mechanical properties of trabecular bone. J. Biomech. Elsevier; 1993;26(10):1249–52.

97. Lucas M. A NOVEL METHOD FOR THE EVALUATION OF MECHANICAL PROPERTIES OF CANCELLOUS BONE IN THE RAT DISTAL FEMUR [Master's thesis]. [College Station, Texas]: Texas A&M University; 2009.

98. van Rietbergen B, Weinans H, Huiskes R, Odgaard A. A new method to determine trabecular bone elastic properties and loading using micromechanical finite-element models. J. Biomech. 1995;28(1):69–81.

99. Sas A, Tanck E, Sermon A, van Lenthe GH. Finite element models for fracture prevention in patients with metastatic bone disease. A literature review. Bone Rep. Elsevier; 2020;100286.

100. Viceconti M, Qasim M, Bhattacharya P, Li X. Are CT-based finite element model predictions of femoral bone strengthening clinically useful? Curr. Osteoporos. Rep. Springer; 2018;16(3):216–23.

101. Schileo E, Dall'Ara E, Taddei F, Malandrino A, Schotkamp T, Baleani M, Viceconti M. An accurate estimation of bone density improves the accuracy of subject-specific finite element models. J. Biomech. 2008;41(11):2483–91.

102. Bourne BC, van der Meulen MC. Finite element models predict cancellous apparent modulus when tissue modulus is scaled from specimen CT-attenuation. J. Biomech. Elsevier; 2004;37(5):613–21.

103. Easley SK, Jekir MG, Burghardt AJ, Li M, Keaveny TM. Contribution of the intra-specimen variations in tissue mineralization to PTH-and raloxifene-induced changes in stiffness of rat vertebrae. Bone. Elsevier; 2010;46(4):1162–9.

104. Kohn Z. Micro-CT Image-Based Mesh Generation and Finite Element Analysis of Bone [Internet] [Master's thesis]. Texas A&M University; 2020. Available from: https : / /hdl .handle .net /1969 .1 /191721

105. Boudreaux R. Sequential High-Impact, Free-Fall Loading and Zoledronic Acid as a Novel Pre-Treatment for Disuse-Induced Bone Loss [PhD Thesis]. 2014.

106. Gasser JA, Ingold P, Venturiere A, Shen V, Green JR. Long-term protective effects of zoledronic acid on cancellous and cortical bone in the ovariectomized rat. J. Bone Miner. Res. Wiley Online Library; 2008;23(4):544–51.

107. McLellan CP, Lovell DI, Gass GC. The role of rate of force development on vertical jump performance. J. Strength Cond. Res. 2011;25(2):379–85.

108. Ebben W, Flanagan E, Jensen R. GENDER SIMILARITIES IN RATE OF FORCE DEVELOPMENT AND TIME TO TAKEOFF DURING THE COUNTERMOVEMENT JUMP. J. Exerc. Physiol. Online. 2007;10(6).

109. Dempster DW, Compston JE, Drezner MK, Glorieux FH, Kanis JA, Malluche H, Meunier PJ, Ott SM, Recker RR, Parfitt AM. Standardized Nomenclature, Symbols, and Units for Bone Histomorphometry: A 2012 Update of the Report of the ASBMR Histomorphometry Nomenclature Committee. J. Bone Miner. Res. Off. J. Am. Soc. Bone Miner. Res. 2013;28(1):2–17.

110. Allen MR, Hogan HA, Hobbs WA, Koivuniemi AS, Koivuniemi MC, Burr DB. Raloxifene enhances material-level mechanical properties of femoral cortical and trabecular bone. Endocrinology. Oxford University Press; 2007;148(8):3908–13.

111. Herberich E, Sikorski J, Hothorn T. A robust procedure for comparing multiple means under heteroscedasticity in unbalanced designs. PloS One. Public Library of Science; 2010;5(3):e9788.

112. Ulrich D, van Rietbergen B, Weinans H, Rüegsegger P. Finite element analysis of trabecular bone structure: a comparison of image-based meshing techniques. J. Biomech. 1998;31(12):1187–92.

113. Pistoia W, Van Rietbergen B, Lochmüller E-M, Lill C, Eckstein F, Rüegsegger P. Estimation of distal radius failure load with micro-finite element analysis models based on three-dimensional peripheral quantitative computed tomography images. Bone. 2002;30(6):842–8.

114. Eswaran SK, Gupta A, Adams MF, Keaveny TM. Cortical and trabecular load sharing in the human vertebral body. J. Bone Miner. Res. Wiley Online Library; 2006;21(2):307–14.

115. Turner CH, Takano Y, Owan I. Aging changes mechanical loading thresholds for bone formation in rats. J. Bone Miner. Res. Wiley Online Library; 1995;10(10):1544–9.

116. Rubin CT, Bain SD, McLeod KJ. Suppression of the osteogenic response in the aging skeleton. Calcif. Tissue Int. Springer; 1992;50(4):306–13.

117. Steinberg ME, Trueta J. Effects of activity on bone growth and development in the rat. Clin. Orthop. 1981;(156):52–60.

118. Honda A, Sogo N, Nagasawa S, Shimizu T, Umemura Y. High-impact exercise strengthens bone in osteopenic ovariectomized rats with the same outcome as Sham rats. J. Appl. Physiol. American Physiological Society; 2003;95(3):1032–7.

119. Swift JM, Gasier HG, Swift SN, Wiggs MP, Hogan HA, Fluckey JD, Bloomfield SA. Increased training loads do not magnify cancellous bone gains with rodent jump resistance exercise. J. Appl. Physiol. 2010;109(6):1600–7.

120. Schött E, Berge O-G, Ängeby-Möller K, Hammarström G, Dalsgaard C-J, Brodin E. Weight bearing as an objective measure of arthritic pain in the rat. J. Pharmacol. Toxicol. Methods. 1994 Apr 1;31(2):79–83.

121. Turner CH. Three rules for bone adaptation to mechanical stimuli. Bone. 1998;23(5):399–407.

122. Li X, Ominsky MS, Warmington KS, Morony S, Gong J, Cao J, Gao Y, Shalhoub V, Tipton B, Haldankar R, others. Sclerostin antibody treatment increases bone formation, bone mass, and bone strength in a rat model of postmenopausal osteoporosis. J. Bone Miner. Res. 2009;24(4):578–88.

123. Hamann C, Rauner M, Höhna Y, Bernhardt R, Mettelsiefen J, Goettsch C, Günther K-P, Stolina M, Han C-Y, Asuncion FJ, others. Sclerostin antibody

treatment improves bone mass, bone strength, and bone defect regeneration in rats with type 2 diabetes mellitus. J. Bone Miner. Res. 2013;28(3):627–38.

124. Boudreaux RD, Swift JM, Gasier HG, Wiggs MP, Hogan HA, Fluckey JD, Bloomfield SA. Increased resistance during jump exercise does not enhance cortical bone formation. Med. Sci. Sports Exerc. NIH Public Access; 2014;46(5):982.

125. Brezicha JE. Skeletal Responses to Simulated Microgravity in the Adult Rat Model after Sclerostin Antibody Pretreatment [Internet] [Doctoral dissertation]. Texas A&M University; 2019. Available from: https : / /hdl .handle .net /1969 .1 /188988.

126. Van Rietbergen B, Ito K. A survey of micro-finite element analysis for clinical assessment of bone strength: the first decade. J. Biomech. Elsevier; 2015;48(5):832–41.

127. Burghardt AJ, Issever AS, Schwartz AV, Davis KA, Masharani U, Majumdar S, Link TM. High-Resolution Peripheral Quantitative Computed Tomographic Imaging of Cortical and Trabecular Bone Microarchitecture in Patients with Type 2 Diabetes Mellitus. J. Clin. Endocrinol. Metab. 2010;95(11):5045–55.

128. Ackerman KE, Putman M, Guereca G, Taylor AP, Pierce L, Herzog DB, Klibanski A, Bouxsein M, Misra M. Cortical microstructure and estimated bone strength in young amenorrheic athletes, eumenorrheic athletes and non-athletes. Bone. Elsevier; 2012;51(4):680–7.

129. Niebur G, Yuen J, Hsia A, Keaveny T. Convergence behavior of high-resolution finite element models of trabecular bone. 1999;

130. Nawathe S, Akhlaghpour H, Bouxsein ML, Keaveny TM. Microstructural failure mechanisms in the human proximal femur for sideways fall loading. J. Bone Miner. Res. Wiley Online Library; 2014;29(2):507–15.

131. Nawathe S, Nguyen BP, Barzanian N, Akhlaghpour H, Bouxsein ML, Keaveny TM. Cortical and trabecular load sharing in the human femoral neck. J. Biomech. Elsevier; 2015;48(5):816–22.

132. Boutroy S, Van Rietbergen B, Sornay-Rendu E, Munoz F, Bouxsein ML, Delmas PD. Finite element analysis based on in vivo HR-pQCT images of the distal radius is associated with wrist fracture in postmenopausal women. J. Bone Miner. Res. Wiley Online Library; 2008;23(3):392–9.

133. Lelovas PP, Xanthos TT, Thoma SE, Lyritis GP, Dontas IA. The laboratory rat as an animal model for osteoporosis research. Comp. Med. American Association for Laboratory Animal Science; 2008;58(5):424–30.

134. Smith MG, Kelley M, Basner M. A brief history of spaceflight from 1961 to 2020: An analysis of missions and astronaut demographics. Acta Astronaut. Elsevier; 2020;175:290–9.

135. French KD, Emanuele D. Osteoporosis: Increasing Screening and Treatment for Postmenopausal Women. J. Nurse Pract. Elsevier; 2019;15(5):347–50.

136. Oswald ME, Singer M, Robison BD. The quantitative genetic architecture of the bold-shy continuum in zebrafish, Danio rerio. PloS One. Public Library of Science; 2013;8(7):e68828.

137. Wilson DS, Coleman K, Clark AB, Biederman L. Shy-bold continuum in pumpkinseed sunfish (Lepomis gibbosus): An ecological study of a psychological trait. J. Comp. Psychol. American Psychological Association; 1993;107(3):250.

138. Franks B, Higgins ET, Champagne FA. A theoretically based model of rat personality with implications for welfare. PLoS One. Public Library of Science; 2014;9(4):e95135.

139. Orwoll ES, Adler RA, Amin S, Binkley N, Lewiecki EM, Petak SM, Shapses SA, Sinaki M, Watts NB, Sibonga JD. Skeletal health in long-duration astronauts: nature, assessment, and management recommendations from the NASA Bone Summit. J. Bone Miner. Res. Wiley Online Library; 2013;28(6):1243–55.

APPENDIX A. FULL NUMERICAL RESULTS

Appendix A contains all numerical results for group means from this study. All data are mean ± standard deviation.

Table A.1. Number of animals available for *ex vivo* measures

N	Baseline *d0*	End of Pretreatment *d28*	End of HU *d56*	End of Recovery *d112*
CON	7	18	16	22
HUC	---	---	13	14
VJE	---	15	15	15
SCL	---	15	14	15

Table A.2. Animal Body weights

	Baseline *d0*	End of Pretreatment *d28*	End of HU *d56*	End of Recovery *d112*
CON	430 ± 59	437 ± 65	473 ± 62	501 ± 52
HUC	457 ± 36	477 ± 46	483 ± 35	532 ± 44
VJE	373 ± 31	391.4 ± 40.3	432 ± 50	460 ± 47
*SCL	429 ± 29	428 ± 22	473 ± 33	540 ± 38

Table A.3. *Ex vivo* pQCT VJE vs CON results

	Distal Femur		Proximal Humerus	
	CON	**VJE**	**CON**	**VJE**
Total vBMD (mg/cm³)	609.5±34.47	671.0±31.66	634.4±35.15	710.7±57.88
Cancellous vBMD (mg/cm³)	290.2±45.80	329.5±63.13	215.3±27.62	216.3±47.60
Cortical vBMD (mg/cm³)	616.8±32.73	674.7±28.86	643.6±32.99	716.8±54.06

Table A.4. Histomorphometry VJE vs CON results

	Proximal Tibia		Proximal Humerus	
	CON	**VJE**	**CON**	**VJE**
BV/TV (%)	17.10±3.685	22.14±3.367	9.702±2.951	17.49±5.118
OS/BS (%)	1.118±0.357	1.708±0.696	1.388±1.032	3.699±1.770
OcS/BS(%)	1.593±0.578	1.024±0.491	3.482±1.691	1.522±0.507
Tb.Th (μm)	70.30±8.784	77.85±8.863	53.94±9.840	68.25±14.03
Tb.Sp (μm)	361.7±121.1	285.3±66.81	531.4±113.2	342.3±84.08
Tb.N (#/mm)	2.462±0.614	2.833±0.455	1.775±0.397	2.527±0.450
MS/BS (%)	5.189±1.212	6.554±1.511	8.751±1.413	11.61±1.885
MAR (μm/d)	0.924±0.138	1.008±0.163	0.749±0.151	0.974±0.099
BFR (μm²/μm³/d)	0.048±0.013	0.065±0.020	0.066±0.014	0.113±0.025

Table A.5. Three-point bending results

		CON	HUC	VJE	SCL
Anterior-Posterior Diameter (mm)	*d0*	4.021±0.170	-	-	-
	d28	3.921±0.215	-	3.682±0.165	3.922±0.281
	d56	3.896±0.229	4.082±0.228	3.992±0.218	3.923±0.142
	d112	4.012±0.255	4.185±0.162	3.835±0.239	4.141±0.150
Cross-Sectional Moment of Inertia (mm^4)	*d0*	14.34±2.520	-	-	-
	d28	13.66±2.410	-	10.98±1.076	14.89±2.237
	d56	13.64±2.327	15.27±3.049	14.21±2.639	14.19±1.976
	d112	15.17±3.288	16.63±2.726	12.49±3.027	17.88±2.611
Stiffness (N/mm)	*d0*	607.0±55.57	-	-	-
	d28	576.6±93.59	-	559.3±57.04	647.4±123.5
	d56	613.4±91.87	588.5±108.6	593.4±111.8	608.7±95.96
	d112	609.3±135.3	537.4±138.3	659.2±127.7	728.0±94.63
Ultimate Force (N)	*d0*	238.4±15.49	-	-	-
	d28	261.4±22.87	-	240.8±22.73	270.7±28.64
	d56	262.3±27.40	262.6±19.56	275.3±37.13	277.5±30.16
	d112	270.6±41.74	283.6±26.80	269.4±38.18	315.1±20.65
Yield Force (N)	*d0*	126.3±25.43	-	-	-
	d28	160.0±34.26	-	174.3±14.89	197.7±20.37
	d56	164.6±43.65	156.6±29.48	169.0±31.38	188.4±23.81
	d112	186.0±38.36	194.6±61.63	185.3±26.18	206.7±29.84
Displacement at Yield (mm)	*d0*	0.211±0.032	-	-	-
	d28	0.292±0.096	-	0.320±0.050	0.303±0.034
	d56	0.285±0.128	0.283±0.104	0.292±0.049	0.320±0.059
	d112	0.339±0.174	0.406±0.206	0.291±0.055	0.291±0.042
Displacement at Max Force (mm)	*d0*	0.685±0.076	-	-	-
	d28	0.751±0.088	-	0.706±0.098	0.685±0.108
	d56	0.727±0.109	0.734±0.159	0.756±0.145	0.717±0.114
	d112	0.731±0.153	0.816±0.113	0.651±0.072	0.764±0.152
Displacement at Fracture (mm)	*d0*	0.801±0.145	-	-	-
	d28	0.802±0.096	-	0.775±0.102	0.691±0.115
	d56	0.788±0.125	0.775±0.172	0.815±0.108	0.783±0.161
	d112	0.751±0.149	0.843±0.134	0.727±0.076	0.764±0.152

	Distal Femur		Proximal Humerus	
	CON	VJE	CON	VJE
Total vBMD (mg/cm3)	609.5±34.47	671.0±31.66	634.4±35.15	710.7±57.88
Cancellous vBMD (mg/cm3)	290.2±45.80	329.5±63.13	215.3±27.62	216.3±47.60
Cortical vBMD (mg/cm3)	616.8±32.73	674.7±28.86	643.6±32.99	716.8±54.06

Table A.4. Histomorphometry VJE vs CON results

	Proximal Tibia		Proximal Humerus	
	CON	VJE	CON	VJE
BV/TV (%)	17.10±3.685	22.14±3.367	9.702±2.951	17.49±5.118
OS/BS (%)	1.118±0.357	1.708±0.696	1.388±1.032	3.699±1.770
OcS/BS(%)	1.593±0.578	1.024±0.491	3.482±1.691	1.522±0.507
Tb.Th (µm)	70.30±8.784	77.85±8.863	53.94±9.840	68.25±14.03
Tb.Sp (µm)	361.7±121.1	285.3±66.81	531.4±113.2	342.3±84.08
Tb.N (#/mm)	2.462±0.614	2.833±0.455	1.775±0.397	2.527±0.450
MS/BS (%)	5.189±1.212	6.554±1.511	8.751±1.413	11.61±1.885
MAR (µm/d)	0.924±0.138	1.008±0.163	0.749±0.151	0.974±0.099
BFR (µm2/µm3/d)	0.048±0.013	0.065±0.020	0.066±0.014	0.113±0.025

Table A.5. Three-point bending results**Continued**

		CON	HUC	VJE	SCL
Energy to Yield (mJ)	*d0*	14.88±4.670	-	-	-
	d28	26.25±14.67	-	30.18±6.872	31.53±4.686
	d56	27.52±22.52	24.38±13.52	26.45±8.132	33.72±9.654
	d112	35.83±23.05	44.78±32.71	29.44±8.999	33.53±9.787
Energy to Fracture (mJ)	*d0*	132.3±36.52	-	-	-
	d28	138.2±25.97	-	128.3±22.40	123.4±24.73
	d56	138.5±29.07	132.8±44.90	149.2±35.28	146.8±45.71
	d112	134.0±43.94	148.8±26.75	132.6±17.10	158.8±41.56
Modulus (GPa)	*d0*	3.037±0.489	-	-	-
	d28	3.018±0.522	-	3.611±0.487	3.075±0.543
	d56	3.266±0.781	2.853±0.555	2.982±0.559	3.043±0.491
	d112	2.917±0.836	2.322±0.709	3.779±0.517	2.927±0.639
Yield Stress (MPa)	*d0*	67.95±17.88	-	-	-
	d28	90.47±33.79	-	109.9±8.478	98.71±14.32
	d56	89.56±23.70	79.81±16.44	90.06±14.90	98.38±10.43
	d112	96.52±29.49	92.92±29.32	109.9±20.04	90.75±14.73
Ultimate Stress (MPa)	*d0*	127.1±12.76	-	-	-
	d28	144.0±24.75	-	151.7±10.63	134.7±16.30
	d56	142.4±17.42	133.3±15.27	148.0±23.98	144.8±13.04
	d112	138.2±27.16	135.5±16.06	157.7±10.02	138.3±14.21
Pre-Yield Toughness (mJ/mm^3)	*d0*	0.856±0.307	-	-	-
	d28	1.579±1.131	-	1.860±0.358	1.628±0.334
	d56	1.535±1.188	1.294±0.739	1.494±0.427	1.846±0.541
	d112	1.991±1.424	2.364±1.646	1.793±0.613	1.619±0.473
Post-Yield Displacement (mm)	*d0*	0.590±0.162	-	-	-
	d28	0.509±0.153	-	0.455±0.087	0.387±0.107
	d56	0.502±0.133	0.492±0.188	0.523±0.125	0.463±0.157
	d112	0.412±0.176	0.437±0.155	0.435±0.072	0.473±0.138

Table A.6. microCT results

		CON	HUC	VJE	SCL
BV/TV (cm^3/cm^3)	*d0*	0.275±0.070	-	-	-
	d28	0.207±0.040	-	0.238±0.049	0.305±0.069
	d56	0.213±0.058	0.171±0.050	0.270±0.069	0.348±0.060
	d112	0.190±0.039	0.167±0.033	0.225±0.034	0.256±0.035
Conn.D ($1/mm^3$)	*d0*	60.93±12.63	-	-	-
	d28	45.82±10.76	-	51.46±10.25	46.99±9.443
	d56	43.05±12.47	37.60±9.333	48.29±13.30	46.11±6.793
	d112	34.89±10.91	31.94±10.24	40.72±8.404	35.78±6.230
SMI	*d0*	1.188±0.539	-	-	-
	d28	1.811±0.309	-	1.522±0.378	1.346±0.648
	d56	1.834±0.503	2.188±0.330	1.430±0.573	1.051±0.447
	d112	1.997±0.373	2.265±0.279	1.698±0.301	1.632±0.301
Tb.N (1/mm)	*d0*	3.495±0.419	-	-	-
	d28	3.150±0.355	-	3.195±0.478	3.341±0.380
	d56	3.100±0.427	3.068±0.327	3.222±0.530	3.289±0.358
	d112	2.916±0.431	2.875±0.403	3.121±0.303	3.065±0.249
Tb.Th (mm)	*d0*	0.099±0.011	-	-	-
	d28	0.091±0.007	-	0.095±0.007	0.118±0.009
	d56	0.093±0.009	0.084±0.008	0.104±0.006	0.133±0.014
	d112	0.097±0.032	0.092±0.002	0.098±0.007	0.117±0.007
Tb.Sp (mm)	*d0*	0.279±0.042	-	-	-
	d28	0.312±0.044	-	0.312±0.059	0.272±0.040
	d56	0.314±0.048	0.318±0.036	0.300±0.071	0.270±0.047
	d112	0.341±0.063	0.339±0.054	0.307±0.039	0.301±0.032
TMD (mg/cm^3)	*d0*	954.7±31.89	-	-	-
	d28	977.4±20.63	-	982.2±18.69	998.7±12.27
	d56	953.4±23.67	957.5±30.82	940.9±22.20	971.6±17.10
	d112	996.2±29.51	999.6±23.30	997.8±18.30	1024.±15.35

Table A.7. Reduced platen compression results

		CON	HUC	VJE	SCL
Stiffness (N/mm)	*d0*	35.23±23.64	-	-	-
	d28	57.75±57.23	-	59.45±63.29	153.6±79.25
	d56	61.46±50.33	36.70±36.19	90.61±52.83	165.5±96.19
	d112	44.76±47.22	53.46±47.52	74.45±43.45	151.2±35.71
Max Force (N)	*d0*	2.905±1.811	-	-	-
	d28	4.982±5.435	-	5.070±6.476	15.83±11.73
	d56	5.685±4.291	3.089±2.814	7.364±5.026	18.92±15.44
	d112	4.559±4.748	4.461±3.226	6.194±4.680	13.69±6.364
Yield Force (N)	*d0*	1.335±0.716	-	-	-
	d28	3.533±3.972	-	4.281±6.316	12.18±9.898
	d56	4.326±3.715	2.354±2.334	5.235±4.021	14.36±13.21
	d112	3.062±2.583	3.185±2.264	3.349±2.296	9.591±4.103
Platen Size (mm)	*d0*	2.060±0.106	-	-	-
	d28	2.064±0.234	-	1.767±0.169	2.070±0.208
	d56	2.053±0.221	2.155±0.242	2.032±0.202	2.148±0.193
	d112	2.018±0.239	2.229±0.211	2±0.247	2.227±0.183
Specimen Thickness (mm)	*d0*	2.025±0.045	-	-	-
	d28	2.101±0.105	-	1.996±0.109	2.049±0.085
	d56	2.016±0.103	2.048±0.183	2.120±0.069	2.107±0.097
	d112	2.010±0.128	1.966±0.089	1.97±0.078	2.045±0.098
Displacement at Yield (mm)	*d0*	0.047±0.021	-	-	-
	d28	0.059±0.035	±	0.059±0.022	0.081±0.035
	d56	0.074±0.037	0.076±0.034	0.055±0.016	0.076±0.032
	d112	0.087±0.041	0.084±0.043	0.048±0.011	0.066±0.022
Displacement at Max Force (mm)	*d0*	0.257±0.137	-	-	-
	d28	0.218±0.157	-	0.115±0.049	0.164±0.077
	d56	0.232±0.125	0.278±0.138	0.199±0.170	0.245±0.139
	d112	0.205±0.110	0.222±0.155	0.189±0.136	0.197±0.134
Energy to Max Force (mJ)	*d0*	0.480±0.353	-	-	-
	d28	0.662±0.863	-	0.411±0.490	2.092±2.215
	d56	1.017±0.987	0.523±0.483	0.837±0.777	2.853±2.198
	d112	0.681±0.936	0.576±0.409	0.826±1.030	2.025±1.988

Table A.7. Reduced platen compression results

		CON	HUC	VJE	SCL
Strain at Yield (mm/mm)	*d0*	0.023±0.010	-	-	-
	d28	0.027±0.015	-	0.030±0.011	0.040±0.017
	d56	0.037±0.019	0.037±0.018	0.026±0.007	0.036±0.015
	d112	0.043±0.020	0.043±0.023	0.024±0.006	0.032±0.010
Yield Stress (MPa)	*d0*	0.402±0.233	-	-	-
	d28	0.943±0.923	-	1.525±1.967	3.592±2.920
	d56	1.187±0.870	0.567±0.454	1.465±0.879	3.666±3.080
	d112	0.889±0.625	0.835±0.644	0.988±0.443	2.424±0.783
Modulus (MPa)	*d0*	21.04±14.04	-	-	-
	d28	33.93±28.99	-	43.77±38.27	93.46±47.58
	d56	33.80±20.94	18.53±16.22	55.66±24.19	92.75±48.13
	d112	26.21±22.05	27.63±26.53	44.70±21.40	79.63±18.91
Ultimate Stress (MPa)	*d0*	0.867±0.523	-	-	-
	d28	1.325±1.213	-	1.820±1.996	4.684±3.446
	d56	1.573±0.980	0.748±0.576	2.104±1.105	4.831±3.532
	d112	1.309±1.064	1.149±0.861	1.819±1.032	3.417±1.250
Normalized Yield Stress ($MPa/mm^3/mm^3$)	*d0*	1.585±0.938	-	-	-
	d28	4.354±3.861	-	5.545±6.010	11.11±6.625
	d56	5.418±3.551	3.241±2.336	5.736±3.348	9.838±7.229
	d112	4.521±2.929	5.226±4.457	4.266±1.726	9.893±3.052
Normalized Modulus ($MPa/mm^3/mm^3$)	*d0*	81.43±54.88	-	-	-
	d28	160.6±125.4	-	167.5±112.3	293.0±105.0
	d56	159.7±93.99	96.20±63.16	220.4±105.1	254.6±110.2
	d112	132.7±107.3	175.4±178.9	189.8±77.51	331.1±100.5
Normalized Ultimate Stress ($MPa/mm^3/mm^3$)	*d0*	3.429±1.960	-	-	-
	d28	6.140±4.907	-	6.716±6.070	14.44±8.567
	d56	7.546±4.808	4.155±2.602	8.204±3.790	13.17±8.287
	d112	6.635±5.109	7.582±7.779	7.644±3.576	14.07±5.346

Table A. 8. Finite Element Method Simulation Results

	RPC FEM		Trab FEM	
	SCL	**VJE**	**SCL**	**VJE**
Yield Stress (MPa)	7.615±2.002	8.890±3.265	3.587±0.842	4.035±1.673
Yield Strain (mm/mm)	0.031±0.012	0.029±0.014	0.009±0.001	0.009±0.003
Elastic Modulus (MPa)	526.7±354.2	367.6±195.9	404.4±135.1	498.7±257.9
Reaction Force (N)	80.03±54.73	60.01±31.75	259.5±87.23	343.0±203.9
Scaled Tissue Modulus (MPa)	18.44±0.454	17.54±0.920	18.49±0.606	17.53±0.721
Scaled Elastic Modulus (MPa)	973.1±660.9	637.7±337.5	744.7±237.5	869.2±431.7
Scaled Yield Stress (MPa)	13.97±3.535	15.49±5.592	6.614±1.462	7.042±2.803
FEM Platen Diameter (mm)	1.946±0.087	2.062±0.128	-	-
Trabecular Load Share (N/N)	1.013±0.056	1.018±0.029	-	-
Cortical Load Share (N/N)	-0.01±0.056	-0.01±0.029	-	-

APPENDIX B. AUXILIARY FEM FIGURES

Auxiliary figures from FEM simulation are included below. For all figures, "scaled" measures were calculated using specimen-specific tissue modulus scaled by µCT TMD. An asterisk indicates a significant correlation, α=0.05.

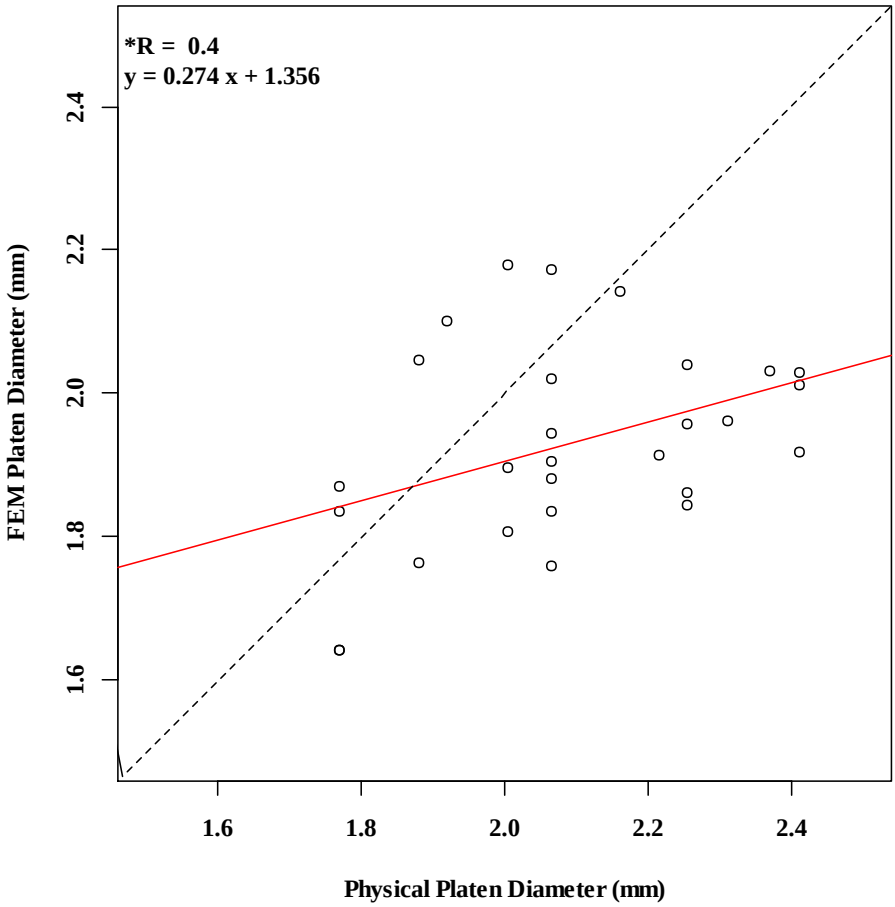

Figure B. 1. FEM RPC virtual platen diameter to physical RPC platen diameter correlation

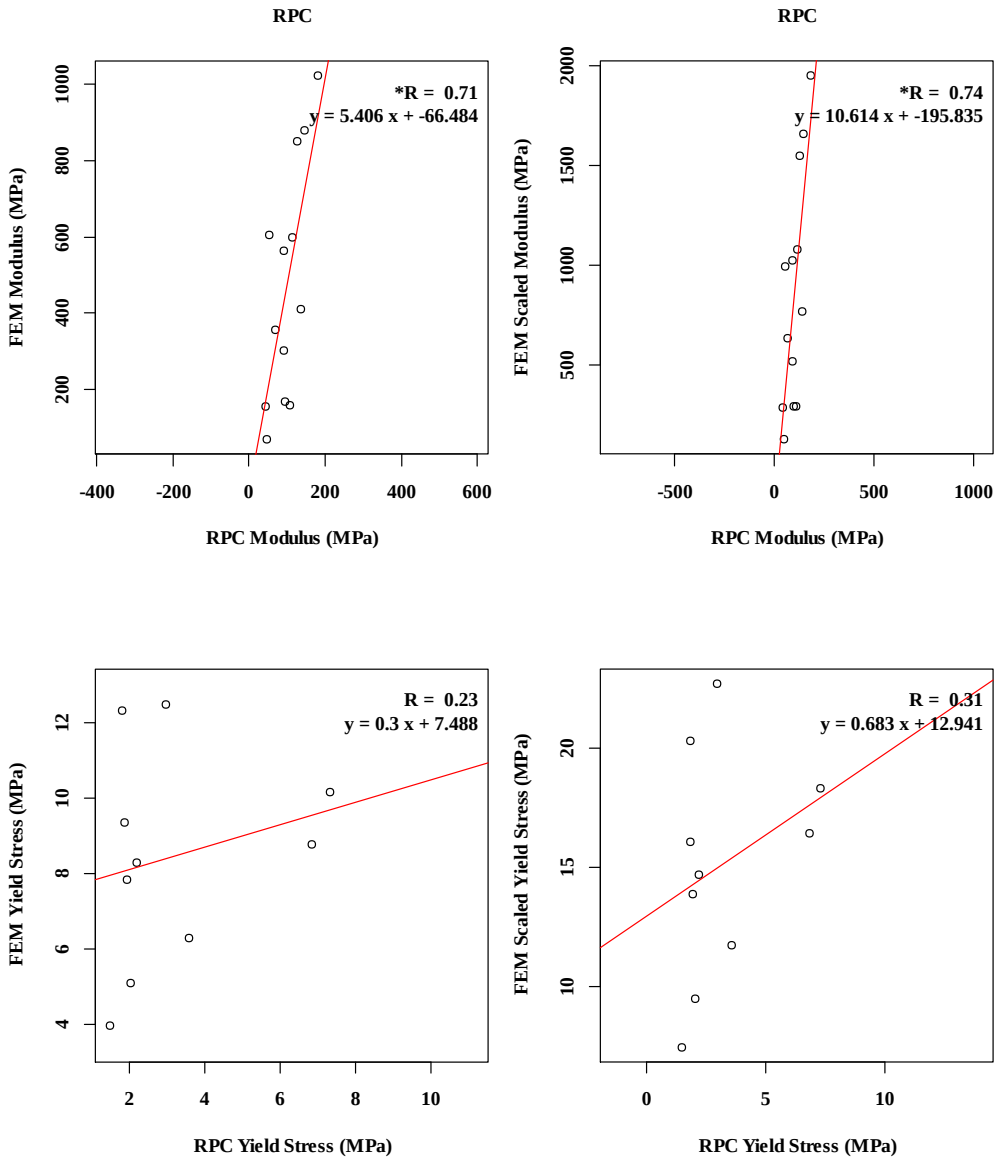

Figure B. 2. FEM RPC to physical RPC correlations

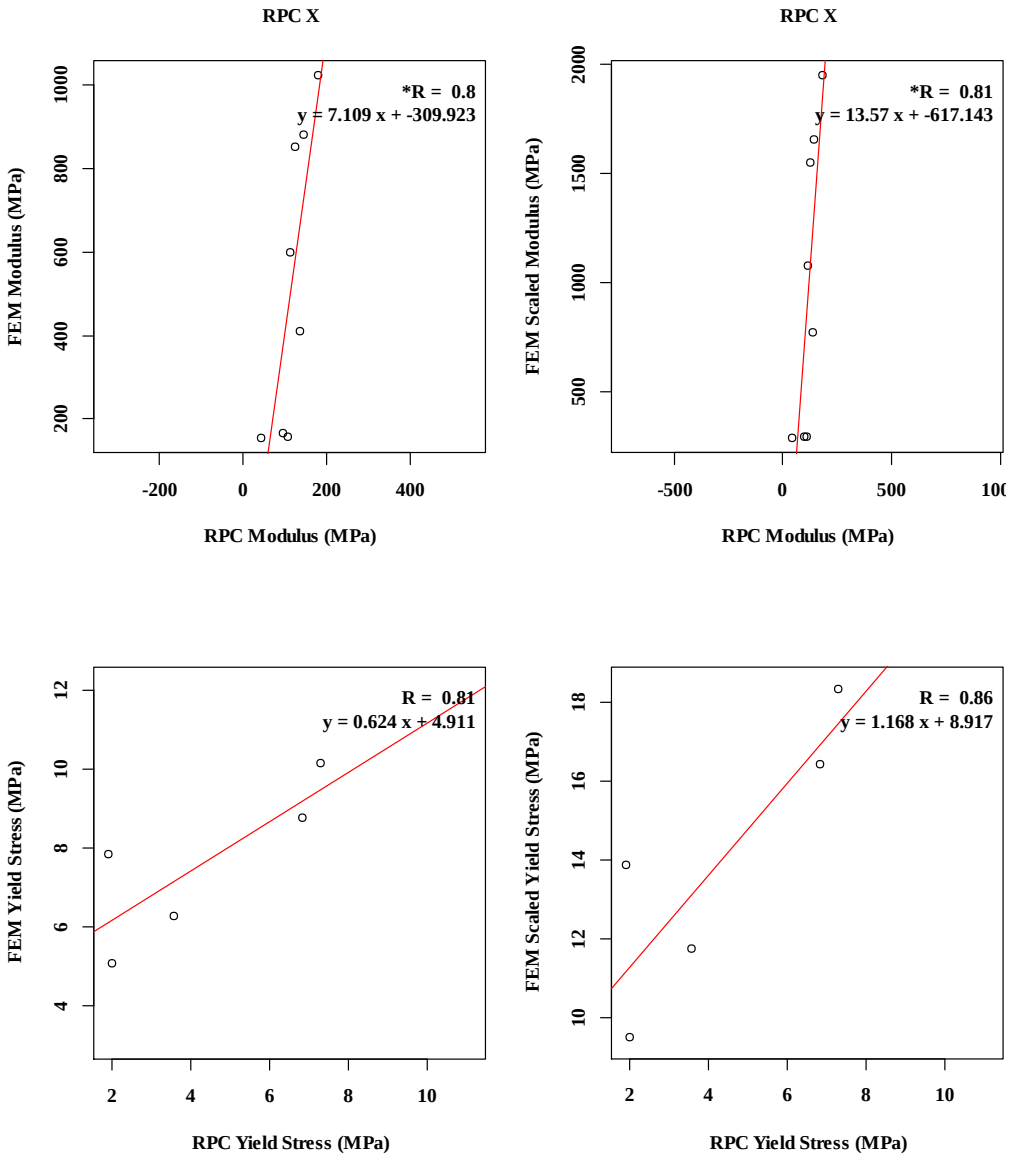

Figure B. 3. FEM RPC to physical RPC correlations, SCL only

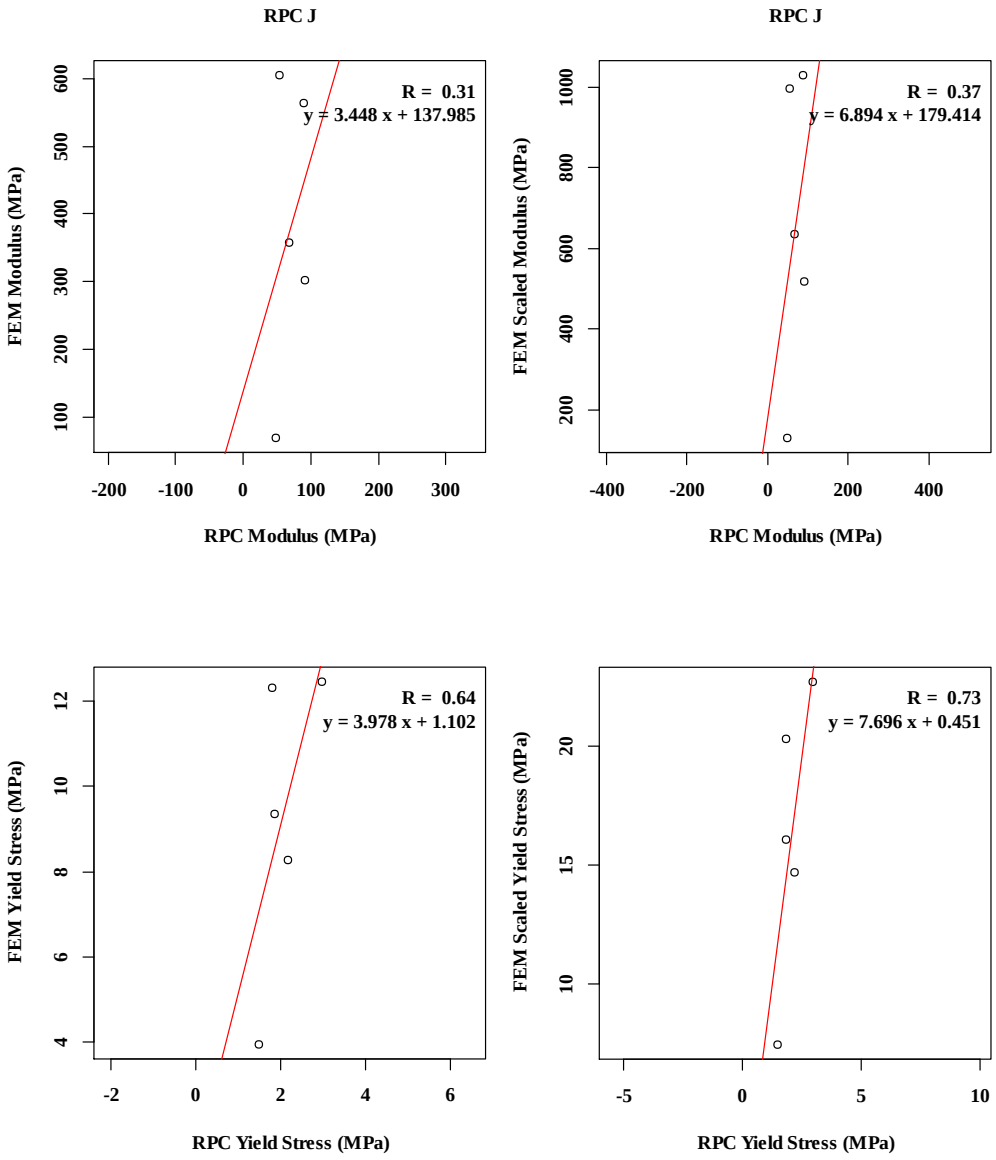

Figure B. 4. FEM RPC to physical RPC correlations, VJE only

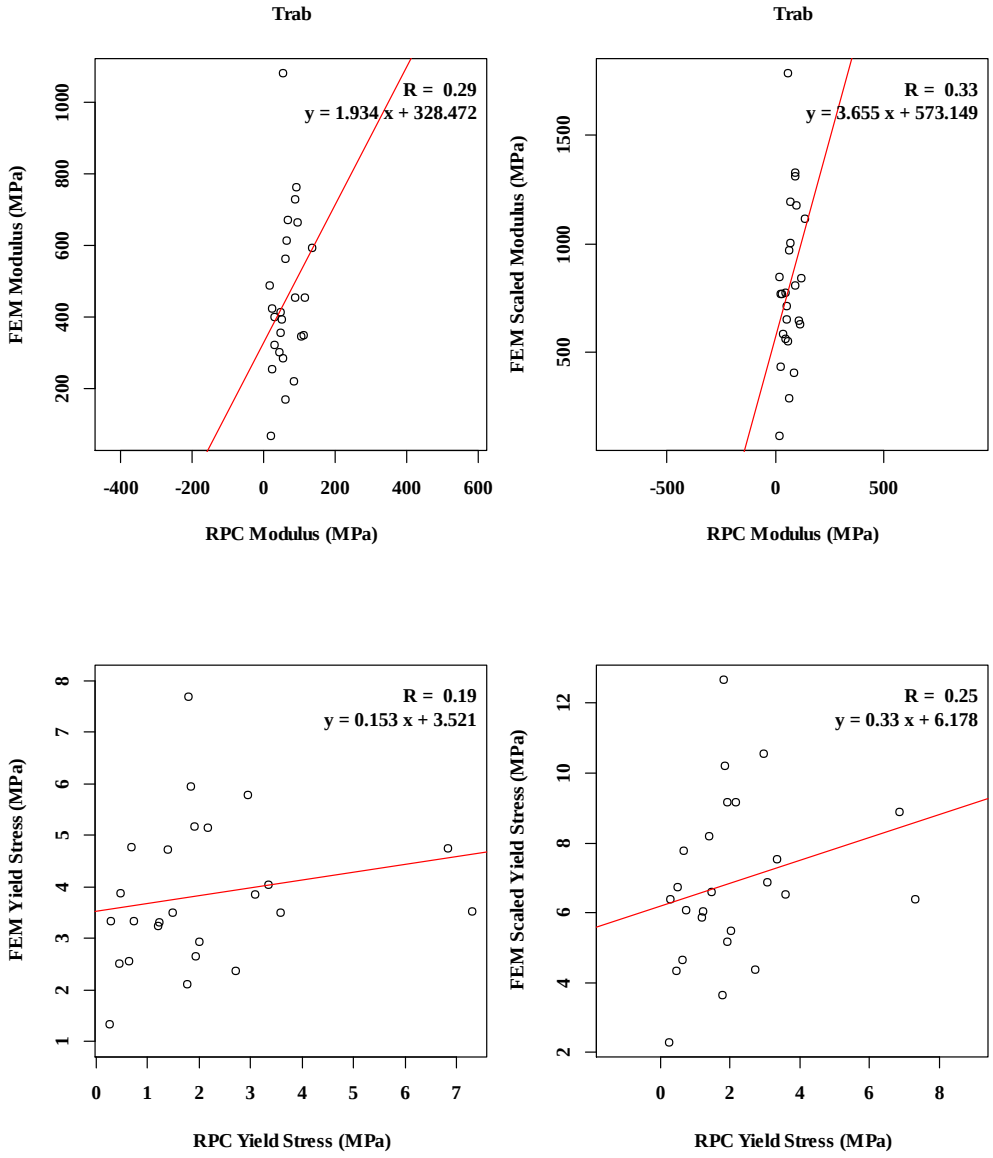

Figure B. 5. FEM Trab to physical RPC correlations

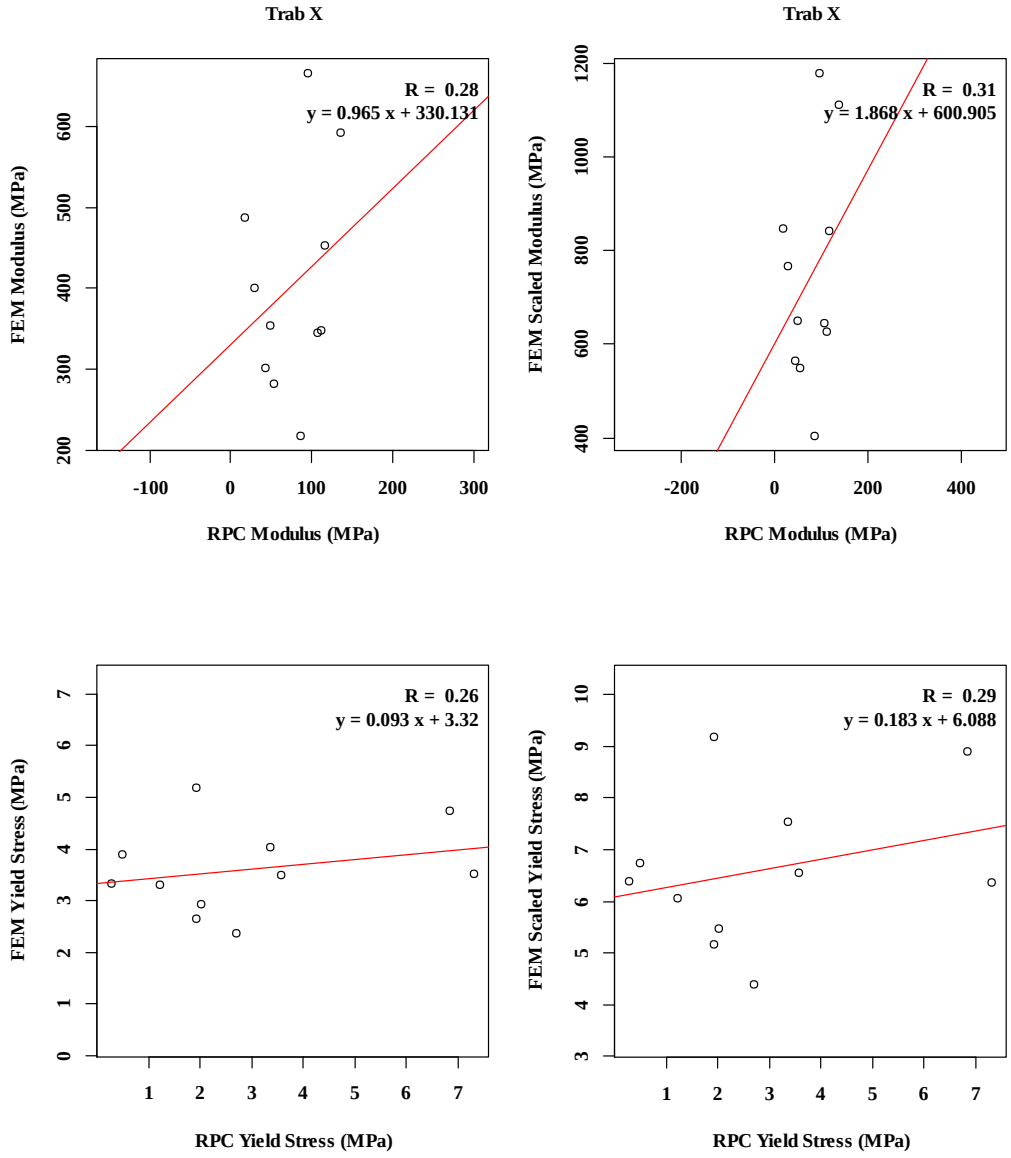

Figure B. 6. FEM Trab to physical RPC correlations, SCL only

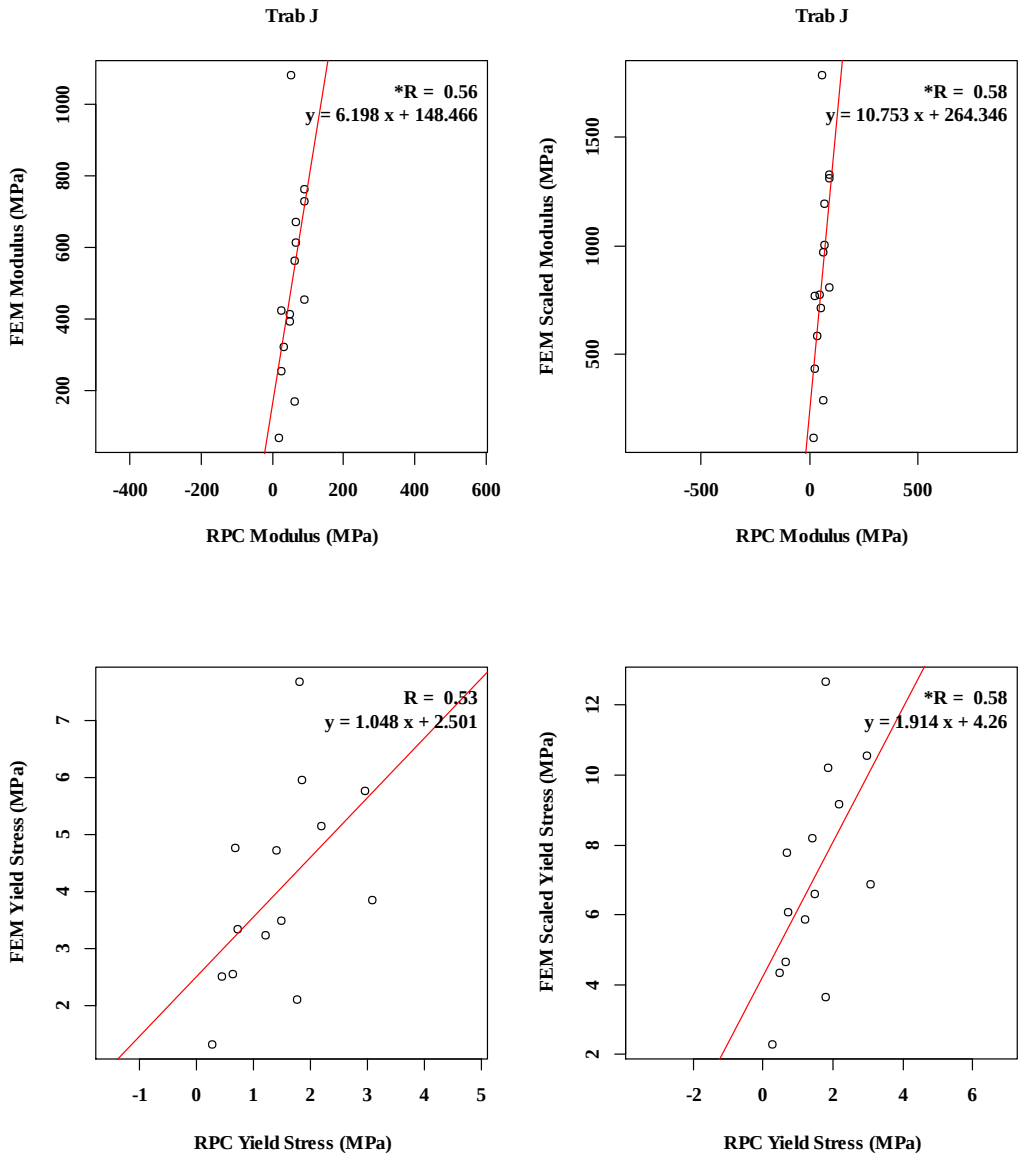

Figure B. 7. FEM Trab to physical RPC correlations, VJE only

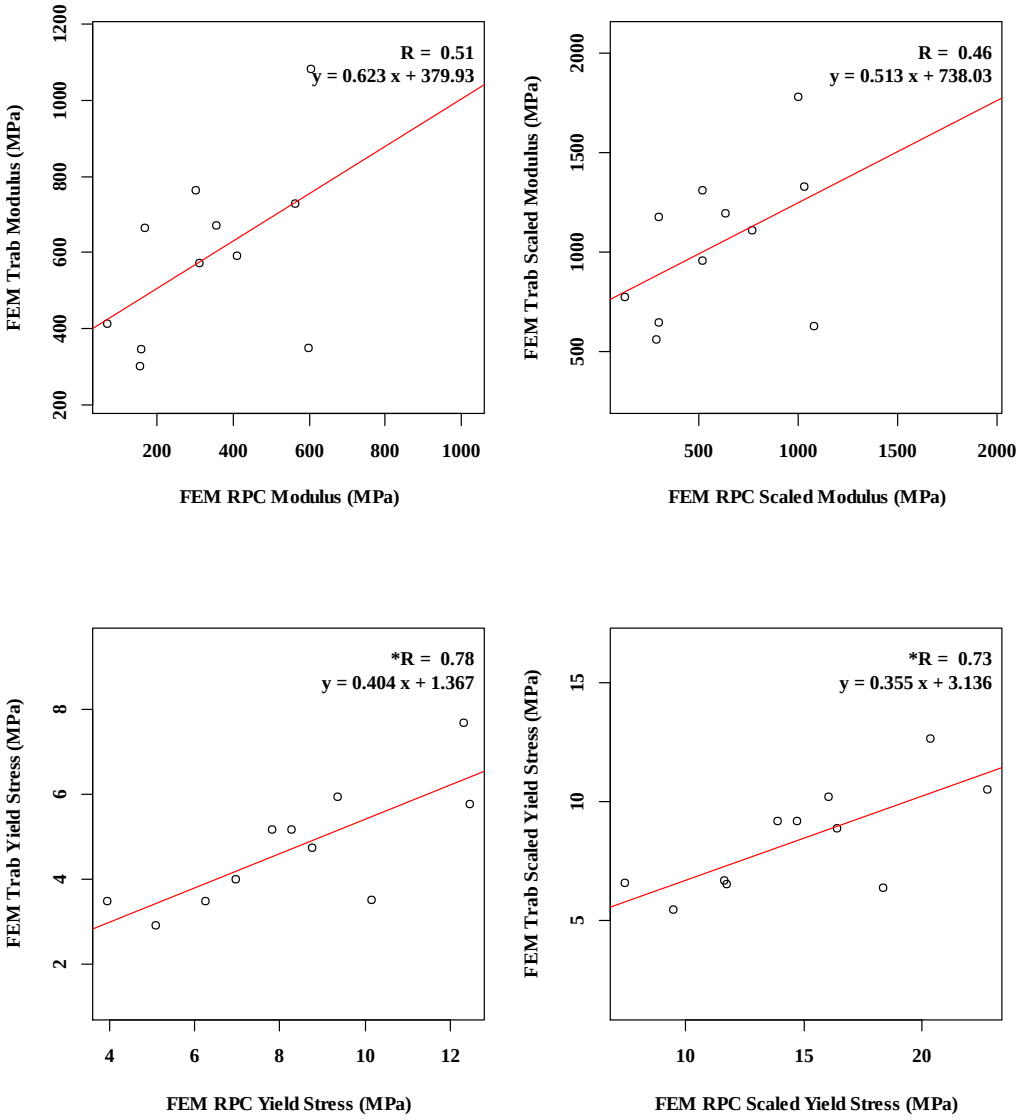

Figure B. 8. FEM Trab to FEM RPC correlations

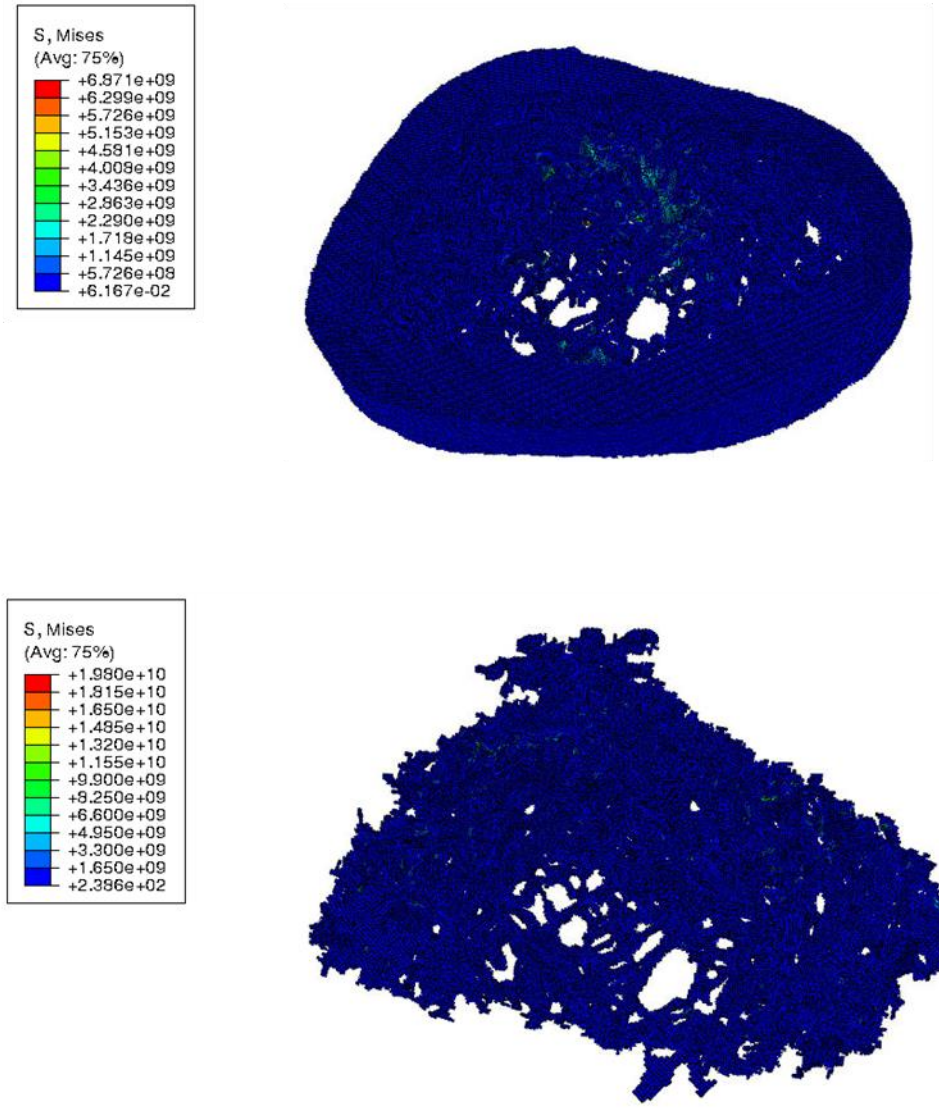

Figure B. 9. Representative Abaqus-generated contour plots
Note the difficulty in discerning any meaningful stress distributions due to the overwhelming number of low-stress elements.